HYDROTHERMAL STUDIES ON MINERAL REPLACEMENT REACTIONS IN THE GOLD-SILVER-TELLURIUM AND COPPER-IRON-SULFUR SYSTEMS

JING ZHAO

B.Eng (2007) & M.Eng (2010), East China University of Science and Technology, Shanghai, China

This thesis is submitted for the degree of Doctor of Philosophy

in

School of Chemical Engineering

at

The University of Adelaide

18 February 2014

Adelaide, Australia

TABLE OF CONTENTS

ABSTRACT

Over the past decades, a number of hydrothermal studies were undertaken on the mineral replacement reactions using hydrothermal method, which mostly proceeded via a coupled dissolution-reprecipitation (CDR) mechanism. However, most of experimental studies have been focused on mineral replacement reactions at relative low pressures and at low to medium temperatures. For hydrothermal mineral deposits set at higher temperature, such as porphyry copper systems or intrusion-related gold deposits, solid-state diffusion may be significant due to the high mobility of the metal ions, and solid-state reactions may compete kinetically with the CDR mechanism. Thus, to investigate the possible interaction between CDR reactions and solid state reactions, we designed a set of hydrothermal studies into the mineral replacement reactions in both Au-Ag-Te and Cu-Fe-S systems.

The mineral replacement of sylvanite was studied under hydrothermal conditions, exploring the effects of temperature (160-220 °C), pH (2-10), and redox conditions on the sample textures and reaction kinetics. Sylvanite transformed to Au-Ag alloy and a range of other gold-(silver)-telluride phases as intermediate products, including petzite (Ag_3AuTe_2), hessite (Ag_2Te), an Ag-rich-Te-depleted calaverite-I ($Au_{0.78}Ag_{0.22}Te_{1.74}$) and a normal calaverite-II $(Au_{0.93}Ag_{0.07})Te_2$. The textures of products are very complex due to the interplay between solution-driven interfaces coupled dissolution-reprecipitation (ICDR) reactions and solid-state diffusion driven processes. The complex interaction among solid-state diffusion and ICDR reactions under hydrothermal conditions is due to the high solid-state mobility of Ag ion in the Au-Ag-Te system.

The hydrothermal synthesis of chalcopyrite was performed via the sulfidation of hematite in solutions containing Cu(I) (as a chloride complex) and hydrosulfide, at pH near the pK_a of H_2S(aq) under hydrothermal conditions. Due to the large positive volume increase, the sulfidation of hematite by chalcopyrite follows a dissolution reprecipitation mechanism progressing via both direct replacement and also overgrowth. Distinct from other solution mediated ICDR reactions (e.g. the transformation from pentlandite to violarite) (Xia et al. 2009), no distinct porosity structures were observed in the quenched product grains. This is probably due, at least in part to the large volume increase during the reactions. This work investigated the nature of CDR reaction with large volume increase at relative high temperatures and high pressures, and improved our understanding of the physical chemistry of chalcopyrite formation in nature.

To explain the transformation mechanism of chalcopyrite and bornite intergrowths, we reported the replacement of chalcopyrite by bornite in solutions containing Cu(I) (as a chloride complex) and hydrosulfide over the temperature range 200-300 °C. Results show that chalcopyrite was replaced by bornite under all studied conditions. The reaction proceeds via a CDR reaction mechanism and with some additional overgrowth of bornite. The bornite product formed at 300 °C for 24 hrs is Cu-rich corresponding to compositions in the bornite-digenite solid solution (*bdss*) $Bn_{90}Dg_{10}$, which can exsolve into digenite lamella in a bornite host during the further annealing in the original solution at 150 ˚C and 200 ˚C for 24 to 120 hrs. The exsolution of *bdss* is another example of solid-state diffusion under hydrothermal conditions.

DECLARATION

I certify that this work contains no material which has been accepted for the award of any other degree or diploma in my name, in any university or other tertiary institution and, to the best of my knowledge and belief, contains no material previously published or written by another person, except where due reference has been made in the text. In addition, I certify that no part of this work will, in the future, be used in a submission in my name, for any other degree or diploma in any university or other tertiary institution without the prior approval of the University of Adelaide and where applicable, any partner institution responsible for the joint-award of this degree.

I give consent to this copy of my thesis when deposited in the University Library, being made available for loan and photocopying, subject to the provisions of the Copyright Act 1968.

The author acknowledges that copyright of published works contained within this thesis resides with the copyright holder(s) of those works.

I also give permission for the digital version of my thesis to be made available on the web, via the University's digital research repository, the Library Search and also through web search engines, unless permission has been granted by the University to restrict access for a period of time.

Signed _____ Date _____

ACKNOWLEDGEMENTS

I am indebted to numerous people who have enlightened and encouraged me through their wisdom and support during these unforgettable years, without their input the completion of this thesis would have been impossible. Firstly I would like to thank my supervisors, Prof. Allan Pring, A/Prof. Joël Brugger, A/Prof. Yung Ngothai, and A/Prof. Brian O'Neill for introducing me into this great project. Without their endless support, patience, encouragement, enthusiasm, invaluable advices and unreserved help throughout my PhD candidature, I would never have obtained the success of this project.

My sincere thanks also go to Dr. Fang Xia, Dr. Barbara Etschmann and Dr. Gujie Qian for their assistance in conducting experiments and many insightful suggestions, to Mr. Ben McHenry of South Australian Museum for prompt responses to requests for chemicals and lab equipments, and to Mr. Len Green, Miss Aoife McFadden, Mr. Angus Netting and Dr. Benjamin Wade from Adelaide Microscopy for their technical assistance in using FESEM, EBSD, ICP-MS and EPMA instruments. I offer my special thanks to Prof. Guorong Chen from East China University of Science and Technology for encouraging me to pursue my career in research. I am particularly grateful to Dr. Haipeng Wang for his suggestions of doing a PhD in the University of Adelaide, and all the assistance in admission and scholarship applications. For those who have helped me but are not specially mentioned, thank you!

I wish to acknowledge Australian Department of Education, Science and Training, for the International Postgraduate Research Scholarship, and University of Adelaide for the

postgraduate scholarship. This work has been made possible by the financial support of the Australian Research Council (Grants DP0880884 and DP1095069).

Last but not least, I would like to thank my dear husband, Pengfei Dong, for his love, kindness and support he has shown during the past three and half years. Furthermore I would also like to thank my parents and parents-in-law for their endless love and support. I love you all and I am going to make you proud.

CHAPTER 1

CHAPTER 1 INTRODUCTION

A mineral replacement reaction is a very common outcome of an interaction between a mineral and aqueous hydrothermal fluid. Whenever a mineral or mineral assemblage is not in equilibrium with the fluid a reaction will occur. This can take the form of mineral dissolution or mineral precipitation and in some cases these reactions can occur together and be spatially coupled. Such coupled reactions are known as coupled dissolution reprecipitation (CDR) reactions. CDR reactions are very important in the formation of hydrothermal ore deposits, such as gold-(silver)-telluride deposits and copper-iron-sulfide deposits. Over the past decade, a number of studies have been undertaken to probe the nature of CDR reactions by investigating transformations between mineral pairs over a range of hydrothermal conditions. However, most of experimental work has been focused on mineral formation reactions at relative low pressures and at low to medium temperatures. In the chalcogenide systems studied to date, the temperatures of the reactions were such that the mobility of the metal ions, due to self-diffusion, was low. So in these reactions the kinetics of any solid-state, diffusion-driven process was likely to be very sluggish when compared to the kinetics of CDR reactions. It is clear, however, that in higher temperature settings such as porphyry copper systems or intrusion-related gold deposits, solid-state diffusion may be significant, and solid-state reactions may compete kinetically with the CDR mechanism. The same consideration applies to more mobile chalcogenide systems such as some Ag and Cu sulfides, selenides, and tellurides. Thus, to investigate the possible interaction between CDR reactions and solid state reactions, we designed a set of laboratory studies into the mineral replacement reactions in both Au-Ag-

Te and Cu-Fe-S systems. This chapter is a brief review of the literature on mineral replacement reactions which proceeded with a coupled dissolution re-precipitation mechanism.

1.1 Mineral replacement reaction and coupled dissolution reprecipitation mechanism

In nature, a mineral or mineral assemblage could be replaced by another whenever it is not in equilibrium with the surrounding environment and the whole process is named as mineral replacement reaction. Some mineral replacements are driven by solid diffusion process, for example, the transformation of graphite to diamond and other high pressure polymorphic transition which occurs in the absences of a fluid. The breakdown of a high temperature solid solution via exsolution is also essentially a process driven by solid state diffusion. For example, the formation of the perthite texture in alkali feldspars. While for mineral replacements in the presence of solvent, the reaction proceeds via the dissolution of less stable phase and the precipitation of a more stable mineral. That is dissolution and precipitation mineral replacement. Processes such as cation exchange, chemical weathering, deuteric alteration, pseudomorphism and leaching can also be considered to proceed via dissolution and precipitation process. Compared with solid state diffusion, hydrothermal mineral replacement reactions are much more heterogeneous and complex processes involving the thermodynamics and kinetics of dissolution, solution transport, precipitation (nucleation for solution) and crystal growth. Putnis (2002) reviewed studies on the mechanism of such fluid-mediated mineral replacement and summarized the characteristic textural and reaction features of CDR reactions as below: (1) the variable length scale of

coupling, *i.e.* the distance between the dissolution front and the site of precipitation; (2) numerous pores and fine cracks in product phases; (3) the sharp reaction front between the parent and product phases; (4) the dependence of solution chemistry and temperature on reaction kinetics and product composition; and (5) the preservation of the external dimension and possibly internal textural details of the parent mineral by product phase.

Table 1.1 Summary of studies on mineral replacement reactions

Mineral replacement reactions	**Reference**
Leucite→analcime	Putnis et al. 1994; Putnis and Putnis 2007
Calcium fluorapatite→calcium hydroxyapatite	Rendón-Angeles et al. 2000
Magnetite→pyrite	Qian et al. 2010
Leucite→analcime	Putnis et al. 2007; Xia et al. 2009b
Pyrrhotite→pyrite	Qian et al. 2011
Calcite→hydroxyapatite	Kasioptas et al. 2008
Pentlandite→violarite	Tenailleau et al. 2006; Xia et al. 2009a
Calcite→fluorite	Putnis 2009
Pyrrhotite→pyrite/marcasite	Qian et al. 2011
Gypsum→calcite	Fernández-Díaz et al. 2009
Quartz→gibbsite	Nahon and Merino 1997
$SrSO_4$→SrF_2	Rendón-Angeles et al. 2006
Bones→calcite	Pewkliang et al. 2008
Calcite→opal	Pewkliang et al. 2008
KBr→KCl	Putnis and Mezge 2004; Putnis et al. 2005
$SrSO_4$ → $Sr(OH)_2$	Rendón-Angeles et al. 2006
Chlorapatite → hydroxyapatite	Yangisawa et al. 1999
Calaverite→gold	Zhao et al. 2009

To illustrate the mechanism of a CDR reaction, let us consider the transformation of calaverite ($AuTe_2$) to gold under hydrothermal conditions (Zhao et al. 2009) as an example. As shown in back-scattered electron images of partially reacted grains (Fig. 1.1), when calaverite is annealed hydrothermally at 220 °C, the dissolution of calaverite results in a

very thin layer of aqueous Au and Te at the reaction front. Once the concentration of gold becomes supersaturated, the nucleation of gold will occur on the surface of calaverite, and followed by the growth of the gold nuclei. As soon as a thin gold rim forms, new Au can easily grow onto this substrate. Gold precipitates near the dissolution site, for kinetic reasons (e.g., favorable heterogeneous nucleation due to calaverite surface). In contrast, Te species are oxidized to Te^{4+}, and transported away from the reaction front into the bulk solution and eventually precipitate as TeO_2(s), probably during quenching. The reaction initiates at the surface and along cracks within the calaverite and then proceeds towards the core until all of the calaverite has dissolved and most of the Au has precipitated. Since calaverite dissolution is rate-limiting step relative to gold precipitation, the interface between gold and calaverite remains sharp with no gap visible at the resolution of the SEM (<20 nm; e.g., Fig. 1.1b). The new-formed gold phase is a mesh of fine gold filaments, a highly porous texture, which plays a critical role in mass transfer between the reaction front and the bulk of the solution (e.g., transport of ions to and from the reaction site), and essential for CDR reactions (Putnis and Putnis 2007). The kinetics of dissolution and precipitation are controlled by the relative solubilities of the parent and product phase, both of which are not only dependent on the reaction pressure and temperature, but also depend on solution compositions (e.g., pH, redox, ligand concentrations). Some other examples on CDR reactions are summarized in Table 1.1. Depending on the relative solubilities of the parent and product phases, the kinetics of dissolution and precipitation might be different, resulting in products with distinct textures (e.g. either be a single crystal or polycrystalline).

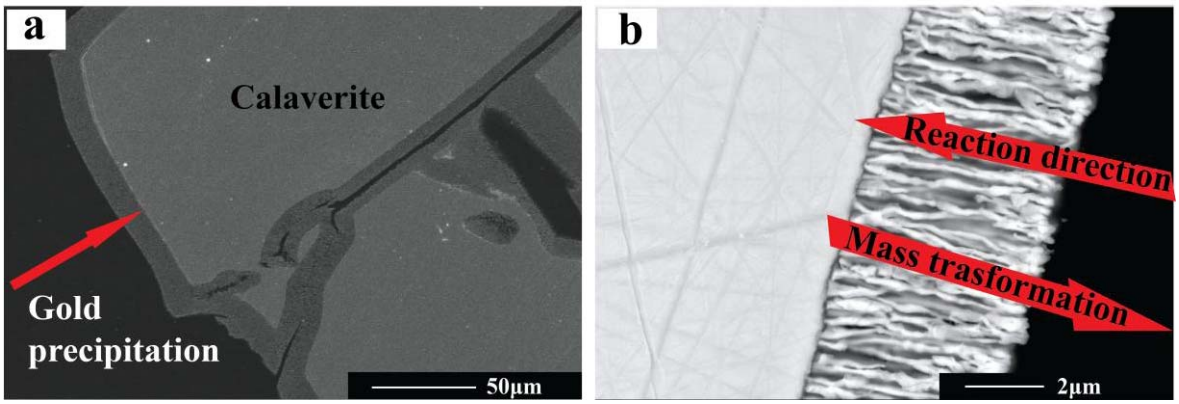

Figure 1.1 (a) Backscattered electron image of cross-sections of a partially reacted calaverite showing that there are sharp boundaries between gold (dark area) and calaverite (light area), and that the reaction preferentially occurs on surface and cracks. (b) An enlargement of the phase boundary, showing the reaction direction, and the porous and filament-shaped gold aggregates growing from the sharp reaction interface.

Since the ubiquitous aqueous fluids in the Earth's crust are important fluid medium for mineral formation in nature, the understanding the dissolution, transport, and precipitation of minerals in hydrothermal fluids are essential to explain the generation of hydrothermal ore deposits. The study of CDR reactions provides information about the physical chemistry of the formation processes of minerals in nature, especially on the dissolution and re-crystallization of hydrothermal minerals and the fluids transport in mineral replacement process. The unique properties of this reaction mechanism can be applied to a wide range of systems and can be used to address a wide range of problems, such as the application in the mining and processing industries. For example, the hydrothermal mineral replacement reactions from calaverite to native gold has been considered as a promising method for ore pre-treatment before cyanide leaching for gold extraction from gold telluride rich-ores (Zhao et al. 2010). The nature of CRD reaction could also be employed in material synthesis, which could not be easily achieved using traditional direct methods. Xia et al. (2008) successfully synthesized two sulfide minerals of low thermal stabilities (<500 °C) using hydrothermal CDR reactions.

1.1.1 Pseudomorphism

Pseudomorphism is one of the most distinctive textural outcomes of CDR reactions. The term is used to denote a replacement reaction in which the external shape and dimensions of primary minerals are preserved by the secondary mineral in the presence of geochemical fluids (Merino and Dewers 1998). Previous studies on pseudomorphic mineral replacement reactions indicate the degree of spatial pseudomorph could vary from nanometer scale to factions of a millimeter depending on cases. For example, under hydrothermal conditions, SrF_2 replaced $SrSO_4$ with the preservation of very fine textural features as small as nanometer scale (Rendón-Angeles et al. 2006), while in the replacement of $SrSO_4$ by $Sr(OH)_2$, the product only preserve large length scale features but loose fine textural details (Rendón-Angeles et al. 2006). To describe the degree of spatial coupling between the dissolution and the precipitation process, Xia et al. (2009) introduced the concept of the scale of pseudomorphism in the replacement of pentlandite by violarite, where the coupling between parent mineral and the product mineral is controlled by the solution chemistry at the reaction front. The dissolution of pentlandite is the rate-controlling step in the reaction solutions pH1-6, and the product could preserve the morphology and internal details of the parent phase in nanometer scale. Under more acidic condition (pH<1), violarite precipitation appears to be rate limiting and a less perfect pseudomorph, really a hollow cast of the parent, was obtained with a length scale of 10's of microns rather than nanometers. To achieve pseudomorphic replacement, the dissolution rate of primary phase must be closely coupled with the precipitation rate of product phase in both space and time during CRD reactions (Putnis 2009). As shown in Figure 1.2a, if the precipitation rate is slower than the dissolution rate, the mineral will dissolve into solution; resulting in a large

fluid gap at the reaction front. Once precipitation of the product mineral commences, the growth rate of the product mineral will remain slower than the dissolution. This results in an ever increasing gap between the dissolution front and precipitation site. If on the other hand the precipitation rate is equal to, or faster than the dissolution rate, the product phase would immediately precipitate at or near the dissolution site resulting in almost no gap at the front and excellent preservation (Fig. 1.2b). Depending on the coupling degree of dissolution between precipitation, the morphological preservation will be very good, loose preservation or no preservation would be observed.

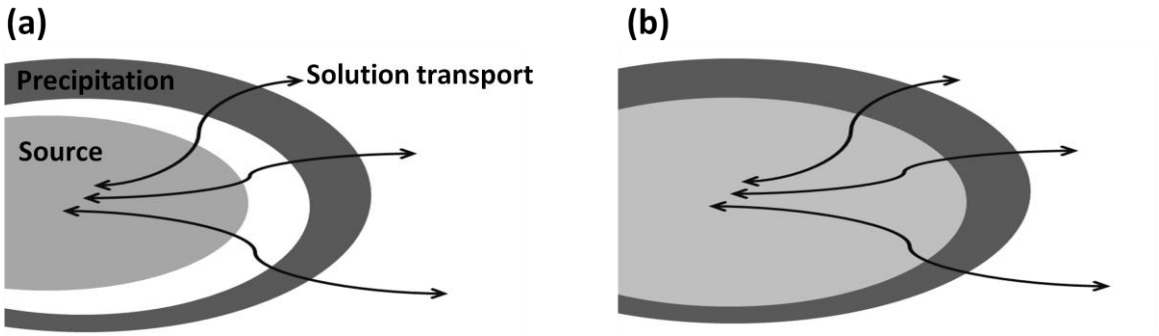

Figure 1.2 Schematic diagram of showing the coupling between dissolution and precipitation with (a) and without gaps at the reaction front between mineral source and production precipitation.

In some CDR reactions, not only the morphology but also the crystallographic orientation of parent phase can also be preserved by the product phase, such as the replacement of chlorapatite by hydroxyapatite (Elliott and Young 1967; Yanagisawa et al. 1999), fluorapatite by hydroxyapatite (Rendón-Angeles et al. 2000), and KBr by KCl (Putnis and Mezger 2004; Putnis et al. 2005). Later work by Xia et al. (2009a) suggested that there must be a close structural relationship between the product and the parent phases, enabling the surface of the parent phase to serve as a patterning agent for the nucleation and growth of the product. Indeed, the CDR reactions have also be used to synthesis materials with

remarkable texture properities. For example, analcime ($NaAlSi_2O_6 \cdot 3H_2O$) has been synthesized from leucite ($KAlSi_2O_6$) via the CDR route (Xia et al. 2009b), and the product presents three-dimensional (3D) ordered arrays of zeolite nanocrystals with uniform size and crystallographic orientation (Fig. 1.3).

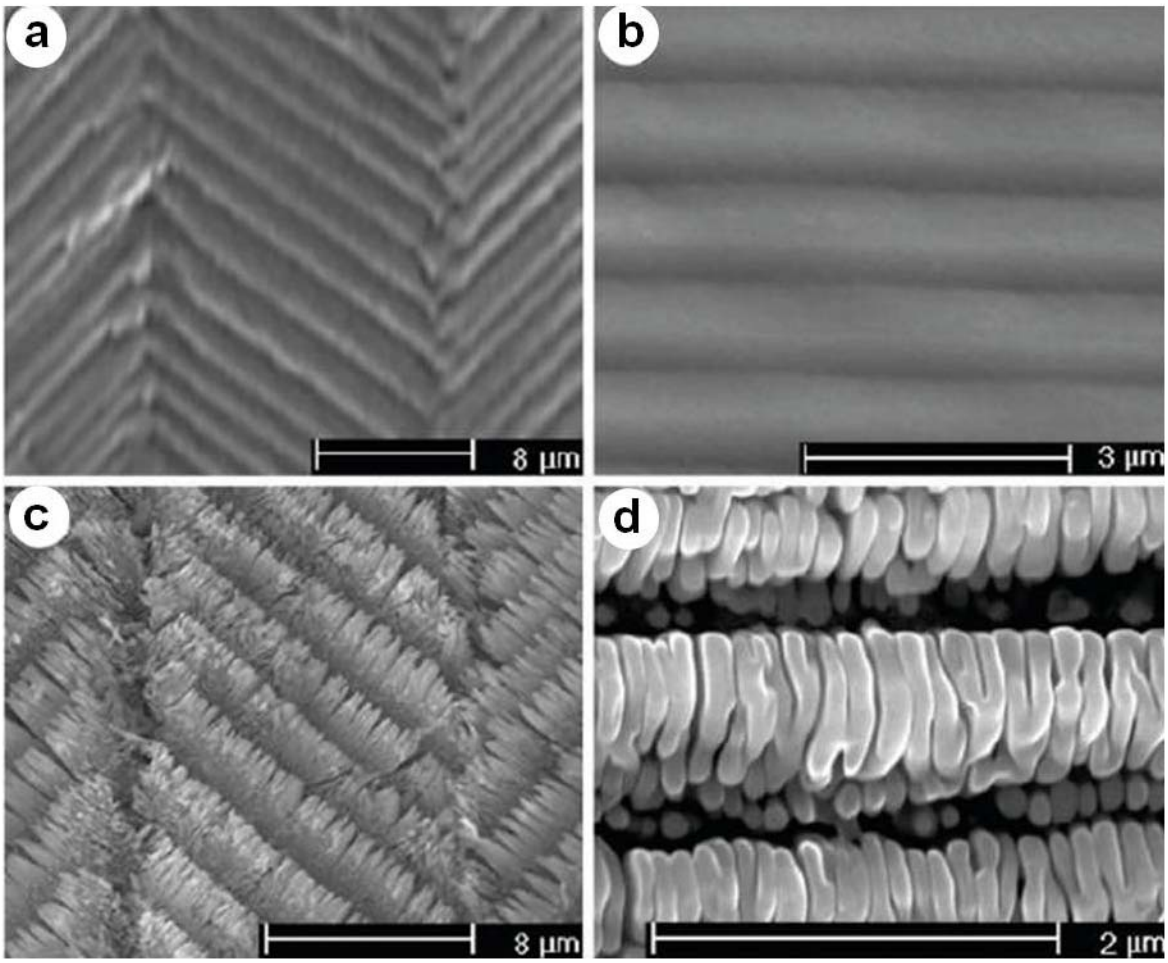

Figure 1.3 SEM images showing (a) the 3D ordered arrays of $KAlSi_2O_6$ lamellae; (b) magnified fine twin lamellae of $KAlSi_2O_6$; (c) product of $NaAlSi_2O_6 \cdot H_2O$ preserved the external morphology of $KAlSi_2O_6$; (d) the 3D ordered arrays of nano $NaAlSi_2O_6 \cdot H_2O$ with uniform size and crystallographic orientation.

1.1.2 Porosity and fine cracks

CDR reactions are fluid-mediated mineral replacement reaction, depending on open pathways for the transport of fluid and solutes between the reaction front and the bulk of

the solution (e.g. ions transportation to and from the reaction site). Networks of fine interconnected pores or fine cracks in product phase provide such pathways in the product minerals, and these are essential to sustain the reactions in enabling mass transfer (Nakamura and Watson 2001; Putnis and Mezger 2004). Figure 1.4 shows the porosity structures of gold product in the replacement of calaverite by gold (Zhao et al. 2009) and fine cracks in violarite replacing pentlandite (Xia et al. 2009a). The generation of porosity or fine cracks is directly related to the molar volume reduction in some studies of mineral replacement reactions. For example, in the replacement of calcite by fluorite (Putnis 2009), the molar volume decreased is 78% based on the Ca conservation. To preserve the external volume of the parent crystal, large amount of pores are generated in the resulted product phase. More examples of mineral replacement reactions with negative molar volume change are listed in Table 1.2. While in some other replacement reactions (e.g. the coarsening of cryptoperthite (Walker et al. 1995)), the loss of parent phase to the fluid is responsible for the generation of porosity. Since the amount of precipitation is less than the amount of dissolution, porosity is generated as the reaction proceeds from the surface of parent grain to the core. Based on the studies of NaCl-KCl-H_2O system, Putins (2002) pointed out that in a mineral replacement reaction, the absolute translated mole quantity should also be taken into account while considering the total volume change. A small quantity of product with a larger molar volume could also lead to porous texture. This point could be further confirmed by recent researches showing that mineral replacement reactions with positive molar volume increase also show porosity structures or fine cracks in the product minerals, such as the replacement of leucite by analcime (Putnis et al. 1994; Xia et al. 2009) and the replacement of magnetite by pyrite (Qian et al. 2010). Thus, the

generation of porosity is a function of both the change in molar volume of the solids and the relative solubilities of the parent and product phases in the aqueous solutions.

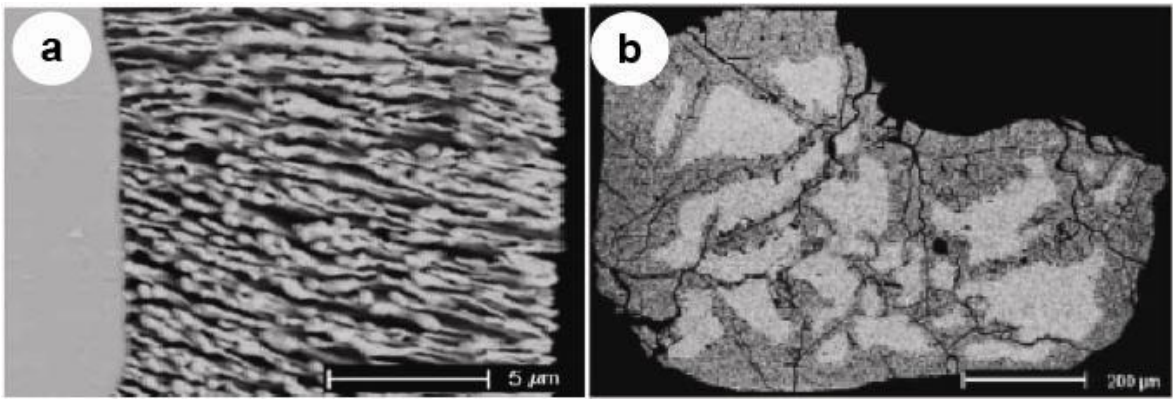

Figure 1.4 (a) An enlargement of the reaction from in the transformation of calaverite by gold, showing the details of the filament-shaped gold crystals (Zhao et al. 2009). (b) Representative backscattered electron micrographs of cross section of pentlandite partially replaced by violarite under conditions of 145°C pH~3.9 in batch Teflon reactor starting with pentlandite (Xia et al. 2009).

Table 1.2 Nominal volume changes and textures during some dissolution-reprecipitation reactions

Reaction	Conservative ion	Volume change (product over parent)	Replacement texture
Calcite→hydroxyapatite	Ca	0.86	Pseudomorphic (Kasioptas et al. 2008)
Pentlandite→violarite	S	0.83	Pseudomorphic (Tenailleau et al. 2006; Xia et al. 2009a)
Calcite→fluorite	Ca	0.78	Pseudomorphic with a porous reaction rim (Putnis 2009)
Pyrrhotite→ pyrite/marcasite	S	0.69/0.71	Pseudomorphic (Qian et al. 2011)
Gypsum→calcite	Ca	0.50	Pseudomorphic (Fernández-Díaz et al. 2009)
Calaverite→gold	Au	0.21	Pseudomorphic (Zhao et al. 2009)
Magnetite→pyrite	Fe	1.60	replacement and overgrowth (Qian et al. 2010)
Leucite→analcime	Al-Si	1.29	Pseudomorphic; large porosity of the product despite volume increase (Putnis et al. 2007; Xia et al. 2009b)
Pyrrhotite→pyrite	Fe	1.16	Pseudomorphic with minor overgrowth (Qian et al. 2011)

A key observation is that if the porous product phase remains in contact with the fluid, it would be expected that the microstructure will continue to evolve with time. In the

replacement of KBr by KCl, the porous KCl product crystal is milky at first due to the porosity but begins to disappear within two days at the room temperature (Putnis 2005). However, the processes by which porosity heals (or anneals out) in the product mineral is still poorly understood. In nature, many minerals formed under hydrothermal conditions do not show obvious porosity in the ground, including ores such as chalcopyrite ($CuFeS_2$) and bornite (Cu_5FeS_4). In this work, chalcopyrite and bornite would be synthesized under hydrothermal conditions, aiming to explore the reason why these minerals are not porous in nature. Is that because of the porous annealing or is it because of large volume change?

1.2 Mineral replacement reactions among gold-(silver)-tellurides

Gold-(silver)-tellurides are very common accessory minerals and found principally in low to medium temperature (≤200 °C) hydrothermal vein deposits, orogenic and intrusion-related gold deposits. The economically important gold-(silver)-tellurides deposits include Golden Mile, Kalgoorlie, Australia (Shackleton and Spry 2003), Cripple Creek, Colorado (Thompson et al. 1985), Emperor, Fiji (Ahmad et al. 1987; Pals and Spry 2003), and Sâcârîmb, Romania (Alderton and Fallick 2000). Gold-(silver)-tellurides carry a significant proportion of the Au in most epithermal gold deposits, such as at the Golden Mile, Kalgoorlie, Australia, where 20% of the recovered gold occurs as tellurides (Shackleton and Spry 2003). However, gold-(silver)-tellurides normally behave in a refractory manner in conventional Au processing circuits, it is essential to develop an efficient and more environmentally friendly alternative for Au recovery from tellurides.

Table 1.3 General information and physical properties of main gold-silver tellurides

Mineral	Chemical Formula	Color	Density (g/cm^3)	Hardness
Calaverite	$AuTe_2$	Silver white to brassy yellow	9.04	2.5-3
Sylvanite	$AgAuTe_4$	Steely gray to silver gray	7.9 - 8.3	1.5-2
Krennerite	$(Au_{1-x},Ag_x)Te_2$	Silver white to blackish yellow	8.53	2.5
Petzite	Ag_3AuTe_2	Bright steel gray to iron black	8.7 - 9.14	2.5
Hessite	Ag_2Te	Lead gray, Steel gray	7.2 - 7.9	1.5-2
Empressite	AgTe	Bronze, Light bronze	7.5 - 7.6	3.5
Stutzite	$Ag_{5-x}Te_3$,(x=0.24-0.36)	Gray, Dark bronze	8	3.5
Muthmannite	$(Ag,Au)Te_2$	Blackish yellow, Bronzy yellow, Grayish white	--	2.5

Note: Data is from http://webmineral.com/data/

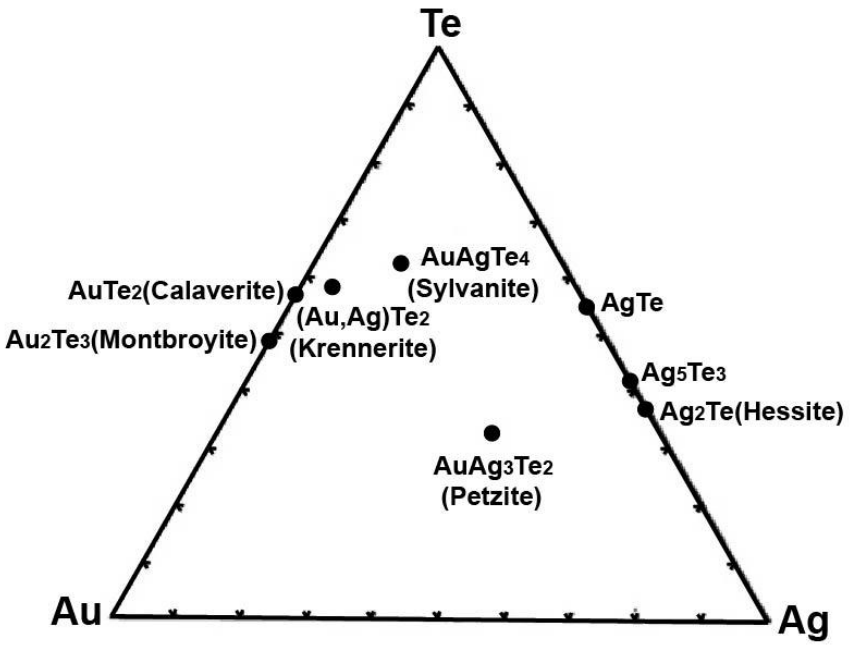

Figure 1.5 Compositions and reactivity of Au-Ag-tellurides Cabri (1965).

Based on previous studies of tellurides-bearing minerals, in total 10 natural occurring phases have been identified as gold-(silver)-tellurides, such as calaverite ($AuTe_2$), krennerite($AuTe_2$), sylvanite ($(Au,Ag)_2Te_4$), petzite (Ag_3AuTe_2), muthmannite ($AgAuTe_2$), empressite(AgTe), hessite (Ag_2Te) and stutzite(Ag_7Te_4). Gold-(silver)-tellurides deposits are also associated with other rare telluride minerals (e.g. tellurobosmuthie (Bi_2Te_3),

volynskite ($AgBiTe_2$), tetradymite(Bi_2TeS_2), coloradpite (HgTe) and altaite(PbTe). Based on the contents of gold and silver, Au-Ag-tellurides minerals are classified into four groups: native elements (native gold, gold-silver alloy and silver), gold-silver tellurides, silver-gold tellurides, and silver tellurides. Calaverite, krennerite, and sylvanite belong to the group of gold-silver tellurides with the chemical formula $Au_{1-x}Ag_xTe_2$. Cabri (1965) gave the following compositional fields: calaverite contains 0 to 2.8 wt% Ag, krennerite contains 3.4 to 6.2 wt% Ag, and sylvanite contains 6.7 to 13.2 wt% Ag. However, more recent work by Bindi et al. (2009) showed that calaverite and sylvanite can have overlapping compositions, and share a similar layer structure topology. The group of silver-gold tellurides contains petzite (Ag_3AuTe_2) and muthmannite ($AgAuTe_2$), and silver tellurides include empressite (AgTe), hessite (Ag_2Te) and stutzite (Ag_7Te_4). A summary of the general information and physical properties of the main gold (and/or silver) tellurides minerals is shown in Table 1.3 and the composition of gold silver tellurium were shown in Figure 1.5 (Cabri 1965).

Over the past decades, several experimental (e.g., Markham 1960; Cabri 1965; Legendre et al. 1980) and theoretical studies (e.g., Afifi et al. 1988) have been conducted on the system Au-Ag-Te. Cabri (1965) conducted a systematic investigation in the ternary system of Au-Ag-Te ternary system, to determine the equilibrium phase relations in the mineralogically important area of the ternary system and phase changes in the assemblages over a range of temperatures. To gain more fundamental knowledge of the thermodynamic data of gold-(silver)-tellurides, Zhang et al. (1994) evaluated the stability of calaverite and hessite and discussed it in context with the stability of other minerals in the system Au-Ag-Te. The calculated stability of hessite and calaverite were applied to explain the physicochemical

conditions of formation of the Gies and Golden Sunlight gold-silver telluride deposits in Montana, USA. Zhao et al. (2009) investigated the replacement of calaverite by gold over a wide range of hydrothermal conditions. At temperatures above 200 °C the transformation takes place in the laboratory on <1 mm size grains in 24 to 48 hrs but is limited by the solubility of Te^{4+} in the solution. The reaction mechanism of this ICDR reaction (interfaced coupled dissolution reprecipitation reaction) is consistent with the breakdown of the Au-bearing telluride nagyágite into an assemblage of gold, altaite, and native tellurium through the action of hydrothermal fluids at Sâcârîmb, Romania (Ciobanu et al. 2008). The porous gold grains from this breakdown share the same structures with mustard gold, which was resulted by the selective leaching of Te from gold tellurides in the weathering zone (e.g., Petersen et al. 1999; Li and Makovicky et al. 2001; Makovicky et al. 2007). The ICDR reaction of calaverite by gold provides an efficient and less toxic alternative pretreatment for the industrial treatment of gold-bearing telluride minerals (Zhao et al. 2010).

Though Au-Ag-Te ternary system is mineralogically and economically important, studies in this system were only focusing on the binary systems of Au-Te and Ag-Te due to the lack of fundamental thermodynamic data of other gold-silver-tellurides. However, the assemblages of gold-silver-tellurides are reported in most deposits and the textures of these minerals are very complex. For example, the mixtures of seven gold-(silver)-telluride minerals were reported in both vein ores and disseminated ores in Sandaowanzi deposit, China (Liu et al. 2011). Since the CDR reactions normally start from the surface of starting grains or along the grain boundaries, the lamella of petzite and hessite is more like to form via a solid state diffusion (Fig 1.6). Carbi (1965) observed the breakdown of phase X

(containing 2.5 to 14.5 wt% gold) to low petzite and low hessite at temperature as low as 50 °C under dry conditions. Thus, it is essential to find out the process of the breakdown of phase X under hydrothermal conditions. It would be particularly interesting to find out if the reaction mechanism occurs via a solid-state diffusion, a CDR processes or the interaction between solid-state diffusions processes and CDR processes.

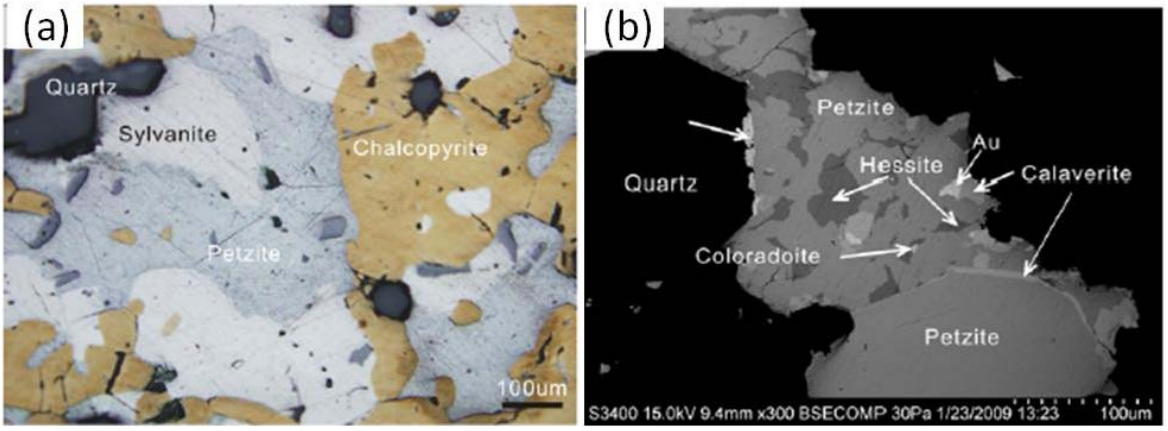

Figure 1.6 Optical microscope image and BSE image of gold-silver-telluride assemblages from Sandaowanzi deposit, China (Liu et al. 2011)

1.3 Mineral replacement reactions among copper iron sulfides

The Cu-Fe-S system is a geologically and economically important ternary system, which has relationship with a wide range of ore deposits, such as moderate temperature sedimentary exhalative (SEDEX) deposits, iron oxide copper gold (IOCG) deposits, and high temperature porphyry copper deposits (Robb 2005). So far, in total 31 minerals were known occurring in the system of Cu-Fe-S, and the composition of Cu-Fe-S minerals reported within Cu-Fe-S system are summarized in Figure 1.7. In some copper iron sulfide deposits, iron sulfide and copper iron sulfide minerals are also often associated with native

gold (Williams et al. 2005). A summary of the general information and physical properties of the main mineral associated with iron oxide-copper-gold deposits mineralization is shown in Table 1.4.

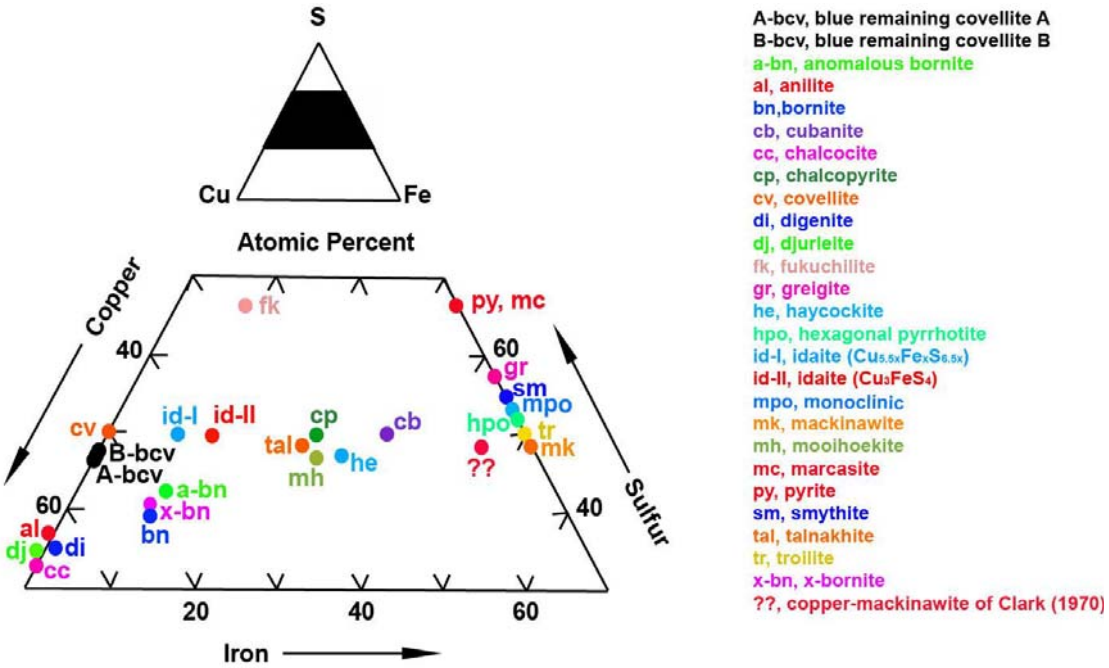

Figure 1.7 Minerals reported within Cu-Fe-S system (after Vaughan and Criag 1978).

Table 1.4 General information and physical properties of IOCG deposits minerals

Mineral	Chemical Formula	Color	Density (g/cm^3)	Hardness
Chalcopyrite	$CuFeS_2$	Brass yellow, Honey yellow	4.19	3.5
Bornite	Cu_5FeS_4	Copper red, Bronze brown, Purple	4.9-5.3	3
Covellite	CuS	Indigo blue, Light blue, Dark blue, Black	4.68	1.5-2
Chalcocite	Cu_2S	Blue black, Gray, Black, Black gray, Steel gray	5.5-5.8	2.5-3
Digenite	Cu_9S_5	Blue, Dark blue, Black	5.6	2.5-3
Pyrite	FeS_2	Pale brass yellow	5-5.02	6.5
Hematite	Fe_2O_3	Reddish gray, Black, Blackish red	5.3	6.5
Magnetite	Fe_3O_4	Grayish black, Iron black	5.1-5.2	5.5-6

Note: Data is from http://webmineral.com/data/

Over the last few decades, a large number of studies on the Cu-Fe-S system have been undertaken in terms of phase relations, transformations within individual compositions, thermodynamic properties and their common occurrence in ore deposits of many types. Most of our knowledge of subsolidus processes in the Cu-Fe-S system is based on experimental studies undertaken using classic dry sealed tube (Tsujimura and Kitakaze 2004; Yund and Kullerud 1960). The high temperature phase relations in the Cu-Fe-S system are relatively simple and are thus well estabilished. At 400°C and above, the phase equilibriums of Cu-Fe-S system mainly contains three extensive solid solutions: intermediate solid solution (or chalcopyrite solid solution, *iss*), chalcocite-digenite-bornite (cc-dg-bn) solid solution and the pyrrhotite (po) solid solution (Figs. 1.8a and 1.8b). As the temperature decreasing, the extent of the solid solution fields decreased and more mineral phases stable phase at 25°C and thought to occur (Fig. 1.8c). Yund and Kullerud (1966) studied the stable phases in the Cu-Fe-S system over a wide range of temperatures and found that the change of the tie-line from bornite + pyrite to digenite + chalcopyrite occured at temperatures below 228 °C. Based on the studies on the phase relations in the Cu-Fe-S system, Cabri (1973) demonstrated that chalcopyrite could break down into an intermediate solid solution + pyrite + vapor at 600 °C. However, Cu-Fe-S related deposits mostly occur under hydrothermal conditions (See Fleet 2006; Vaughan and Craig 1978), the results of dry runs could serve no accurate view of controls on minerals formation under hydrothermal conditions. To develop the phase relations of Cu-Fe-S system under hydrothermal conditions, Sugaki et al. (1975) presented the phase relations of chalcopyrite, bornite, pyrrhotite and the individual phases in intermediated solid solutions at 300 °C and 350 °C. Kojima and Sugaki (1985) studied the phase relations in the Cu-Fe-Zn-S system

between 300 and 500 °C under hydrothermal conditions by the recrystallization of chalcopyrite, bornite, and other sulfides in a 5 m NH_4Cl solution.

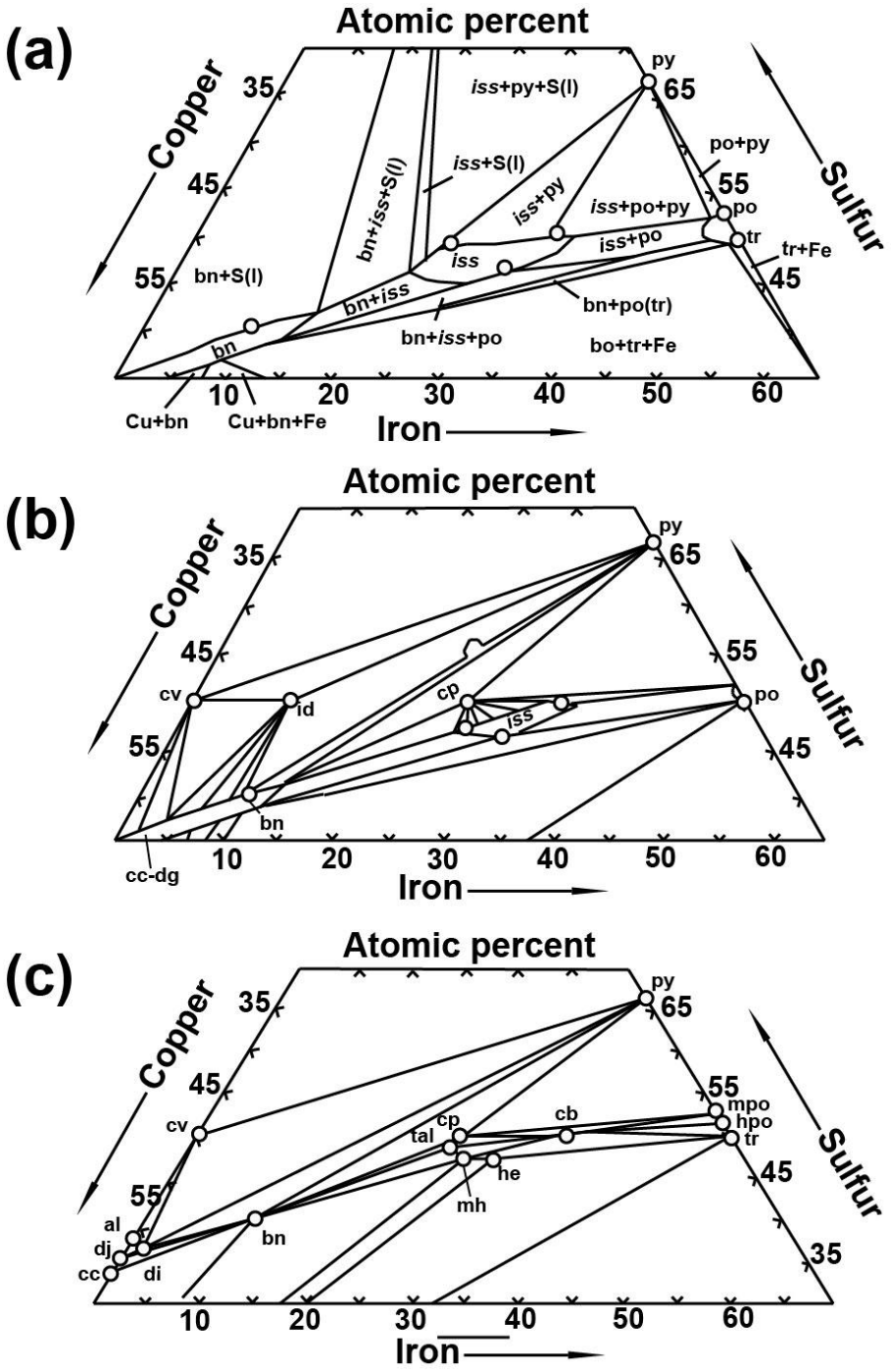

Figure 1.8 Phase relations in the central portion of the Cu-Fe-S system (a) at 600°C (After Cabri 1973); (b) at 400°C (After Craig and Scott 1974); (c) at 25°C. (After Vaughan and Criag 1978)

Chalcopyrite and bornite are the most abundant copper-bearing sulfides and are the primary copper minerals in many ore deposits. Whatever the ore deposit type, chalcopyrite and bornite are essentially hydrothermal minerals, formed from copper-rich saline hydrothermal fluids. The best way to start to explain the physical and chemical processes of copper iron sulfide mineral generation under hydrothermal conditions is to investigate the direct synthesis of chalcopyrite or bornite hydrothermally. To directly understand the formation of chalcopyrite and bornite under hydrothermal conditions, Roberts (1961, 1963), studied the nucleation of chalcopyrite and bornite directly from mixture of Fe (II) and Cu (II) solutions at low temperatures, and demonstrated that formation of copper iron sulfides proceeded via an ion diffusion process route. However, work by Cowper and Rickard (1989) suggested that chalcopyrite could not nucleate from a mixture of 0.01 M Cu^{2+}, Fe^{2+} with equal quantity of a 0.0205 M Na_2S solutions. The nucleation of chalcopyrite was only observed in the reaction of dissolved Cu (II) salts with natural hexagonal pyrrhotite ($Fe_{0.9}S$). Experiments by Rickard and Cowper (1994), in which pyrite was reacted with Cu (II) solution at temperatures ranging from 25 to 350°C, showed that the rate of reaction between pyrite and Cu solutions is purely surface controlled and is dependent on the Cu (II) concentration. Barnard and Christopher (1966a, b) recrystallized crushed chalcopyrite grains in Cl-rich solutions at temperatures between 400 and 500 °C. Seyfried and Ding (1993) conducted a series of experiments to investigate the effects of redox, temperature and fluid chemistry on the solubility of Cu- and Fe-bearing sulfide minerals in Na-K-Cl aqueous fluids in relation to sub-seafloor hydrothermal systems. Hu et al. (1999) synthesized chalcopyrite nanoparticles by dissolving CuCl(s), $FeCl_3 \cdot 6H_2O$(s) and $(NH_4)_2S$(s) in aqueous solutions in autoclaves at 200-250 °C for 3 hrs; the resulting

chalcopyrite was in the form of nanorods typically 20-40 nm in diameter and up to several μm in length. Wang et al. (2009) used a similar method but let the reaction run for 24 hrs to make chalcopyrite nanowires of slightly wider diameter and greater length. Neither of these direct synthesis methods yielded euhedral chalcopyrite typical of that found in nature.

To provide an insight of the direct synthesis of chalcopyrite or bornite hydrothermally, we will present a laboratory study on the formation of chalcopyrite by the replacement of hematite and magnetite under hydrothermal conditions up to 300 °C at vapor-saturated pressures in Chapter 4; and the hydrothermal synthesis of bornite form hematite/chalcopyrite in Chapter 5. Hematite/magnetite has been chosen as starting mineral for chalcopyrite synthesis is due to the reports of chalcopyrite replacing hematite from numerous different ore-forming environments, such as Kupferschiefer type deposits (Kucha and Pawlikowski 1986) and iron-oxide copper gold deposits (Kiruna type; Edfelt et al. 2005). In nature the textures of some chalcopyrite-bornite assemblages could be interpreted in terms of solid state exsolution or unmixing processes, e.g. bornite intergrown with a maze of minute chalcopyrite needles (Ramhdor 1980). The majority of chalcopyrite and bornite intergrowths, however, show textures consistent with mineral replacement reaction and it is believed to occur either by bornite replacing chalcopyrite or visa versa in many typical primary copper sulfide ores (Ramhdor 1980; Robb 2005). Bornite replacing chalcopyrite was observed from Indian Ocean hydrothermal veins (Halbach et al. 1998). The replacement of chalcopyrite by bornite, and further Cu-S type sulfides such as chalcocite, covellite and digenite was found in the origin of Kupferschiefer ore in Poland (Oszczepalski 1999).

1.4 Research objects

Based on previous works, the principal objective of this thesis is to understand the mechanism and kinetics of mineral replacement reactions in both the Cu-Fe-S and Au-Ag-Te systems. To achieve this aim, three detailed experimental studies on mineral replacement reactions were designed and the results are presented in this thesis. In Chapter 3, we will present the results of a laboratory study into the transformation of sylvanite to Au-Ag alloy over a range of hydrothermal conditions. One aim of this work is to establish the mechanism of mineral replacement of an Au-Ag telluride, to characterize the resulting textures, and to compare these results with our previous studies on the replacement of calaverite (Zhao et al. 2009, 2010). Given that sylvanite melts at 354 °C it is reasonable to expect that cation diffusion in this mineral will be significant at temperatures above 145 °C (two thirds of the melting point in Kelvin) for experiments on a laboratory timescale (days to months). In particular we were interested to track the fate of the Ag during the transformation and to assess whether solid-state diffusions processes interact with dissolution-reprecipitation processes in Au-Ag-Te system. Chapter 4 presents the hydrothermal synthesis of chalcopyrite via the sulfidation of hematite in solutions containing Cu(I) (as a chloride complex) and hydrosulfide, at 200-300 °C and pH near the pK_a of H_2S(aq). This study on the replacement of hematite by chalcopyrite and bornite will reveal details of the mechanisms and kinetics of this mineral replacement reaction at relative high temperatures. Considering a large volume increase between parent and product minerals, we are particularly interested in the controls of reaction pathways onto the final mineral assemblage. Chapter 5 focuses on the synthesis of bornite from both hematite and chalcopyrite under hydrothermal conditions. The aim of this is to explain the

formation of bornite over a wide range of physical and chemical hydrothermal conditions. In Chapter 6, the overall investigations and findings of this thesis will be summarized and some possible suggestions on future work will be listed. Author's other publications related to this research would be attached in the Appendix at the end of this thesis.

1.5 Reference

Afifi, A.M., Kelly, W.C., and Essene, E.J. (1988) Phase relations among tellurides, sulfides, and oxides; I, Thermochemical data and calculated equilibria. Economic Geology, 83(2), 377-394.

Ahmad, M., Solomon, M., and Walshe, J.L. (1987) Mineralogical and geochemical studies of the Emperor gold telluride deposit, Fiji. Economic Geology, 82, 234-270.

Barnard, W.M. and Christopher, P.A. (1966a) Hydrothermal synthesis of chalcopyrite. Economic Geology, 61, 897-902.

Barnard, W.M. and Christopher, P.A. (1966b) Further study on the effectiveness of aqueous solutions in the hydrothermal synthesis of chalcopyrite. Economic Geology, 61, 1287-1290.

Bindi, L., Arakcheeva, A., and Chapuis, G. (2009) The role of silver on the stabilization of the incommensurately modulated structure in calaverite, $AuTe_2$. American Mineralogist, 94, 728-736.

Cabri, L.J. (1965) Phase relations in the Au-Ag-Te system and their mineralogical significance. Economic Geology, 60, 1569-1605.

Cabri, L.J. (1973) New data on Phase Relations in the Cu-Fe-S System. Economic Geology, 68 (4), 443-454.

Ciobanu, C.L., Cook, N.J., Pring, A., Damian, G., and Căpraru, N. (2008) Another look at nagyágite from the type locality, Sâcârîmb, Romania: Replacement, chemical variation and petrogenetic implications. Mineralogy and Petrology, 93(3-4), 273-307.

Cowper, M. and Rickard, D. (1989) Mechanism of chalcopyrite formation from iron monosulphides in aqueous solutions (< 100°C, pH 2-4.5). Chemical Geology, 78(3-4), 325-341.

Craig, J.R. and Scott, S.D. (1974) Sulfide phase equilibria. In Mineral. Soc. Am. Short Course Notes, I, CSI-CSIIO.

Edfelt, Å., Armstrong, R., Smith, M., and Martinsson, O. (2005) Alteration paragenesis and mineral chemistry of the Tjårrojåkka apatite-iron and Cu(-Au) occurrences, Kiruna area, northern Sweden. Mineralium Deposita, 40, 409-434.

Elliott, J.C. and Young, R.A. (1967) Conversion of single crystals of chlorapatite into single crystals of hydroxyapatite. Nature, 214(5091), 904-906.

Fernández-Díaz, L., Pina, C.M., Astilleros, J.M., and Sánchez-Pastor, N. (2009) The carbonatation of gypsum: Pathways and pseudomorph formation. American Mineralogist, 94, 1223-1234.

Fleet, M.E. (2006) Phase Equilibria at High Temperatures. Reviews in Mineralogy and Geochemistry, 61(1), 365-419.

Halbach, P., Blum, N., Münch, U., Plüger, W., Garbe-Schönberg, D., and Zimmer, M. (1998) Formation and decay of a modern massive sulfide deposit in the Indian Ocean. Mineralium Deposita, 33(3), 302-309.

Hu, J., Lu, Q., Deng, B., Tang, K., Qian, Y., Li, Y., Zhou, G., and Liu, X. (1999) A hydrothermal reaction to synthesize $CuFeS_2$ nanorods. Inorganic Chemistry Communications, 2(12), 569-571.

Kasioptas, A., Perdikouri, C., Putnis, C.V., and Putnis, A. (2008) Pseudomorphic replacement of single calcium carbonate crystals by polycrystalline apatite. Mineralogical Magazine, 72(1), 77-80.

Kojima, S. and Sugaki, A. (1985) Phase relations in the Cu-Fe-Zn-S system between 500 °C and 300 °C under hydrothermal conditions. Economic Geology, 80(1), 158-171.

Kucha, H. and Pawlikowski, M. (1986) Two-brine model of the genesis of strata-bound Zechstein deposits (Kupferschiefer type), Poland. Mineralium Deposita, 21(1), 70-80.

Legendre, B., Souleau, C., and Chhay, H. (1980) The ternary system Au-Ag-Te. Bull Soc Chim France, (5-6), 197-204.

Li, J.L. and Makovicky, E. (2001) New studies on mustard gold from the Dongping Mines, Hebei Province, China: The tellurian, plumbian, manganoan and mixed varieties. Neues Jahrbuch Fur Mineralogie-Abhandlungen, 176, 269-297.

Liu, J., Bai, X., Zhao, S., Tran, M., Zhang, Z., Zhao, Z., Zhao, H., and Lu, J. (2011) Geology of the Sandaowanzi telluride gold deposit of the northern Great Xing'an Range, NE China: Geochronology and tectonic controls. Journal of Asian Earth Sciences, 41(2), 107-118.

Markham, N.L. (1960) Synthetic and natural phases in the system Au-Ag-Te. Economic Geology, 55(6), 1148-1178.

Makovicky, E., Chovan, M., and Bakos, F. (2007) The stibian mustard gold from the Krivan Au deposit, Tatry Mts., Slovak Republic. Neues Jahrbuch für Mineralogie-Abhandlungen, 184, 207-215.

Merino, E. and Dewers, T. (1998) Implication of replacement for reaction-transport modelling. Journal of Hydrology, 209, 137-146.

Nahon, D. and Merino, E. (1997) Pseudomorphic replacement in tropical weathering: evidence, geochemical consequences, and kinetic-rheological origin. American Journal of Science, 297, 393-417.

Nakamura, M. and Watson, E.B. (2001) Experimental study of aqueous fluid infiltration into quartzite: implications for the kinetics of fluid redistribution and grain growth driven by interfacial energy reduction. Geofluids, 1, 73-89.

Oszczepalski, S. (1999) Origin of the Kupferschiefer polymetallic mineralization in Poland. Mineralium Deposita, 34, 599-613.

Pals, D.W. and Spry, P.G. (2003) Telluride mineralogy of the low-sulfidation epithermal Emperor gold deposit, Vatukoula, Fiji. Mineralogy and Petrology, 79(3-4), 285-307.

Petersen, S.B., Makovicky, E., Li, J.L., and Rose-Hansen, J. (1999) Mustard gold from the Dongping Au-Te deposit, Hebei Province, People's Republic of China. Neues Jahrbuch Fur Mineralogie-Monatshefte, 337-357.

Pewkliang, B., Pring, A., and Brugger J. (2008) The formation of precious opal: clues from the opalization of bone. Canadian Mineralogist, 46, 139-149.

Putnis, A., Putnis, C.V., and Giampaolo, C. (1994) The microstructure of analcime phenocrysts in igneous rocks. European Journal of Mineralogy, 6, 627-632.

Putnis, A. (2002) Mineral replacement reactions: from macroscopic observations to microscopic mechanisms. Mineralogical Magazine, 66 (5), 689-708.

Putnis, C.V. and Mezger, K. (2004) A mechanism of mineral replacement: isotope tracing in the model system KCl-KBr-H_2O. Geochimica et Cosmochimica Acta, 68 (13), 2839-2848.

Putnis, C.V., Tsukamoto, K., and Nishimura, Y. (2005) Direct observations of pseudomorphism: compositional and textural evolution at a fluid-solid interface. American Mineralogist, 90(11-12), 1909-1912.

Putnis, A. and Putnis, C.V. (2007) The mechanism of reequilibration of solids in the presence of a fluid phase. Journal of Solid State Chemistry, 180, 1783-1786.

Putnis, C.V., Geisler, T., Schmid-Beurmann, P., Stephan, T., and Giampaolo, C. (2007) An experimental study of the replacement of leucite by analcime. American Mineralogist, 92, 19-26.

Putnis, A. (2009) Mineral Replacement Reactions. Reviews in Mineralogy and Geochemistry, 70(1), 87-124.

Qian, G., Brugger, J., Skinner, W.M., Chen, G., and Pring, A. (2010) An experimental study of the mechanism of the replacement of magnetite by pyrite up to 300 °C. Geochimica et Cosmochimica Acta, 74(19), 5610-5630.

Qian, G., Xia, F., Brugger, J., Skinner, W.M., Bei, J., Chen, G., and Pring, A. (2011) Replacement of pyrrhotite by pyrite and marcasite under hydrothermal conditions up to 220 °C: An experimental study of reaction textures and mechanisms. American Mineralogist, 96(11-12), 1878-1893.

Ramdohr, P. (1980) The ore minerals and their intergrowths (2nd edition). Pergamon Press, London.

Rendón-Angeles, J.C., Yanagisawa, K., Ishizawa, N., and Oishi, S. (2000) Conversion of Calcium Fluorapatiteinto Calcium Hydroxyapatite under Alkaline Hydrothermal Conditions. Journal of Solid State Chemistry, 151 (1), 65-72.

Rendón-Angeles, J.C., Pech-Canul, M.I., López-Cuevas, J., Matamoros-Veloza, Z., and Yanagisawa, K. (2006) Differences on the conversion of celestite in solutions bearing monovalent ions under hydrothermal conditions. Journal of Solid State Chemistry, 179(12), 3645-3652.

Robb, L. (2005) Introduction to ore-forming processes. Blackwell Publishing, Oxford.

Roberts, W.M.B. (1961) Formation of chalcopyrite by reaction between chalcocite and pyrrhotite in cold solution. Nature, 191 (5), 560-562.

Roberts, W.M.B. (1963) The low temperature synthesis in aqueous solution of chalcopyrite and bornite. Economic Geology, 58 (1), 52-61.

Seyfried Jr., W.E. and Ding, K. (1993) The effect of redox on the relative solubilities of copper and iron in Cl-bearing aqueous fluids at elevated temperatures and pressures: An experimental study with application to subseafloor hydrothermal systems. Geochimica et Cosmochimica Acta, 57(9), 1905-1917.

Shackleton, J.M. and Spry, P.G. (2003) Telluride mineralogy of the Golden Mile deposit, Kalgoorlie, Western Australia. Canadian Mineralogist, 41, 1503-1524.

Sugaki, A., Shima, H., Kitakaze, A., and Harada, H. (1975) Isothermal phase relations in the system Cu-Fe-S under hydrothermal conditions at 350 °C and 300 °C. Economic Geology, 70 (4), 806-823.

Tenailleau, C., Pring, A., Etschmann, B., Brugger, J., Grguric, B., and Putnis, A. (2006) Transformation of pentlandite to violarite under mild hydrothermal conditions. American Mineralogist, 91, 706-709.

Thompson, T.B., Trippel, A.D., and Dwelley, P.C. (1985) Mineralized veins and breccias of the Cripple Creek District, Colorado. Economic Geology, 80(6), 1669-1688.

Tsujimura, T. and Kitakaze, A. (2004) New phase relations in the Cu-Fe-S system at 800 ^{o}C; constraint of fractional crystallization of a sulfide liquid. Neues Jahrbuch für Mineralogie, 10, 433-444.

Vaughan, D.J. and Craig, J.R. (1978) Mineral chemistry of metal sulphides. Cambridge University Press, Cambridge.

Walker, F.D.L., Lee, M.R., and Parsons, I. (1995) Micropores and micropermeable texture in alkali feldspars: geochemical and geophysical implications. Mineralogical Magazine, 59, 505-534.

Wang, M.X., Wang, L.S., Yue, G.H., Wang, X., Yan, P.X., and Peng, D.L. (2009) Single crystal of $CuFeS_2$ nanowires synthesized through solventothermal process. Materials Chemistry and Physics, 115(1), 147-150.

Williams, P.J., Barton, M.D., Johnson, D.A., Fontboté, L., De Haller, A., Mark, G., Oliver, N.H.S. and Marschik, R. (2005) Iron oxide copper-gold deposits: geology, space-time distribution, and possible modes of origin. Economic Geology, 100th Anniversary Volume, 371-405.

Xia, F., Zhou, J., Brugger, J., Ngothai, Y., O'Neill, B., Chen, G., and Pring, A. (2008). Novel route to synthesize complex metal sulfides: hydrothermal coupled

dissolution-reprecipitation replacement reactions. Chemistry of Materials, 20(8), 2809-2817.

Xia, F., Brugger, J., Chen, G., Ngothai, Y., O'Neill, B., Putnis, A., and Pring, A. (2009a) Mechanism and kinetics of pseudomorphic mineral replacement reactions: A case study of the replacement of pentlandite by violarite. Geochimica et Cosmochimica Acta, 73(7), 1945-1969.

Xia, F., Brugger, J., Ngothai, Y., O'Neill, B., Chen, G., and Pring, A. (2009b). Three-dimensional ordered arrays of zeolite nanocrystals with uniform size and orientation by a pseudomorphic coupled dissolution-reprecipitation replacement route. Crystal Growth and Design, 9(11), 4902-4906.

Yanagisawa, K., Rendón-Angeles, J.C., Ishizawa, N., and Oishi, S. (1999) Topotaxial replacement of chlorapatite by hydroxyapatite during hydrothermal ion exchange. American Mineralogist, 84, 1861-1869.

Yund, R.A. and Kullerud, G. (1960) The Cu-Fe-S system: Phase relations at 700 ^{o}C. Year Book - Carnegie Institution of Washington, 111-114.

Zhang, X.M. and Spry, P.G. (1994) Calculated stability of aqueous tellurium species calaverite, and hessitc at elevated temperatures. Economic Geology and the Bulletin of the Society of Economic Geologists, 89(5), 1152-1166.

Zhao, J., Brugger, J., Grundler, P.V., Xia, F., Chen, G., and Pring, A. (2009) Mechanism and kinetics of a mineral transformation under hydrothermal conditions: Calaverite to metallic gold. American Mineralogist, 94(11-12), 1541-1555.

Zhao, J., Xia, F., Pring, A., Brugger, J., Grundler, P.V., and Chen, G. (2010) A novel pretreatment of calaverite by hydrothermal mineral replacement reactions. Minerals Engineering, 23, 451-453.

Zhao, J., Brugger, J., Xia, F., Ngothai, Y., Chen, G., and Pring, A. (2013) Dissolution-reprecipitation versus solid-state diffusion: mechanism of mineral transformations in sylvanite, $(AuAg)_2Te_4$, under hydrothermal conditions. American Mineralogist, 98, 19-32.

CHAPTER 2

CHAPTER 2 RESEARCH METHODOLOGY

This chapter includes an introduction to the starting natural minerals, buffer solution preparation, hydrothermal reaction and the different analytical methods used in this study. Analytical techniques used in this thesis include X-ray powder diffraction (XRD) analysis, field emission scanning electron microscopy (FESEM) analysis, electron probe micro-analysis, electron backscatter diffraction (EBSD) analysis, and solution inductive coupled plasma mass spectroscopy (ICP-MS).

2.1 Natural mineral samples

In total, five natural minerals were used throughout this thesis, including sylvanite, micaceous hematite, kidney ore hematite, magnetite and chalcopyrite. The identification of natural minerals was established using a powder X-ray diffractometer at the South Australian Museum and the composition of each mineral was determined by a Cameca SX-52 electron probe instrument (20 kV, 20 nA) at Adelaide Microscopy, the University of Adelaide. The compositions of staring minerals are listed in Table 2.1. SEM images revealed that some sylvanite crystals contained a small number of micro-inclusions (1 to 5 μm) of euhedral calaveite crystals, which appear to have a consistent crystallographic relationship to the host sylvanite, but they are too small to be investigated by backscatter electron diffraction. XRD analysis of the natural magnetite indicated 81 ± 5 wt% magnetite and 19 ± 5 wt% hematite. Crystals were crashed into small fragments which were washed in the ultrasonic bath, ground and carefully sieved into a 150-400 μm fraction for sylvanite and into a 125 to 150 μm fraction for the other samples.

Table 2.1 Compositions of staring materials

Sylvanite (Vatukoula, Fiji, SA Museum G6983/VIC Museum E16799) (analysis on 16 points) (wt%)			
	Mean	**Range**	**Standard deviation**
Au	29.83	28.61-30.48	0.25
Ag	9.24	8.98-9.51	0.12
Te	61.45	60.85-61.82	1.87
Sb	0.38	0.31-0.44	0.01
Total	100.90		
Hematite (Cumberland, England, SA Museum G6983) (analysis on 21 points) (wt%)			
	Mean	**Range**	**Standard deviation**
Fe_2O_3	97.33	94.35-100.69	0.36
SiO_2	1.21	<0.06-2.98	0.06
Al_2O_3	0.05	<0.06-0.17	0.06
MgO	0.04	<0.05-0.10	0.05
MnO_2	0.03	<0.06-0.08	0.06
P_2O_5	0.04	<0.05-0.13	0.05
Total	98.53		
Kidney ore hematite (Cumberland, England, SA Museum G1603) (analysis on 18 points) (wt%)			
	Mean	**Range**	**Standard deviation**
Fe_2O_3	96.92	95.06-98.66	0.36
SiO_2	1.21	0.96-1.35	0.06
Al_2O_3	0.04	<0.02-0.11	0.02
MnO_2	0.03	<0.02-0.06	0.02
P_2O_5	0.06	<0.05-0.11	0.05
CaO	≤0.06		0.06
Total	98.32		
Magnetite (Mt. Isa area, Queensland, SA Museum G8146) (analysis on 13 points) (wt%)			
	Mean	**Range**	**Standard deviation**
Fe_3O_4	99.25	99.67-100.52	0.38
VO_2	0.61	0.58-0.65	0.03
SiO_2	0.03	<0.03-0.04	0.03
Al_2O_3	0.03	<0.03-0.07	0.03
MgO	0.02	<0.02-0.03	0.02
MnO	0.05	<0.03-0.09	0.03
Total	99.99		
Chalcopyrite (Moonta Mines, South Australian, SA Museum G22621) (analysis on 24 points) (wt%)			
	Mean	**Range**	**Standard deviation**
Cu	35.46	35.21-35.77	0.29
Fe	31.23	31.02-31.35	0.29
S	33.49	33.23-33.81	0.25
Total	100.19		

2.2 Preparation of buffer solution

Buffer solutions (including acetate, phosphate and borate) ranging from pH 2-12 were used throughout this study. High purity water (conductivity was 18 MΩ cm^{-1}; Direct - Q3system,

Millipore corp.) was used to prepare buffer solutions (Table 2.2) at room temperature (~25 °C). A temperature-corrected pH-meter (EUTECH Scientific, model Cyber-scan 510) with an Ag/AgCl pH electrode was used for the pH measurements. Calibrations were performed with AQUASPEX standard buffer solutions: $pH_{25°C}$ = 4.01 (KH-phthalate buffer), $pH_{25°C}$ = 7.00 (phosphate buffer), and $pH_{25°C}$ = 10.01 (carbonate buffer). The pHs the of buffer solutions at reaction temperature were calculated using the Geochemist's Work Bench (GWB) (Bethke 2008) or the HCh geochemical modeling software (Shvarov and Bastrakov 1999).

Table 2.2 Composition of buffer solutions used in this study

No.	$pH_{25°C}$		Components			
	calc.	meas.	Acid	C/m	Basic	C/m
P2	2.00	2.10	H_3PO_4	0.1044	$NaH_2PO_4·2H_2O$	0.0954
P3	3.10	2.98	H_3PO_4	0.0170	$NaH_2PO_4·2H_2O$	0.1820
A5	5.06	4.88	CH_3COOH	0.0590	CH_3COONa	0.1400
P7	7.03	6.90	$NaH_2PO_4·2H_2O$	0.0680	Na_2HPO_4	0.1310
B10	10.1	9.80	H_3BO_3	0.1064	NaOH	0.0936
P11	10.8	10.8	Na_2HPO_4	0.2000	NaOH	0.0282
CP2	2.10	2.10	H_3PO_4	0.5220	$NaH_2PO_4·2H_2O$	0.4770
CA4	3.99	3.86	CH_3COOH	0.8260	CH_3COONa	0.1740
CA5	5.06	4.88	CH_3COOH	0.2960	CH_3COONa	0.7040
CA6	5.92	5.73	CH_3COOH	0.5490	CH_3COONa	0.9550
CP7	7.03	6.90	$NaH_2PO_4·2H_2O$	0.3400	Na_2HPO_4	0.6550
CP8	8.08	8.02	$NaH_2PO_4·2H_2O$	0.0450	Na_2HPO_4	0.9540
CB9	9.10	8.76	H_3BO_3	0.7040	NaOH	0.2950
CB10	10.1	9.80	H_3BO_3	0.5320	NaOH	0.4800

In the replacement of sylvanite by Au-Ag alloy, 0.1m NaCl was added into P2, P7 and B10 buffer solutions, which was used to more closely mimic natural hydrothermal fluids and provide ligands to increase Ag mobility. For the other two sets of experiments related to Cu-Fe-S minerals, solutions were prepared with the boiled high purity water in an argon-filled anoxic glove box (Fig. 2.1) at room temperature (~ 25 °C). 1 m NaCl was added into

each solution to prevent copper (I) from disproportionating into copper (II) and copper (0) (Brugger et al. 2007).

Figure 2.1 The argon-filled anoxic glove box used in this work.

2.3 Hydrothermal experiments

To study the coupled dissolution and reprecipitation reaction mechanism, three sets of experiments on gold silver tellurides and copper iron sulfide minerals were performed using the *in situ* hydrothermal method. Two types of designed reactors were used throughout this project: 25mL polytetrafluoroethylene (PTFE) cells sealed in stainless steel static batch reactors (Fig. 2.2) and 8 mL titanium autoclaves (Fig. 2.3). As the maximum working temperature for PTFE is approximately 260 ºC, the PTFE lined stain steel static cells were used for experiments carried out at temperatures up to 220 ºC, while titanium

cells were used for experiments run at higher temperatures. For most of the sylvanite runs, 10 mg sylvanite crystal fragments and 15 mL reaction solution were added to a 25 mL PTFE cells, leaving a 10 mL headspace for expansion. For the synthesis of chalcopyrite, 10 mg hematite crystal fragments, 12.5 mg CuCl pure powder, and 189 mg thioacetamide were carefully weight and added into the titanium cell with 5 mL solution in the N_2-filed anoxic glove box (Fig. 2.1).

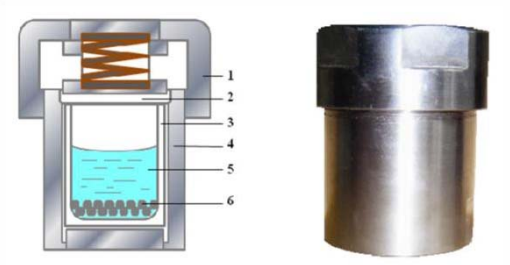

Figure 2.2 Schematic diagrams (left) and picture (right) of PTFE lined stainless steel static batch reactors. In the schematic diagram: 1 stainless steel cap, 2 PTFE cap, 3 PTFE body, 4 stainless steel body, 5 hydrothermal reaction fluid, 6 mineral samples.

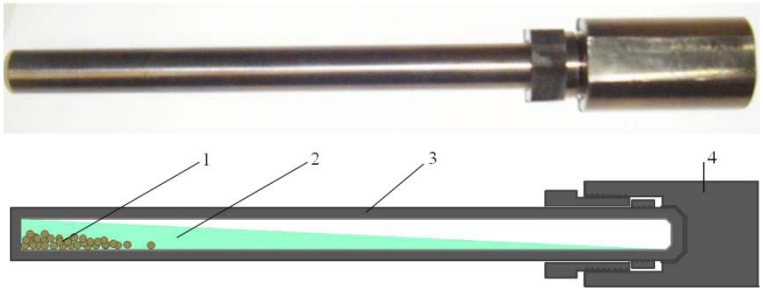

Figure 2.3 Image (above) and schematic diagrams (below) of Ti autoclave. In the schematic diagram: 1 mineral sample, 2 hydrothermal reaction fluid, 3 titanium body, 4 titanium cap.

The hydrothermal experiments were heated in electric muffle furnaces or ovens (Fig. 2.4) (both with a temperature regulation precision of ±2 °C) at a constant temperature for the duration of experiments. During the experiments, the pressures in the autoclaves reach autogenesis vapor pressures, which were bellow 86 bars at a temperature bellow of 300 °C. After reaction, the autoclaves were rapidly cooled by quenching in a large volume of cold

water (~10 L) for about 30 mins. The reacted fluid was collected after the autoclave was opened, the solids were rinsed three times with Milli-Q water and then three times with acetone before drying. Results from leaking runs were discarded.

Figure 2.4 Muffle furnaces (blue) and ovens (creamy) used in this work. These furnaces/ovens are programmable and the temperature can be controlled precisely within ± 2 ºC. The maximum working temperatures of the furnaces and ovens are 1150 ºC and 500 ºC, respectively.

2.4 Powder X-ray diffraction

Powder X-ray diffraction (XRD) is a very important laboratory technique for qualitative and quantitative analyses of powder samples. The analysis principle is based on the Bragg's law.

$$n\lambda = 2d\sin\theta \quad (1)$$

where n is an integer determined by the order given, λ is the wavelength of X-ray, d is the spacing of the crystal {hkl} planes, and θ is the diffraction angle. As shown in Figure 2.5, X-ray penetrating through or reflecting from the crystalline is diffracted by the crystal lattice planes {hkl}, the path difference between two waves undergoing constructive interference is given by $2d\sin\theta$. The diffraction occurs only when the path length of each wave ($2d\sin\theta$) is equal to an integer multiple of the wavelength. A diffraction pattern is obtained by measuring the intensity of diffracted waves as a function of diffraction angle. More details of XRD principle are given in Pecharsky and Zavalij (2003).

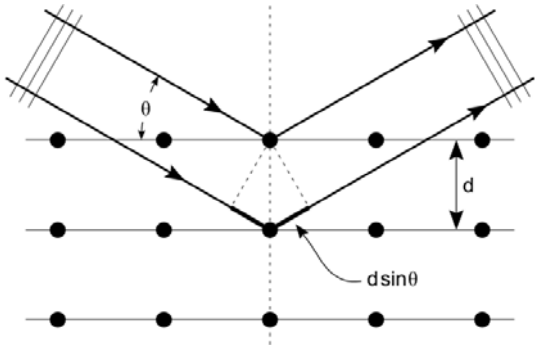

Figure 2.5 Bragg diffraction illustration.

In this project, room-temperature XRD patterns of the samples were collected using a Huber Guinier Image Plate G670 with Co$K\alpha_1$ radiation (λ = 1.78892 Å) in the Mineralogy Department, South Australian Museum (Fig. 2.6). The X-ray was generated by a PANalytical® X- ray tube at 35 kV and 34 mA, and filtered by an asymmetrically ground and curved quartz (SiO_2) monochromator. The function of the Huber Image Plate Camera is based on the image properties of a 330 × 15 mm X-Ray sensitive storage film, which is arranged in a focal circle 180 mm in diameter. The image information of a diffraction pattern on the film is read with a laser scanner. A focused laser beam (30 × 50 μm) excites photoluminescence on the film which is detected by a photomultiplier. The obtained signal

is amplified, digitized by an A/D-converter and transferred to the memory of the controlling computer. The image plate records diffraction patterns in the 2θ range from 4° to 100° with a step of 0.005°.

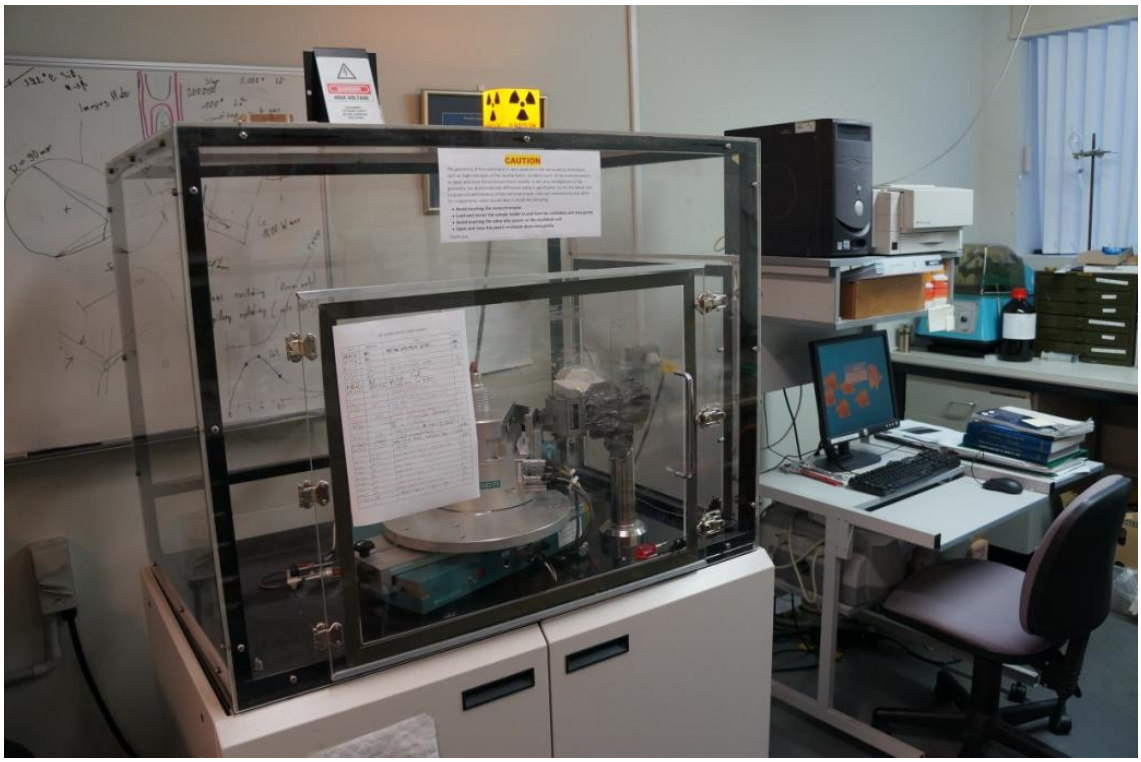

Figure 2.6 The Huber Guinier Imaging Plate Camera G670 used in this work.

For each test, around 5 mg specimen was ground under acetone in an agate mortar and spread on a MALAR® polyethylene terephthalate thin film. Powder diffraction data was collected for 20 min or recollected for longer periods to obtain an intensity of >2000 counts for the strongest peak in each pattern. The extent of the transformation was determined by the Rietveld quantitative phase analysis method (QPA) using either the program Rietica (Rietveld 1969; Hunter 1998) or the program of Topas (Bruker AXS 2009). Diffraction data in the 2θ range from 20 to 80° was used in the QPA. For the program Rietica, a pseudo-Voigt function with Howard asymmetry (Howard 1982) and

Shifted Cheby II function were adopted to model the peak shapes and the background, respectively. Zero shifts were taken from the refinements of the NBS internal or external Si standard. The refined parameters include: the scale factor (*S*), background, cell parameters, and the peak-shape parameters (*U, V, W*). For the program Topas, a Pseudo-Voigt function and a 6^{th} order Chebychev polynomial were used to model the peak shapes and the background, respectively. The zero shift and scale factors (S) were refined. The crystal data used for QPA were taken from ICSD database (sylvanite # 24646; calaverite #64681; gold #44362; hematite #82902; chalcopyrite #94554; bornite #24174; magnetite #31157; pyrite #15012; pyrrhotite #9146).

2.5 Scanning electron microscope (SEM)

A Philips XL30 field emission scanning electron microscope (FESEM) (Fig. 2.7) located in Adelaide Microscopy at the University of Adelaide, was used for characterization of the morphological and textural features of the samples. This microscope is equipped with a secondary electron (SE) detector, a backscattered electron (BSE) detector, an EDAX® Energy Dispersive X-ray Spectrometer (EDS), and the HKL Electron backscatter diffraction (EBSD) system. SE imaging was used to determine the surface morphology of the grains before and after the reaction. A BSE detector was used to characterize the cross sections of partially reacted grains. EDS was used for semi-quantitative chemical determinations with a 60 sec data acquisition time. The accelerating voltage was maintained at 20 kV and the working distance for above three modes was 10 mm. The HKL EBSD system was not used in this study. To prepare samples for surface morphology characterization, small fragments were stuck on a Φ12mm aluminum stub using a double

stick carbon tape and coated with a 15 nm thick carbon film. For textural studies, partially reacted grains were embedded in epoxy resin, sectioned with sand papers, polished with diamond paste (down to 1 μm) and evaporatively coated with 15 nm thick carbon films.

Figure 2.7 The Philips XL30 Field Emission Scanning Electron Microscope.

2.6 Electron backscatter diffraction (EBSD)

Electron backscatter diffraction (EBSD) is an advanced microanalysis technique applied in scanning electron microscopy to elucidate the texture or preferred orientation of crystalline or polycrystalline material. The principle of EBSD is based on the diffraction of some elastic backscattered electrons by the crystal lattice planes {hkl}, the record of these diffracted electrons on a fluorescent screen as unique diffraction patterns called “Kikuchi pattern”. According to Bragg’s law, the electron diffraction pattern represents the

crystalline structure, and the Kikuchi pattern may provide direct information about crystallographic orientation of the sample. By collecting Kikuchi patterns point by point in the analysis area and indexing each pattern with crystal models from ICSD, the crystallographic orientation distributions of the involved phases are obtained. In this project only pole figures were used to present the distributions of crystal orientation.

To identify the crystallographic orientations of different mineral phases, all EBSD analyses were carried out using a FEI Helios 600 NanoLab at Adelaide Microscopy, University of Adelaide (Fig. 2.8). The FEI Helios 600 is a dual-beam workstation combining a high-resolution field emission SEM (FESEM) with a focused ion beam (FIB), which can be used to sputter the surface of the sample down to nanoscale. The instrument is also equipped with an integrated EDS and EBSD system for gathering compositional data and crystallographic data. The samples were first polished with diamond paste (3 and 1 μm) for 20 min, and then polished with 0.04 μm colloidal silica suspension for 60 min in an attempt to remove the damaged layer. After polishing, the samples were coated with a 1.5 nm thick carbon film to minimize electron charging effect. For some samples with no colloidal silica suspension polishing step, the analysis area was milled with the focused Ga^+ ion beam (30 kV and 2.8 nA) at an angle of 10° to remove the surface layer distorted by the mechanical polishing process (Fig. 2.9a). The EBSD analyses were performed with sample surface tilted 70° relative to the horizontal and with a 20 kV accelerating voltage, 0.6 nA specimen current, and a 20 mm working distance. The EBSD patterns were recorded using a Nordlys camera (Fig. 2.9b). Crystal structural data for all minerals were taken from the ICSD database (sylvanite # 24646; calaverite #64681; gold #44362; hematite #82902; chalcopyrite #94554).

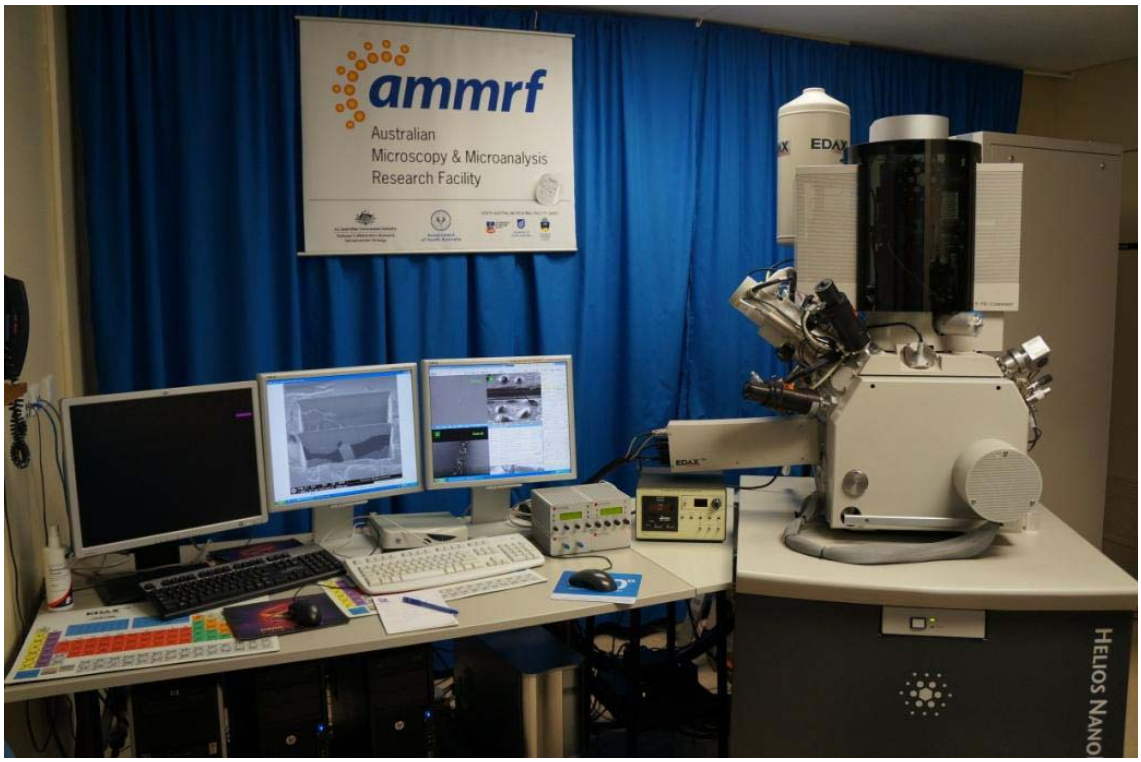

Figure 2.8 The FEI Helios NanoLab DualBeamTM FIB/SEM platform

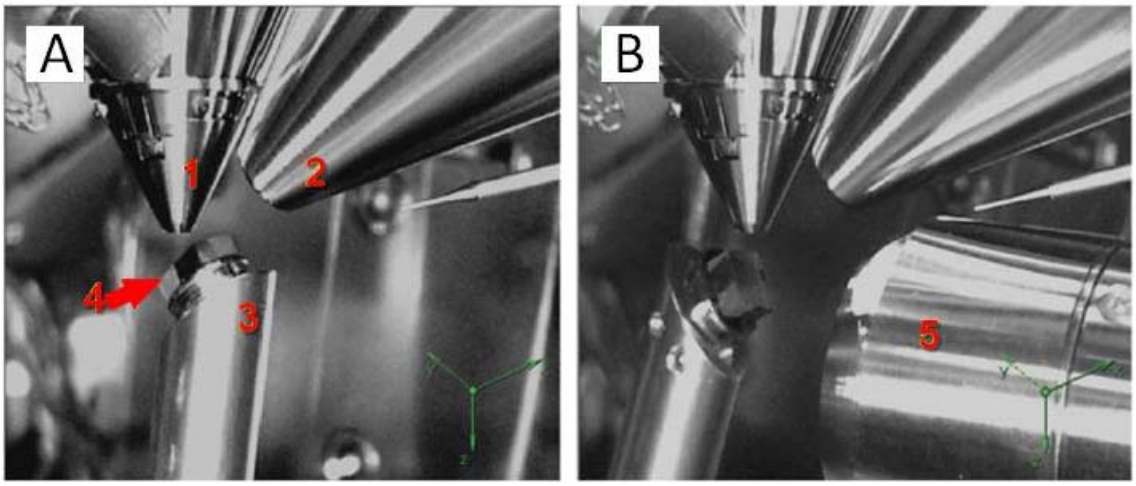

Figure 2.9 The images of (A) the milling view, (B) EBSD patterns collecting. 1. field emission electron beam gun, 2. Ga^+ ion beam gun, 3. sample stage with 3D movement mechanism, 4. sample, 5. Hikari EBSD camera.

2.7 Chemical analysis of solid products

The chemical composition and the element distribution of both the starting minerals and reacted grains were determined using a Cameca SX-51 electron probe microanalysis (EPMA) at Adelaide Microscopy, University of Adelaide (Fig. 2.10). The EPMA was equipped with four wavelength dispersive X-ray Spectrometers (WDS), one EDS and one reflected-light optical microscope. The carbon coated polished sample embedded in the resin blocks were prepared for analysis. EPMA was operated at an accelerating voltage of 20 kV and a beam current of ~20 nA. The counting time for each element and the background was set to 30 seconds.

Figure 2.10 The CAMECA SX51 electron microprobe at Adelaide Microscopy.

2.8 Solution inductively coupled plasma mass spectrometry (ICP-MS)

ICP-MS is a high speed, precise, and sensitive technique to measure the concentrations of elements in solution. The analysis for ICP-MS can be used to measure trace elements concentration as low as one part per trillion (ppt) or to determine the composition of an unknown sample by a quick scanning for more than 70 elements. The analysis is done by atomizing and ionizing the nebulized sample with inductively coupled plasma (such as the high temperature argon plasma) and measuring the mass to charge ratio (M/Z) using an electron multiplier detector. The concentration for the element in the sample is given by comparing the obtained M/Z for a particular ions compared with a calibration curve.

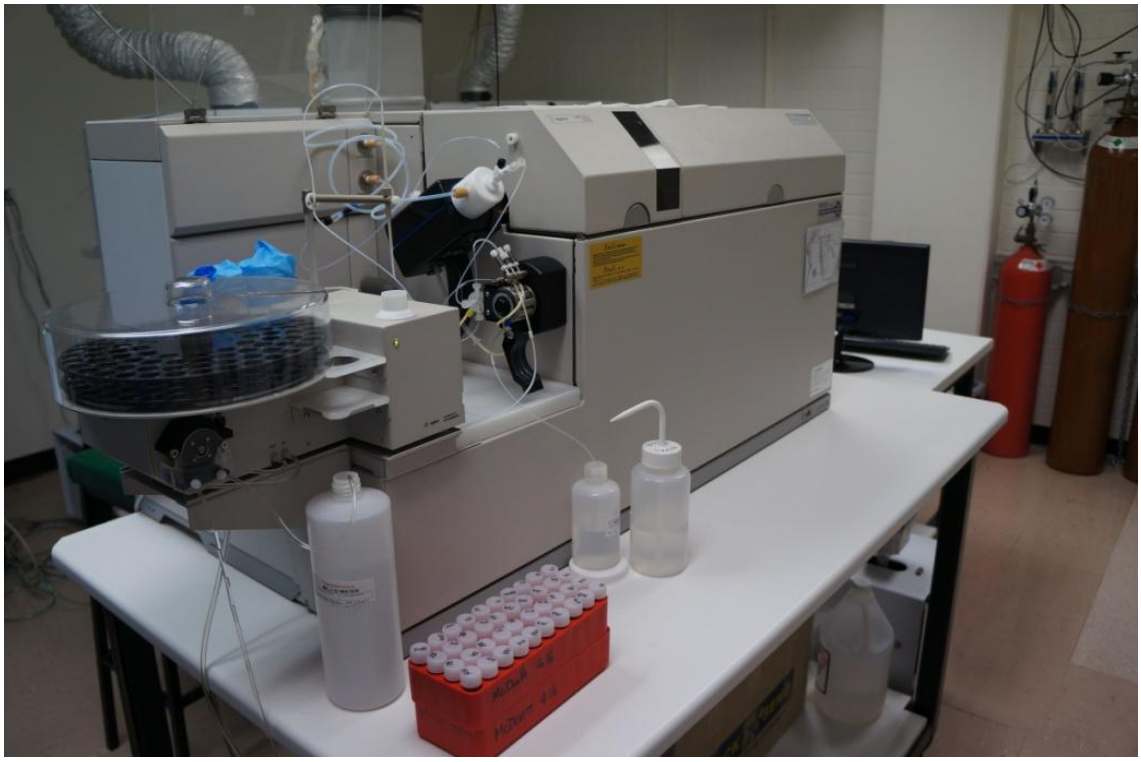

Figure 2.11 The Agilent 7500cs solution ICP-MS instrument at Adelaide Microscopy Centre

An Agilent 7500 ICP-MS (Fig. 2.11) at Adelaide Microscopy was used to measure the concentrations of Au, Ag and Te (Chapter 3). Standard solutions of 500, 200, 100, 50, 20, 10, 5, and 0 ppb (blank) of Au, Ag, and Te were prepared for calibration purpose. An indium solution (200 ppb) was used as an internal standard. Depending on their compositions, solutions were run either unprocessed, or were diluted by factors of 100 or 1000 times using 2% HNO_3.

2.9 References

Bethke, C.M. (2008) Geochemical and biogeochemical reaction modeling (2nd edition). 564 p. Cambridge University Press, New York.

Brugger, J., Etschmann, B., Liu, W., Testemale, D., Hazemann, J.L., Emerich, H., van Beek, W., and Proux, O. (2007) An XAS study of the structure and thermodynamics of Cu(I) chloride complexes in brines up to high temperature (400 °C, 600 bar). Geochimica et Cosmochimica Acta, 71(20), 4920-4941.

Bruker AXS (2009): TOPAS V4.2: General profile and structure analysis software for powder diffraction data. Bruker AXS GmbH, Karlsruhe, Germany.

Howard, C. (1982) The approximation of asymmetric neutron powder diffraction peaks by sums of Gaussians. Journal of Applied Crystallography, 15, 615-620.

Hunter, B.A. (1998) Rietica-A visual Rietveld program. International Union of Crystallography Commission on Powder Diffraction Newsletter, 20, 21-23.

Pecharsky, V.K. and Zavalij, P.Y. (2003) Fundamentals of powder diffraction and structural characterization of materials. Kluwere Academic Publishers, Boston.

Rietveld, H. (1969) A profile refinement method for nuclear and magnetic structures. Journal of Applied Crystallography, 2(2), 65-71.

Shvarov, Y. and Bastrakov, E. (1999) HCh: a software package for geochemical modelling. User's guide. AGSO record, 25, 60.

CHAPTER 3

Statement of Authorship

Title of Paper	**Dissolution-reprecipitation vs. solid-state diffusion: Mechanism of mineral transformations in sylvanite, $(AuAg)_2Te_4$, under hydrothermal conditions.**
Publication Status	◉ Published, ○ Accepted for Publication, ○ Submitted for Publication, ○ Publication style
Publication Details	**Zhao, J., Brugger, J., Xia, F., Ngothai, Y., Chen, G., and Pring, A., (2013) Dissolution-reprecipitation vs. solid-state diffusion: Mechanism of mineral transformations in sylvanite, $(AuAg)_2Te_4$, under hydrothermal conditions. American Mineralogist, 98, 19-32.**

Author Contributions

By signing the Statement of Authorship, each author certifies that their stated contribution to the publication is accurate and that permission is granted for the publication to be included in the candidate's thesis.

Name of Principal Author (Candidate)	**Jing Zhao**		
Contribution to the Paper	**Designed and performed experiments, interpreted and processed data, wrote manuscript.**		
Signature		Date	**6 August 2013**

Name of Co-Author	**Joël Brugger**		
Contribution to the Paper	**Supervised development of work, helped in data interpretation and manuscript evaluation.**		
Signature		Date	**5 July 2013**

Name of Co-Author	**Fang Xia**		
Contribution to the Paper	**Helped to evaluate and edit the manuscript.**		
Signature		Date	**6 August 2013**

Name of Co-Author	**Yung Ngothai**		
Contribution to the Paper	**Supervised development of work and helped in manuscript evaluation.**		
Signature		Date	**6 August 2013**

Name of Co-Author	**Guorong Chen**		
Contribution to the Paper	**Helped in manuscript evaluation.**		
Signature		Date	**12 August 2013**

Name of Co-Author	**Allan Pring**		
Contribution to the Paper	**Supervised development of work, helped in data interpretation and manuscript evaluation, and acted as corresponding author.**		
Signature		Date	**8 August 2013**

Zhao, J., Brugger, J., Xia, F., Ngothai, Y., Chen, G. & Pring, A. (2013) Dissolution reprecipitation vs. solid-state diffusion: mechanism of mineral transformations in sylvanite, $(AuAg)_2Te_4$, under hydrothermal conditions.
American Mineralogist, v. 98(1), pp. 19-32

CHAPTER 4

Statement of Authorship

Title of Paper	**Experimental study of the formation of chalcopyrite and bornite via the sulfidation of hematite: mineral replacements with large volume increase.**
Publication Status	◉ Published, ○ Accepted for Publication, ○ Submitted for Publication, ○ Publication style
Publication Details	**Zhao, J., Brugger, J., Chen, G., Ngothai, Y., and Pring, A. (2014) Experimental study of the formation of chalcopyrite and bornite via the sulfidation of hematite: mineral replacements with large volume increase. American Mineralogist, 99, 343-354.**

Author Contributions

By signing the Statement of Authorship, each author certifies that their stated contribution to the publication is accurate and that permission is granted for the publication to be included in the candidate's thesis.

Name of Principal Author (Candidate)	**Jing Zhao**		
Contribution to the Paper	**Designed and performed experiments, interpreted and processed data, wrote manuscript.**		
Signature		Date	**6 August 2013**

Name of Co-Author	**Joël Brugger**		
Contribution to the Paper	**Supervised development of work, helped in data interpretation and manuscript evaluation.**		
Signature		Date	**5 July 2013**

Name of Co-Author	**Guorong Chen**		
Contribution to the Paper	**Helped in manuscript evaluation.**		
Signature		Date	**12 August 2013**

Name of Co-Author	**Yung Ngothai**		
Contribution to the Paper	**Supervised development of work and helped in manuscript evaluation.**		
Signature		Date	**6 August 2013**

Name of Co-Author	**Allan Pring**		
Contribution to the Paper	**Supervised development of work, helped in data interpretation and manuscript evaluation, and acted as corresponding author.**		
Signature		Date	**8 August 2013**

Zhao, J., Brugger, J., Chen, G., Ngothai, Y. & Pring, A. (2014) Experimental study of the formation of chalcopyrite and bornite via the sulfidation of hematite: mineral replacements with a large volume increase.
American Mineralogist, v. 99(2-3), pp. 343-354

CHAPTER 5

Statement of Authorship

Title of Paper	**The replacement of chalcopyrite by bornite under hydrothermal conditions.**
Publication Status	○ Published, ○ Accepted for Publication, ○ Submitted for Publication, ◉ Publication style
Publication Details	**Zhao, J., Brugger, J., Ngothai, Y., and Pring, A. (2013)** **The replacement of chalcopyrite by bornite under hydrothermal conditions.**

Author Contributions

By signing the Statement of Authorship, each author certifies that their stated contribution to the publication is accurate and that permission is granted for the publication to be included in the candidate's thesis.

Name of Principal Author (Candidate)	**Jing Zhao**		
Contribution to the Paper	**Designed and performed experiments, interpreted and processed data, wrote manuscript.**		
Signature		Date	**6 August 2013**

Name of Co-Author	**Joël Brugger**		
Contribution to the Paper	**Supervised development of work, helped in data interpretation and manuscript evaluation.**		
Signature		Date	**5 July 2013**

Name of Co-Author	**Yung Ngothai**		
Contribution to the Paper	**Supervised development of work and helped in manuscript evaluation.**		
Signature		Date	**6 August 2013**

Name of Co-Author	**Allan Pring**		
Contribution to the Paper	**Supervised development of work, helped in data interpretation and manuscript evaluation, and acted as corresponding author.**		
Signature		Date	**8 August 2013**

CHAPTER 5 THE REPLACEMENT OF CHALCOPYRITE BY BORNITE UNDER HYDROTHERMAL CONDITIONS

JING ZHAO[1,2], JOËL BRUGGER[1,3], YUNG NGOTHAI[2], AND ALLAN PRING[1,4*]

[1]Department of Mineralogy, South Australian Museum, North Terrace, Adelaide, SA 5000, Australia

[2]School of Chemical Engineering, University of Adelaide, Adelaide, SA 5005, Australia

[3]School of Earth and Environmental Sciences, University of Adelaide, Adelaide, SA 5005, Australia

[4]School of Chemistry and Physics, University of Adelaide, Adelaide, SA 5005, Australia

*Corresponding author: allan.pring@samuseum.sa.gov.au

Abstract

Intergrowths of chalcopyrite and bornite in nature generally exhibit textures indicative of replacement reactions in the presence of a fluid, and are believed to occur either by bornite replacing chalcopyrite or vice versa. Based on the successful hydrothermal synthesis of chalcopyrite and bornite, we report the replacement of chalcopyrite by bornite in solutions containing Cu(I) (as a chloride complex) and hydrosulfide over the temperature range 200-300 °C. Results show that chalcopyrite was replaced by bornite under all studied conditions. The reaction proceeds via a coupled dissolution-reprecipitation reaction mechanism and with some additional overgrowth of bornite.

The bornite product is Cu-rich corresponding to compositions in the bornite-digenite solid solution (*bdss*) and is temperature dependent; at 250 ˚C a composition of $Bn_{50}Dg_{50}$ was obtained, while at 300 ˚C the composition was $Bn_{90}Dg_{10}$. When the *bdss* formed at 300 °C for 24 hrs was further annealed under hydrothermal conditions at 150 ˚C and 200 ˚C for 24 to 120 hrs, the solid solution exsolved into digenite lamella in a bornite host. The exsolution textures observed in this study are very similar to those reported in dry sealed tube experiments on *bdss* driven by solid-state diffusion. The rates of exsolution under hydrothermal conditions are approximately 25 times more rapid than under comparable dry annealing conditions. This illustrates the important role of the hydrothermal recrystallization in the kinetics of ore texture development.

Keywords: chalcopyrite, bornite, mineral replacement, hydrothermal, bornite-digenite solid solution, exsolution.

5.1 Introduction

Chalcopyrite ($CuFeS_2$) and bornite (Cu_5FeS_4) are the most abundant primary copper-bearing sulfides across a wide range of ore deposit types. Both minerals are part of the same broad sulfide structural family and their structures can be derived from the zinc blende structure, a cubic close-packed array of S atoms with metal cations occupying half of the tetrahedral sites in the S lattice. Chalcopyrite ($CuFeS_2$) is an ordered zinc blende derivative, with the ordering of the Fe and Cu atoms over half of the available tetrahedral sites leading to a tetragonal superstructure with the until cell repeat doubled in one direction compared to the parent cubic zinc blende cell (a *2a* supercell). Above 265 °C bornite (Cu_5FeS_4) and digneite (Cu_9S_5) form a complete solid solution, the bornite-digenite solid solution (*bdss*) structure is based on a cubic close-packed array of S atoms with Cu, Fe and a metal vacancy randomly distributed over all eight of the available tetrahedral interstices in a "stuffed zinc blende" structure or antifluorite-type structure. Between 200 °C and 265 °C bornite exists as an intermediate cubic phase, but below 200 °C bornite undergoes a complex ordering transition leading to an orthorhombic 2*a*4*a*2*a* superstructure (*Pbca*) of the basic zinc blend-type cell. The digenite end of the solid solution is characterized by a 5*a* cubic superstructure (*Fm*3*m*) and it appears that a small amount of Fe substituting for Cu stabilizes the superstructure (See Grguric et al. 2000 and references there in),

In nature the textures of some chalcopyrite-bornite assemblages can be interpreted in terms of solid state exsolution or unmixing processes, e.g. bornite intergrown with a maze of minute chalcopyrite needles (Ramdohr 1980; Cook et al. 2011). The majority of chalcopyrite and bornite intergrowths, however, show textures consistent with fluid-

mediated replacement reactions. For example, the replacement of chalcopyrite by bornite was reported by Halbach et al. (1998) in massive sulfide samples from Indian Ocean seafloor hydrothermal vents. Oszczepalski (1999) studied the origin of Kupferschiefer ore in Poland and pointed out that chalcopyrite was preferentially replaced by bornite, which would be further replaced by Cu-S type sulfides such as chalcocite, covellite and digenite. Indeed, chalcopyrite-bornite intergrowths found in many typical primary copper sulfide ores are believed to have formed either by bornite replacing chalcopyrite or vice versa (Ramdohr 1980; Robb 2005).

The transformation mechanism of chalcopyrite and bornite intergrowths has been the subject of only a small number experimental of studies under both solid-state and hydrothermal conditions. For examples, Amcoff (1988) undertook a detailed study on the solid-state replacement of chalcopyrite by bornite between 200 and 500 °C, showing that chalcopyrite reacted with chalcocite to form bornite under relatively reducing conditions. The reaction is structurally controlled by the inter-diffusions of Fe and Cu in the S lattices. Roberts (1963) conducted a series of experiments to investigate the transformation of chalcopyrite into bornite in copper sulfate aqueous solution at low temperature (<150 °C), showing that chalcopyrite could be converted to bornite after six days at 100 °C, and that the product bornite could be converted back to chalcopyrite by adding an excess of sulfide and ferrous ions under the same conditions.

Based on previous studies on mineral replacement reactions of a range of important sulfide minerals including pyrite (Qian et al. 2010, 2011, 2013), violarite (Tenailleau et al. 2006, Xia et al. 2009; Brugger et al. 2010) and marcasite (Qian et al. 2011), we recently undertook an experimental study of the formation of chalcopyrite via hydrothermal

processes, more specifically the replacement of hematite by chalcopyrite upon reaction with Cu-S-rich fluids in the temperature interval 200 to 300 °C (Zhao et al. 2013a). Here, we investigated the replacement of chalcopyrite by bornite under hydrothermal conditions at temperature up to 300 °C and vapor saturated pressures up to 86 bar. The aim here is to explain the formation of bornite over a wide range of physical and chemical hydrothermal conditions. In this paper we will refer in general terms to compositions in the bornite-digneite solid solution (*bdss*) as bornite, when discussing specific compositions in the solid solution series we will denote them by their bornite and dignite factions (Bn_xDg_{1-x}).

5.2 Samples and methods

5.2.1 Preparation of starting samples

Chalcopyrite from Moonta Mines, South Australian (SA Museum sample G22621) was used as starting material throughout this study. The purity of chalcopyrite was established using a powder X-ray diffraction and electron probe microanalysis. The average composition of chalcopyrite is $Cu_{1.04(8)}Fe_{1.05(2)}S_{1.91(4)}$ (mean of 24 points analysis). Chalcopyrite was crushed and fragments were washed in an ultrasonic bath, and carefully sieved into a 125 to 150 µm size fraction. All other chemical reagents including buffer solutions used in experiments were analytical reagents. The buffer solutions were prepared as described in Zhao et al. (2013a), and their compositions are given in Table 5.1. The pH values shown in Table 5.1 were measured at room temperature, while the pH values at reaction temperatures listed in Table 5.2 were calculated using the HCh geochemical modeling software (Shvarov and Bastrakov 1999).

Table 5.1 Composition of buffer solutions

pH at 25°C		Buffer ID	Components					
calc.	**meas**		**Acid**	**C/m**	**Basic**	**C/m**	**Addition**	**C/m**
2.10	2.10	CP2	H_3PO_4	0.522	$NaH_2PO_4 \cdot 2H_2O$	0.477	NaCl	1.007
3.99	3.86	CA4	CH_3COOH	0.825	CH_3COONa	0.170	NaCl	1.000
7.03	6.90	CP7	$NaH_2PO_4 \cdot 2H_2O$	0.340	Na_2HPO_4	0.655	NaCl	1.000
10.10	9.80	CB10	H_3BO_3	0.533	NaOH	0.449	NaCl	1.000

5.2.2 Hydrothermal experiments

For each run, 10 mg of chalcopyrite crystal fragments (55 μmoles), 21.5 mg CuCl(s) (217 μmoles), 0.1890 g thioacetamide and 5 mL reaction solution were carefully weighted and added into an 8 mL titanium autoclave in an argon-filed anoxic glove box. The sealed cells were left in electric Muffle furnaces (with a temperature regulation precision of 2 °C) at a constant temperature over the duration of experiments. To test the effect of cooling history on reaction textures and products, two sets of experiments were conducted at 300 °C for 24 hrs in buffer solution CB10; then the temperature was decreased to 150 °C (Runs G1-G3) or 200 °C (Runs G4-G6), and maintained at these temperatures for different annealing times (shown in Table 5.4). At the end of the runs, the autoclaves were quenched to room temperature in a large volume of cold water (~10 L) for 20 minutes. The solids were rinsed three times using Milli-Q water followed by acetone. Results from leaking runs were not considered in this study. During the experiments, the pressures in the autoclaves are autogenously pressures, which are around 86 bar at 300 °C. To investigate the effects of pH and temperature on the reaction rate and on the composition of the bornite, experiments were undertaken in CP2, CA4, CP7 and CB10 buffer solutions at both 250 °C and 300 °C for 24 hrs.

5.2.3 Analysis methodology

The extent of the transformation was determined by Rietveld quantitative phase analysis (QPA) of powder X-ray diffraction data using the program Topas (Bruker AXS 2009). Characterization of the morphological and textural features of reacted grains was undertaken using a Philips XL30 field emission scanning electron microscope (FESEM) at Adelaide Microscopy, University of Adelaide. The chemical compositions of products were determined using a Cameca SX-51 electron probe microanalysis (EPMA) at Adelaide Microscopy, University of Adelaide.

Table 5.2 Reaction conditions and results*

No.	Run No.	T/(°C)	Buffer Solution#	Solution pH§	Time (hrs)	NaCl /m	Products and weight percentage (%)‡
C1	C250D2PH1D	250	CP2	3.31	24	1	Cpy(97)Bn(3)
C2	C250D4PH1D	250	CA4	4.17	24	1	Cpy(95)Bn(5)
C3	C250D7PH1D	250	CP7	6.09	24	1	Cpy(95)Bn(5)
C4	C250D10PH1D	250	CB10	7.08	24	1	Cpy(84)Bn(16)
C5	C300D2PH1D	300	CP2	3.75	24	1	Cpy(73)Bn(27)
C6	C300D4PH1D	300	CA4	4.39	24	1	Cpy(67)Bn(33)
C7	C300D7PH1D	300	CP7	6.23	24	1	Cpy(28)Bn(72)
C8	C300D10PH4HS	300	CB10	7.43	4	1	Cpy(41)Bn(59)
C9	C300D10PH6HS	300	CB10	7.43	6	1	Cpy(68)Bn(32)
C10	C300D10PH18HS	300	CB10	7.43	18	1	Cpy(54)Bn(46)
C11	C300D10PH1D	300	CB10	7.43	24	1	Cpy(23)Bn(77)
C12	C300D10PH2D	300	CB10	7.43	48	1	Cpy(23)Bn(77)
C13	C300D10PH3D	300	CB10	7.43	72	1	Cpy(29)Bn(71)
C14	C300D10PH4D	300	CB10	7.43	96	1	Cpy(39)Bn(61)
C15	C300D10PH5D	300	CB10	7.43	120	1	Cpy(5)Bn(95)
C16	C300D10PH6D	300	CB10	7.43	144	1	Cpy(11)Bn(90)
C17	C150D10PH4D	150	CB10	7.47	72	1	Cpy(97)Bn(3)
C18	C150D10PH6D	150	CB10	7.47	96	1	Cpy(96)Bn(4)
C19	C200D10PH4D	200	CB10	7.16	120	1	Cpy(89)Bn(11)
C20	C200D10PH6D	200	CB10	7.16	144	1	Cpy(88)Bn(12)

* The mass of chalcopyrite, CuCl and thioacetamide are 10 mg, 21.5mg and 0.1890g, respectively. The volume of fluid is 5ml.
# "P" phosphate buffer solution, "A" acetate buffer solutions, and "B" borate buffer solution. For respective compositions refer to Table 5.1.
§ pH values were calculated at reaction temperature using HCh software.
‡ Obtained from powder X-ray diffraction patterns by Rietveld quantitative phase analysis. "Cpy" stands for chalcopyrite phase, "Bn" for bornite, and "Hm" for hematite. Error on the phase proportion is estimated to 5% on each determination.

5.3 Results

5.3.1 The replacement of chalcopyrite by bornite

Under all conditions explored in this study, chalcopyrite was replaced by bornite. For experiments conducted at 300 °C using solution CB10, the proportion of the products shows a first order dependence on the reaction time (Runs C8-C16, shown in Table 5.2). For example, 32 wt% of chalcopyrite was replaced by bornite (Run C9) after 6 hr reaction, and the extent increased to 77 wt% after 24 hr reaction (Run C11), and then remained at this value for further 48 hrs.

Under the SEM, the original chalcopyrite gains are characterized by sharp-edges and smooth conchoidal surfaces (Fig. 5.1a). After 72 hr reaction in buffer solution CB10 at 300 °C (Run C1), they consist of compound particles cemented together by a layer of Bornite (Fig. 5.1b). The newly formed bornite consists of microcrystals ranging in size up to 2 μm across (Fig. 5.1c). Back-scattered electron images of cross sections of partially reacted grains show a thick bornite layer coating a chalcopyrite core (Fig. 5.2a). The replacement reaction initiates at the outer surface of the original chalcopyrite grain and the cracks within chalcopyrite grain are in-filled with bornite. The reaction interface between chalcopyrite and bornite presents a sharp boundary (Fig. 5.2b), and the replacing bornite shows porosity (Fig. 5.2c). Note that in these back-scattered images that there is no evidence of chemical zoning in the bornite rims, and the composition of the bornite is homogeneous (Table 5.3).

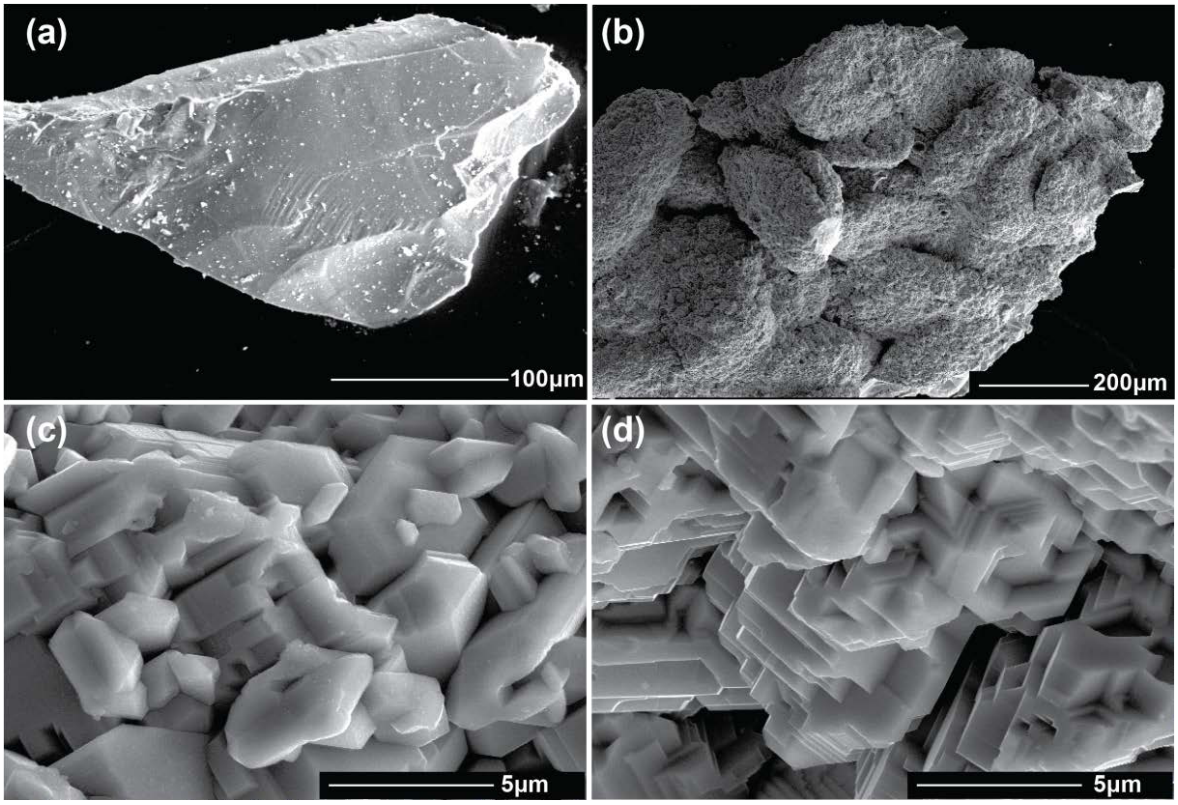

Figure 5.1 Secondary electron images of (a) unreacted chalcopyrite with sharp edges, (b) partially reacted chalcopyrite grains, (c-d) the surfaces of reacted chalcopyrite grains under hydrothermal conditions, showing fine bornite crystals varying in size up to 2 μm across.

Table 5.3 Compositions of products

Run No.	Points	Composition	Weight percentages of elements in products (wt%) [mean(range)]		
			Cu	Fe	S
C1	7	$Cu_{6.03(8)}Fe_{0.59(8)}S_{4.00}$	69.60(68.63-70.58)	6.04(7.04-8.49)	23.29(22.38-23.15)
C2	4	$Cu_{6.18(9)}Fe_{0.58(5)}S_{4.00}$	70.05(67.37-70.67)	5.85(5.74-5.91)	22.86(22.43-23.28)
C4	8	$Cu_{6.30(7)}Fe_{0.50(6)}S_{4.00}$	70.81(70.44-71.24)	4.92(4.57-5.00)	22.67(22.43-22.87)
C5	6	$Cu_{5.21(6)}Fe_{0.85(4)}S_{4.00}$	65.74(65.47-65.93)	9.42(9.27-9.55)	25.46(25.19-25.54)
C6	15	$Cu_{5.20(9)}Fe_{0.85(5)}S_{4.00}$	65.81(65.06-66.54)	9.33(9.05-10.11)	25.52(25.19-25.94)
C7	10	$Cu_{5.38(8)}Fe_{0.89(7)}S_{4.00}$	65.76(65.45-65.78)	9.58(9.38-9.87)	24.66(24.42-25.03)
C11	13	$Cu_{5.26(9)}Fe_{0.84(6)}S_{4.00}$	65.89(65.62-66.33)	9.29(8.47-9.64)	25.27(24.88-25.91)

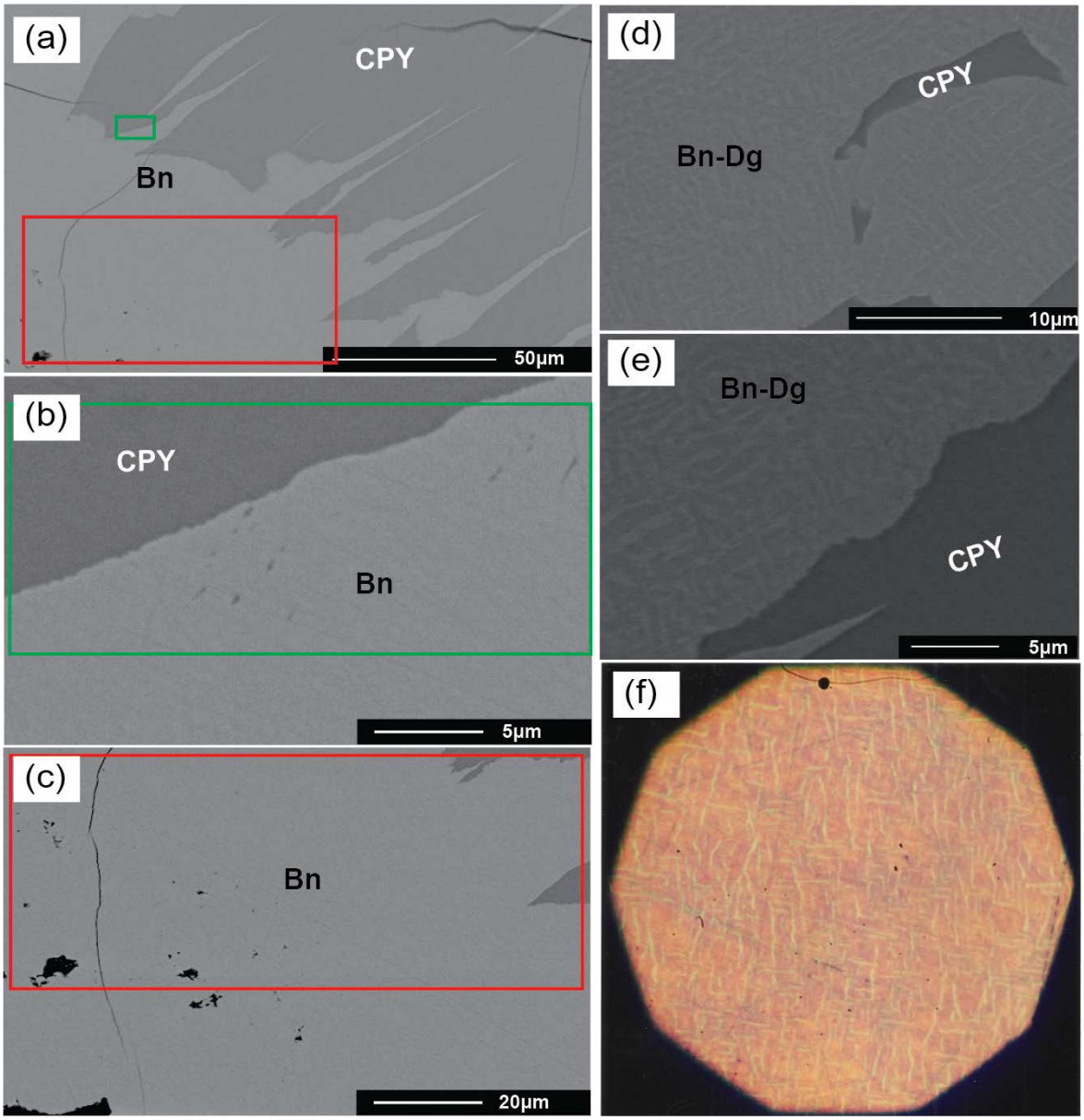

Figure 5.2 Back scattered electron images of the cross section of (a) a partially reacted grain showing the replacement of chalcopyrite (dark grey) by bornite (light grey) from the outside to the core, (b) sharp boundaries between chalcopyrite and bornite (magnified image of area shown in green rectangle in Figure 5.2a), and (c) newly formed bornite with isolated pores (magnified image of area shown in red rectangle in Figure 5.2a), (d-e) a partially reacted grain (Run G2) showing the replacement of chalcopyrite (dark grey) by bornite (grey)-digenite (light grey lines) intergrowth. (f) The optical image of a $Bn_{90}Dg_{10}$ sample annealed at 180 °C for 11 weeks showing characteristic "basket weave" microstructure defined by the exsolution of bornite and digenite. Filed of view is 75 microns (Image: Grguric and Putnis 1999).

5.3.2 Controls on the rate of transformation and on the composition of the products

Experimental runs undertaken over a range of temperatures and pHs show that the replacement reaction is favored by higher temperature (Runs C1-C7 and C11). As shown in Figure 5.3, the greatest reaction extent occurs in buffer solution CB10 at 300 ˚C (Run C11), showing 77% replacement, compared to only 16% at 250 ˚C (Run C4). The lowest extent of transformation was associated with the CP2 buffer solution, where only 3% replacement was obtained after 24 hrs at 250 ˚C (Run C1) and 27% at 300 ˚C (Run C5). The reaction extent for runs using buffer solution CA4 increased from 5% at 250 ˚C (Run C2) to 33% at 300 ˚C (Run C6), and using buffer solution CP7 increased from 5% at 250 ˚C (Run C3) to 72% at 300 ˚C (Run C6). The hydrolysis rate of thioacetamide to form HS^-/H_2S(aq) is fast compared to the rates of these replacement reactions over the temperature range, and the above results truly reflect the effect of temperature on the replacement reaction rate.

Electron microprobe analyses of showed that the composition of bornite did not vary with solution pH. The composition of the bornite in run C11 ($pH_{300°C}$7.43) is $Cu_{5.26(9)}Fe_{0.84(6)}S_{4.00}$ (based on the mean of 13 point analyses), which corresponds to $Bn_{90}Dg_{10}$ in the bornite-digenite solid solution (*bdss*, shown in Table 5.3). The compositions of bornite in runs C5-C7 at 300˚C are $Cu_{5.21(6)}Fe_{0.85(4)}S_{4.00}$, $Cu_{5.20(9)}Fe_{0.85(5)}S_{4.00}$ and $Cu_{5.38(8)}Fe_{0.89(7)}S_{4.00}$, respectively. However, the composition of bornite appears to be related to reaction temperature. The compositions of bornite in run C4 at $pH_{250°C}$7.08 is $Cu_{6.30(7)}Fe_{0.50(6)}S_{4.00}$ (shown in Table 5.3), which corresponds to $Bn_{50}Dg_{50}$ in the bornite-digenite solid solution.

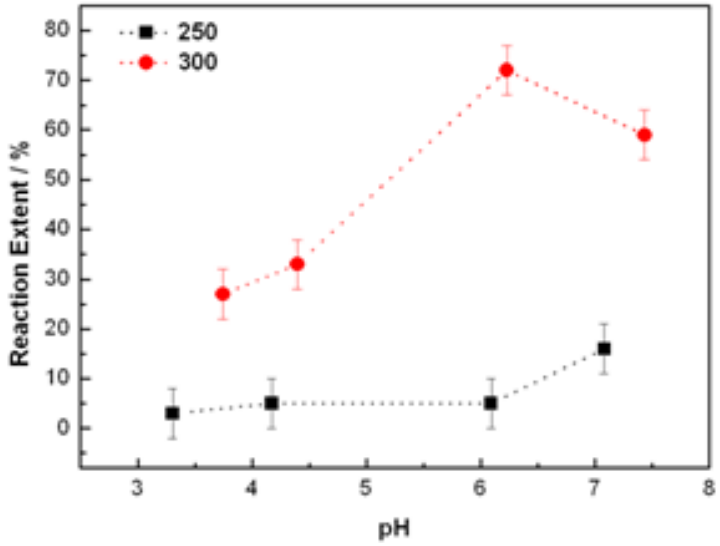

Figure 5.3 Reaction extents as a function of temperature and pH. Experiments were conducted for 24 hrs at both 250˚C and 300˚C for different fluid compositions (Runs C1-C7 and C11). The pH values of different fluid compositions at reaction temperature were calculated using HCh and shown in Table 5.2. Errors of the reaction extent (3-σ; ±5%) are plotted at each point.

5.3.3 The exsolution of *bdss* to bornite and digeniten

In reactions that were initiated at 300 °C for 24 hrs and then cooled to and annealed at 150 °C or 200 °C for 24 to 120 hrs (G1-G6), the QPA results showed that chalcopyrite was replaced by bornite and digenite (Table 5.4). For example, Run G1 undertaken at 300 °C for 24 hrs and then annealed at 150 °C for 24 hrs yielded 52 wt% bornite and 28 wt% digenite. Compared to Run C11 (conducted at 300˚C for 24 hrs) where 77wt% of chalcopyrite was replaced by bornite, rather than altering the overall reaction extents, the annealing of G1 promotes the break down of *bdss* and the formation of digenite and bornite. However, the experiments undertaken just at 150 or 200 ˚C for continuous 96 and 120 hrs, without an initial period at 300 ˚C, show relative low reaction extents (Runs C17-C20). For example, only 12 wt% of chalcopyrite was replaced by bornite in solution CB10 at 200 ˚C after 120 hrs. Back-scattered electron images of cross sections of partially reacted grains in runs G1-G6 show the replacement of chalcopyrite by a matrix of

stoichiometic bornite with exsolution lamellae of digenite (e.g., Figs. 5.2d-5.2e). The composition of the bornite matrix was $Cu_{4.95(5)}Fe_{0.99(2)}S_4$ (mean of 15 points), close to the stoichiometry of bornite Cu_5FeS_4, while that of the digenite was $Cu_{8.50(9)}Fe_{0.15(3)}S_5$ (mean of 15 points) which corresponds to the Cu-poorest composition reported for several natural digenite by Morimoto and Gyobu (1971).

Table 5.4 Reaction conditions and results for the annealing*

No.	Run No.	T/(°C)	Solution pH§	Time (day)	Products and weight percentage (%)‡
G1	300-150D10PH1D	150	7.47	1D	Cpy(19)Bn(52)Dg(28)
G2	300-150D10PH3D	150	7.47	3D	Cpy(15)Bn(60)Dg(25)
G3	300-150D10PH5D	150	7.47	5D	Cpy(58)Bn(30)Dg(12)
G4	300-200D10PH1D	200	7.16	1D	Cpy(47)Bn(30)Dg(22)
G5	300-200D10PH3D	200	7.16	3D	Cpy(14)Bn(48)Dg(38)
G6	300-200D10PH5D	200	7.16	5D	Cpy(18)Bn(53)Dg(28)

Note:
* All experiments were undertaken at 300 °C for 24 hrs using solution CB10 and then annealed at 150 and 200 °C for 24 to 120 hrs under hydrothermal conditions.
§ pH values were calculated at reaction temperature using HCh software.
‡ Obtained from powder X-ray diffraction patterns by Rietveld quantitative phase analysis. "Cpy" stands for chalcopyrite phase, "Bn" for bornite, and "Dg" for digenite. Error on the phase proportion is estimated to 5% on each determination.

5.4 Discussion

5.4.1 Reaction mechanism

The replacement of chalcopyrite by bornite under hydrothermal conditions is characterized by a sharp reaction front between chalcopyrite and bornite, with no visible gap at the reaction front. The reaction starts at the surface of the chalcopyrite grains and proceeds to the crystal core. Cracks within chalcopyrite grains are in-filled with bornite indicating that the replacement proceeds along cracks within the chalcopyrite. These textural characteristics indicate that bornite immediatedly precipitated as chalcopyrite dissolved. Hence, the replacement of chalcopyrite by bornite is an example of an interface coupled dissolution-reprecipitation (ICDR) reaction. The dissolution of the parent phase is spatially

tightly coupled with the precipitation of the product phase at the reaction front, and the reaction rate is controlled by the relative solubilities of the parent and product phases (Putnis 2009). ICDR reactions often show pseudomorphic preservation of grain shape and textural features, when there is near constant bulk volume preservation, such as the transformation process of pentlandite to violarite under mild hydrothermal conditions (Xia et al. 2009). Zhao et al. (2013a) discuss the volume changes associated with mineral replacement reactions and calculate that volume increase for the formation of chalcopyrite from hematite is 290%, based on the conservation of Fe. For the transformation of chalcopyrite to bornite, calculated on the basis of the preservation of Fe, the volume increase is of the order of 226%, however, if the volume change is calculated on the basis of the preservation of the S lattice, which is common to both chalcopyrite and bornite, then the volume increase is only 13%. Preserving the S lattice during the replacement requires the loss of 2 of the 4 Fe atoms in the chalcopyrite cell to solution at the reaction interface and the addition of 6 Cu atoms per cell from solution. In ICDR reactions, when precipitation takes place close (within microns) to the site of dissolution, the reactions products are porous, enabling mass and fluid transport between the reaction front and the bulk solution. In this transformation, the bornite product is compact, with some scattered pores (Figs. 5.2b and 5.2c). What is unclear is whether some of the porosity in the product bornite has been destroyed during polishing or healed during the quenching process, but the porosity must have been present to enable fluid transport to the reaction interface. However, runs C8-C16 show that the replacement reaction appears to stall after 24 hrs with 77% transformation. It seems likely that the porosity may decay during the reactions. The reasons that the product bornite does not exhibit highly porous structure could be related to

the relatively high mobility of Cu by solid state diffusion at 200 to 300 °C. In this temperature interval bornite undergoes two phase transitions: high to intermediate at 265 °C and from intermediate to low below 200 °C. These transformations are associated with Cu and Fe ordering, consistent with high metal mobility. The outer surface of bornite is in contact with the bulk solution and bornite is added to the grain as overgrowth as the bulk solution composition becomes saturated with respect to bornite, due to the excess Fe released at the ICDR interface. The concentration Fe in the bulk solution is low compared to that of the interface solution, so one might expect in the initial stages of the reaction that the rate of the ICDR reaction to be much faster than the rate of bornite overgrowth. The overgrowth layer of bornite is not as prominent in this system as the chalcopyrite overgrowth in the replacement of hematite by chalcopyrite (Zhao et al. 2013a), but nevertheless the bornite overgrowth does cement grains together.

Since Zhao et al. (2013a) presented a detailed discussion on the chemical reaction process of hematite replaced by chalcopyrite or/and bornite, this discussion will not be repeated here. We will only consider the replacement of chalcopyrite by bornite in basic solution CB10. The overall reaction under all studied conditions can be written as:

$$CuFeS_2(s) + 2H_2S(aq) + 4CuCl_2^- = Cu_5FeS_4(s) + 4HCl(aq) \quad (1)$$

The replacement of chalcopyrite by bornite is a redox reaction, involving a reduction reaction of chalcopyrite dissolution and an oxidation of bornite precipitation. The factors that control ICDR reactions are complex and ultimately governed by the interplay between chalcopyrite dissolution and bornite precipitation, which depends on factors such as solution composition and mineral solubility.

The chalcopyrite dissolution reaction releases the speciation of Cu, Fe and HS^- at the reaction front and results in the immediate precipitation of bornite at the precipitation site. Chalcopyrite dissolves, resulting in the increase of the concentration of aqueous Fe complexes, Cu complexes and S at the reaction front. Once the concentration of Fe, Cu and S, at the reaction front reaches supersaturation with respect to bornite (or more correctly the *bdss*), then bornite can begin to nucleate at sites on the chalcopyrite surface. As explained in Zhao et al. (2013a), Fe(II) is the most stable form of Fe and Cu (I) is the most stable form of Cu under the solution conditions used in these experiments. Speciation calculations show that CuHS(aq) and $Cu(HS)_2^-$ are the predominant Cu complexes under reaction conditions and the main speciation of Fe includes $Fe(OH)_2$, $Fe(OH)_3^-$ and $Fe(OH)_4^-$, due to the high concentration of basic in the buffer solution. These Fe species are transported through the network of pores and microcracks to the bulk solution, enabling bornite overgrowth.

5.4.2 The composition of bornite and the exsolution of digenite and bornite

At 300 °C the bornite composition corresponds to a composition in *bdss* of $Bn_{90}Dg_{10}$ over the pH range 4.39 to 7.43, while at 250 °C the composition corresponds to $Bn_{50}Dg_{50}$, thus indicating that the compositions become more Cu-rich at lower reaction temperatures, although this relationship could not been explored in detail in this study. In reactions that were initiated at 300 °C for 24 hrs and then annealed at 150 °C for 24, 72 or 120 hrs (G1-G3) the product was bornite with exsolution lamella of digenite. The fact that the reaction was initiated at 300 °C indicates that the original bulk composition was $Bn_{90}Dg_{10}$ and that when the hydrothermal system was annealed at 150 °C the solid solution exsolved to give digenite lamella approximately 1 to 3 μm in width in a bornite matrix (Figs. 5.2d and 5.2e).

Note that these exolsution textures show no obvious evidence of porosity indicating that during the exsolution the system recrystallized. Grguric and Putnis (1999) undertook detailed experiments on the breakdown of the bornite-digentite solid solution by annealing under dry conditions. Some of the compositions they examined correspond exactly to the compositions found in the hydrothermal experiments reported above, and Grguric and Putnis (1999) produced exsolution textures similar to those found here. The image in Figure 5.2f is from Grguric and Putnis (1999) and shows the exsolution texture produced by annealing $Bn_{90}Dg_{10}$ at 180 °C for 11 weeks. The texture in Figure 5.2d and 5.2e was produced by annealing at 150 °C under hydrothermal conditions for 72 hrs. The difference in the rate of textural coarsening is a factor of 25 times faster between hydrothermal and dry conditions. In fact it is probably greater than 25 times due to the 30 °C temperature difference of the annealing stage, 150°C for the hydrothermal experiments and 180°C for the dry experiments. While in the Grguric and Putnis (1999) sample the exsolution and coarsening is driven by solid state diffusion, in this study these processes are catalyzed by hydrothermal recrystallization as the porosity in the system is annealed out to reduce surface area. This illustrates the importance of role of the hydrothermal fluids and the kinetics of recrystallization in the development of ore textures. Zhao et al. (2013b) showed that exsolution processes could be triggers by hydrothermal replacement reaction in gold silver tellurides.

5.5 Acknowledgement

We thank Len Green, Aoife McFadden, and Benjamin Wade from Adelaide Microscopy Center for their assistance in using the FESEM and electron microprobe. We thank Dr.

Benjamin A. Grguric for the image in Figure 5.4c. This work has been made possible by the financial support of the Australian Research Council (Grants DP0880884 and DP1095069).

5.6 References

Amcoff, Ö. (1988) Experimental replacement of chalcopyrite by bornite: Textural and chemical changes during a solid-state process. Mineralium Deposita, 23(4), 286-292.

Brugger, J., McFadden, A., Lenehan, C.E., Etschmann, B., Xia, F., Zhao, J., and Pring, A. (2010) A novel route for the synthesis of mesoporous and low-thermal stability materials by coupled dissolution-reprecipitation reactions: mimicking hydrothermal mineral formation. CHIMIA International Journal for Chemistry, 64, 693-698.

Bruker AXS (2009) TOPAS V4.2: General profile and structure analysis software for powder diffraction data. Bruker AXS GmbH, Karlsruhe, Germany

Cook, N.J., Ciobanu, C.L., Danyushevsky, L.V., and Gilbert, S. (2011) Minor and trace elements in bornite and associated Cu-(Fe)-sulfides: A LA-ICP-MS study. Geochimica Cosmochima Acta, 75(21), 6473-6496.

Grguric, B.A. and Putnis, A. (1999) Rapid exsolution behaviour in the bornite-digenite series, and implications for natural ore assemblages. Mineralogical Magazine, 63(1), 1-14.

Grguric, B.A., Harrison, R.J., and Putnis, A. (2000) A revised phase diagram for the bornite-digenite join from in situ neutron diffraction and DSC experiments. Mineralogical Magazine, 64(2), 213-231.

Halbach, P., Blum, N., Münch, U., Plüger, W., Garbe-Schönberg, D., and Zimmer, M. (1998) Formation and decay of a modern massive sulfide deposit in the Indian Ocean. Mineralium Deposita, 33(3), 302-309.

Morimoto, N. and Gyobu, A. (1971) The composition and stability of digenite. American Mineralogist, 56, 1889-1909.

Oszczepalski, S. (1999) Origin of the Kupferschiefer polymetallic mineralization in Poland. Mineralium Deposita, 34, 599-613.

Putnis, A. (2009) Mineral replacement reactions. Reviews in Mineralogy and Geochemistry, 70(1), 87-124.

Qian, G., Brugger, J., Skinner, W.M., Chen, G., and Pring, A. (2010) An experimental study of the mechanism of the replacement of magnetite by pyrite up to 300°C. Geochimica et Cosmochimica Acta, 74(19), 5610-5630.

Qian, G., Xia, F., Brugger, J., Skinner, W.M., Bei, J., Chen, G., and Pring, A. (2011) Replacement of pyrrhotite by pyrite and marcasite under hydrothermal conditions up to 220 °C: An experimental study of reaction textures and mechanisms. American Mineralogist, 96(11-12), 1878-1893.

Qian, G., Brugger, J., Testemale, D., Skinner, W., and Pring, A. (2013) Formation of As(II)-pyrite during experimental replacement of magnetite under hydrothermal conditions. Geochimica et Cosmochimica Acta, 100, 1-10.

Ramdohr, P. (1980) The ore minerals and their intergrowths (2nd edition). Pergamon Press, London.

Robb, L. (2005) Introduction to ore-forming processes. Blackwell Publishing, Oxford.

Roberts, W.M.B. (1963) The low temperature synthesis in aqueous solution of chalcopyrite and bornite. Economic Geology, 58(1), 52-61.

Shvarov, Y. and Bastrakov, E. (1999) HCH: a software package for geochemical modelling. User's guide. AGSO record, 1999/25, 60 pp.

Tenailleau, C., Pring, A., Etschmann, B., Brugger, J., Grguric, B., and Putnis, A. (2006) Transformation of pentlandite to violarite under mild hydrothermal conditions. American Mineralogist, 91(4), 706-709.

Xia, F., Brugger, J., Chen, G., Ngothai, Y., O'Neill, B., Putnis, A., and Pring, A. (2009) Mechanism and kinetics of pseudomorphic mineral replacement reactions: A case study of the replacement of pentlandite by violarite. Geochimica et Cosmochimica Acta, 73(7), 1945-1969.

Zhao, J., Brugger, J., Ngothai, Y., and Pring, A. (2013a) The formation of chalcopyrite and bornite under hydrothermal conditions: an experimental approach (Submitted to American Mineralogist).

Zhao, J., Brugger, J., Xia, F., Ngothai, Y., Chen, G., and Pring, A. (2013b) Dissolution-reprecipitation versus solid-state diffusion: mechanism of mineral transformations in sylvanite, $(AuAg)_2Te_4$, under hydrothermal conditions. *American Mineralogist*, 98, 19-32.

CHAPTER 6

CHAPTER 6 CONCLUSIONS

The major contribution of these researches is that they advance our knowledge and understanding of hydrothermal mineral formation processes in situations, where the kinetics of mineral replacement reactions are controlled by CDR reaction competing with solid state diffusion-driven reactions. These reactions lead to complex mineral textures, and assemblages. The results show that the kinetic of the solid state reactions is greatly accelerated by the presence of reaction generated porosity. Two systems were investigated in details: the replacement of sylvanite by Au-Ag alloy and the second is the formation and decomposition of the bornite-digentite solid solution (*bdss*). The second contribution is that this thesis provides an insight into sulfidation of hematite resulting in chalcopyrite as well as the replacement of chalcopyrite by bornite under hydrothermal conditions, which process via CDR mechanism with large positive volume change at relative high temperatures (up to 300°C). This chapter draws brief conclusions of each study, points out the contribution of each project, and highlights the possible investigations of future research.

6.1 Dissolution-reprecipitation vs. solid-state diffusion

The replacement of sylvanite by Au-Ag alloy and other gold silver tellurides under hydrothermal conditions presents a very complex reaction path due to the interplay between solution-driven interfaces coupled dissolution-reprecipitation (ICDR) reactions and solid-state diffusion driven processes. Initially, sylvanite was replaced by Au-Ag alloy via an ICDR mechanism, which could be characterized by the textural features of high porosity, micro-cracking, and sharp reaction fronts without a significant gap between the

parent and product phases, and the pseudomorphic morphological preservation of original sylvanite. Over the course of the ICDR process, the majority of Te is eventually lost to solution and the Au and Ag rapidly precipitate at the reaction fronts. Once the concentrations of Au, Ag and Te reach a critical state, sylvanite dissolution becomes coupled with the precipitation of calaverite-I (Ag-rich-Te-depleted calaverite) instead of Au-Ag alloy. However, calaverite-I is unstable and breaks down via the solid-state exsolution to calaverite-II (a normal calaverite phase) and phase X, which in turn decomposes to a petzite and hessite lamellae via a solid-state diffusion. Also of note is that the calaverite-I, calaverite-II and phase X would all replaced by Au-Ag alloy via ICDR reactions as the hydrothermal replacement reaction. The textures that resulted from ICDR reactions present high porosity (e.g. the porous rim of Au-Ag alloy and porous calaverite-I), while products from solid-state reaction are largely nonporous, such as the nonporous calaverite -II and petzite-hessite lamella which show no visible pores.

This is the first report on the complex interaction among solid-state diffusion and coupled dissolution-reprecipitation reactions under hydrothermal conditions. Due to the high solid-state mobility of Ag ion in the Au-Ag-Te system, the unstable intermediate phase of calaverite-I breaks down into calaverite-II and phase X, which itself is an unstable solid solution followed by the exsolution of phase X into petzite and hessite. The resulting texture of product phase is consistent with some unusual Au-Ag telluride assemblages in nature and this reaction path explains the origin of natural Au-Ag telluride assemblages. That solid-state diffusion processes driven by CDR reactions are good examples for exploring the textural complexity in other mineral systems with high metal ion mobility, such as Ag-S system and Cu-(Fe)-S system. The replacement of sylvanite by Au-Ag alloy

also provides a possible low-emission and lower energy alternative to ore roasting as a pre-treatment for telluride-rich gold ores (Spry et al. 2004; Zhao et al. 2009, 2010).

6.2 Experimental study of the formation of chalcopyrite and bornite via the sulfidation of hematite

By exploring the effects of temperature (200-300°C), iron source and sulfidation levels on the sample textures and the reaction kinetics, Chapter 4 demonstrates that chalcopyrite could be synthesized by the interaction of hematite and solutions containing Cu(I) (as a chloride complex) and hydrosulfide at pH near the pK_a of H_2S(aq). Due to the large positive volume increase, the sulfidation of hematite by chalcopyrite follows a coupled dissolution-reprecipitation mechanism progressing via both direct replacement and overgrowth. As the reaction proceeds, the precipitation of bornite was observed on the outer surface of chalcopyrite grains, while no bornite was obtained at the reaction front between with hematite. This suggests chalcopyrite forms earlier than bornite and the nucleation rate of chalcopyrite is faster than that of bornite or other Cu-sulfides. The nature of sulfides in the experiments is controlled by the relative nucleation of chalcopyrite and bornite under certain reaction conditions. Distinct from other solution mediated ICDR reactions (e.g. the transformation from pentlandite to violarite) (Xia et al. 2009), no distinct porosity structure was observed in the quenched product grains this is probably due, at least in part to the large volume increase during the reactions. Instead, an overgrowth of chalcopyrite at the out layer of grains was observed; this is similar to the phenomenon observed in the replacement of magnetite by pyrite (Qian et al. 2010), where the volume increase is 65%. By exploring the synthesis of chalcopyrite under hydrothermal conditions,

this work investigated the nature of CDR reaction with large volume increase at relative high temperatures and high pressures. This study improves our understanding of the physical chemistry of chalcopyrite formation in nature, and could be used to further explain the formation of copper iron sulfide related hydrothermal ore deposits. Since the overgrowth of chalcopyrite is related to the excess availability of Fe (most likely as a Fe (II) complex in this case) transported to the bulk solution to the outside of the grain through reaction generated porosity, this study also offers a microcrosscopic insight into the fluid-rock interaction process, which can release Fe in solution and contribution to the formation of Cu-Fe sulfides.

6.3 The replacement of chalcopyrite by bornite under hydrothermal conditions

This study demonstrates that chalcopyrite could be replaced by bornite at temperature up to 300°C under hydrothermal conditions. The replacement reaction follows the CDR mechanism, which is characterized by a sharp reaction front between chalcopyrite and bornite, with no visible gap at the reaction front. In this transformation, the product bornite is compact with some scattered pores. As the reaction appears to stall after 24 hr reaction, the reason that the resulting bornite does not exhibit highly porous structure could be related to relatively high mobility of Cu ion by solid-state diffusion at 200 to 300°C. Though the overgrowth of bornite at the outer layer of grains was observed in this reaction, the rate of overgrowth might be slower than the rate of CDR reaction due to the excess Fe released at the ICDR interface. The composition of product “bornite” (really composition is the bornite-digentite solid solutions, *bdss*) seems to become less copper rich as

temperature increasing. At 300 °C, the composition of copper-rich bornite corresponds to $Bn_{90}Dg_{10}$, while at 250°C the composition is closer to $Bn_{50}Dg_{50}$. However, it is important to note that these results are only based on a comparatively small number of samples and reaction runs.

The exsolution texture of a bornite-digenite solid solution phase was observed during a further heating process at 150 and 200°C under hydrothermal conditions, which is texturally very similar to the breakdown of the bornite-digentite solid solution by annealing $Bn_{90}Dg_{10}$ at 180 °C for 11 weeks under dry conditions by Grguric and Putnis (1999, 2000). The difference is that the rate of textural coarsening is a factor of 25 times faster between hydrothermal and dry conditions. Distinct from the exsolution and coarsening driven by solid state diffusion (Grguric and Putnis 1999), the exsolution and coarsening in this study is catalyzed by hydrothermal recrystallization as the porosity in the system is annealed out to reduce surface area. This illustrates the importance of role of the hydrothermal fluids in the development of ore textures.

6.4 Future Work

This Ph.D project focuses on the mechanisms of mineral replacement reactions in both the Au-Ag-Te and Cu-Fe-S systems. During that later stages of these studies, a number of very interesting questions related to aspects study could not be explored in this thesis. Thus, some relevant work is listed below as future investigations.

6.4.1 The role of silver in the gold silver tellurides replacement reactions

Au-Ag alloy and a range of intermediate phases were obtained in the replacement of sylvanite, including Ag-rich-Te depleted calaverite ($Au_{0.78}Ag_{0.22}Te_{1.74}$), normal calaverite

($Au_{0.93}Ag_{0.07}Te_2$), petzite (Ag_3AuTe_2), and hessite (Ag_2Te). The reaction path is very complex, driven by the competition between solid-state reactions and ICDR reaction in sylvanite. The fact of solid state reaction reflects to the formation of a metastable phase of Ag-rich-Te depleted calaverite. Sylvanite was firstly replaced by Au-Ag alloy, and then by Ag-rich-Te depleted calaverite once the concentrations of Te and Ag reach a critical state. What is the structure of the Ag-rich-Te depleted calaverite reaction intermediate is it really a calaverite structure or is that just a quench product? To explore this question, some *in situ* hydrothermal diffraction experiments can be undertaken by X-ray diffraction. What are the concentrations of Te and Ag at the critical state mentioned in Chapter 3? How much does Ag lost to the solution? Are those questions related to the compositions of starting gold silver tellurides?

6.4.2 The replacement of bornite by chalcopyrite

In nature, the majority of chalcopyrite and bornite intergrowths show textures consistent with mineral replacement reaction and it is believed to occur either by bornite replacing chalcopyrite or by chalcopyrite replacing bornite. Chapter 4 shows that the precipitation of bornite was obtained as an intermediate phase in the replacement of hematite by chalcopyrite. As the reaction proceeds, the percentage of bornite firstly increases and then decrease due to the stability of bornite under hydrothermal conditions. Based on the formation of copper iron sulfides under hydrothermal conditions carried out in this study, more fundamental understanding about physical chemistry properties of copper iron sulfides can be used to investigate the replacement of bornite by chalcopyrite. Since the replacement of bornite by chalcopyrite is very similar to bornite leaching, the results could be very important in the improvement of bornite mining and processing industry.

6.4.3 The effects of sulfur on the formation of minerals in Cu-Fe-S system

In the replacement of hematite by chalcopyrite, several different products, such as magnetite, pyrite, chalcopyrite and bornite were obtained under different conditions. To investigate the effect of S on the reaction products, a detailed study could be carried out using different amount of sulfur source to determine the specific effect of sulfur on the formation of minerals in Cu-Fe-S system.

6.4.4 The composition of bornite-digenite solid solution

Bornite-digenite intergrowths are abundant in many Cu deposits, such as Montana and Olympic Dam. Rather than fluid-mediated reaction, most of the bornite-digenite assemblages show the evidence of exsolution of intermediate compositions along the bornite-low digenite join. In Chapter 5, chalcopyrite was replaced by the digenite-bornite solid solution (*bdss*), and the solid solutions exsolved to give digenite lamella within shorter time (24 to 120 hrs) during the further annealing at 150 and 200°C under hydrothermal conditions. Compare to the exsolution of $Bn_{90}Dg_{10}$ which took 11 weeks at 180°C under dry conditions (Grguric and Putnis 1999), the kinetics of these hydrothermal catalyzed reactions are 25 times rapid than the rate of solid-state diffusion. As mentioned in Chapter 5, the composition of *bdss* becomes more Cu-rich as the decrease of reaction temperature from 300 to 250°C. Thus, the hydrothermal replacement of chalcopyrite could be used to synthesize *bdss* with different compositions along the bornite-low digenite join, and the exsolution of *bdss* could be carried out under hydrothermal conditions. To further reveal the real mechanism and kinetic of exsolution process under hydrothermal conditions, *in situ* hydrothermal study could be carried out by high resolution neutron powder diffraction or synchrotron technology in the future.

6.4.5 The replacement of hematite by magnetite

Most geologists believe that the transformation of iron oxides in nature always require either an oxidizing or reduction agent and occur under specific redox environments. However, the mechanism of the iron oxides transformation was also proposed as the addition or leaching of Fe^{2+} in hydrothermal fluids (Ohmoto 2003). The replacement of hematite by magnetite was observed in the low sulfur (0.05 m) runs under slightly acid to basic conditions ($pH_{300°C}$ 6.06-8.59) in Chapter 4, and hematite was totally replaced by magnetite at $pH_{300°C}$ 8.59 within 90 hrs. The reaction mechanism should be more complex than only a redox reaction controlled by S. It may be related to the dissolution of hematite into Fe^{2+} and the reaction between hematite and Fe^{2+} in fluid media. Another concerning is whether hematite would be replaced by iron sulfides, such as pyrite or pyrrhotite under some certain conditions. Therefore, the replacement of hematite by magnetite is worthy of further detailed investigations.

6.5 References

Grguric, B.A. and Putnis, A. (1999) Rapid exsolution behaviour in the bornite-digenite series, and implications for natural ore assemblages. Mineralogical Magazine, 63(1), 1-14.

Grguric, B.A., Harrison, R.J., and Putnis, A. (2000) A revised phase diagram for the bornite-digenite join from in situ neutron diffraction and DSC experiments. Mineralogical Magazine, 64(2), 213-231.

Ohmoto, H. (2003) Nonredox transformations of magnetite-hematite in hydrothermal systems. Economic Geology, 98(1), 157-161.

Qian, G., Brugger, J., Skinner, W.M., Chen, G., and Pring, A. (2010) An experimental study of the mechanism of the replacement of magnetite by pyrite up to 300 °C. Geochimica et Cosmochimica Acta, 74(19), 5610-5630.

Spry, P.G., Chryssoulis, S., and Ryan, C.G. (2004) Process mineralogy of gold: Gold from telluride-bearing ores. Journal of the Minerals, Metals and Materials Society, 56, 60-62.

Xia, F., Brugger, J., Chen, G., Ngothai, Y., O'Neill, B., Putnis, A., and Pring, A. (2009) Mechanism and kinetics of pseudomorphic mineral replacement reactions: A case study of the replacement of pentlandite by violarite. Geochimica et Cosmochimica Acta, 73(7), 1945-1969.

Zhao, J., Brugger, J., Grundler, P.V., Xia, F., Chen, G., and Pring, A. (2009) Mechanism and kinetics of a mineral transformation under hydrothermal conditions: Calaverite to metallic gold. American Mineralogist, 94, 1541-1555.

Zhao, J., Xia, F., Pring, A., Brugger, J., Grundler, P.V., and Chen, G. (2010) A novel pre-treatment of calaverite by hydrothermal mineral replacement reactions. Minerals Engineering, 23, 451-453.

APPENDIX A

Statement of Authorship

Title of Paper	**Mechanism of mineral transformations in krennerite, Au_3AgTe_8, under hydrothermal conditions.**
Publication Status	◉ Published, ○ Accepted for Publication, ○ Submitted for Publication, ○ Publication style
Publication Details	**Xu, W., Zhao, J., Brugger, J., Chen, G., and Pring, A. (2013) Mechanism of mineral transformations in krennerite, Au_3AgTe_8, under hydrothermal conditions. American Mineralogist, 98,2086-2095.**

Author Contributions

By signing the Statement of Authorship, each author certifies that their stated contribution to the publication is accurate and that permission is granted for the publication to be included in the candidate's thesis.

Name of Principal Author	**Weina Xu**		
Contribution to the Paper	**Designed and performed experiments, interpreted and processed data, wrote manuscript.**		
Signature		Date	**6 August 2013**

Name of Co-Author (Candidate)	**Jing Zhao**		
Contribution to the Paper	**Helped to evaluate and edit the manuscript.**		
Signature		Date	**6 August 2013**

Name of Co-Author	**Joël Brugger**		
Contribution to the Paper	**Helped to evaluate and edit the manuscript.**		
Signature		Date	**5 July 2013**

Name of Co-Author	**Guorong Chen**		
Contribution to the Paper	**Supervised development of work and helped in manuscript evaluation.**		
Signature		Date	**12 August 2013**

Name of Co-Author	**Allan Pring**		
Contribution to the Paper	**Supervised development of work, helped in data interpretation and manuscript evaluation, and acted as corresponding author.**		
Signature		Date	**8 August 2013**

Xu, W., Zhao, J., Brugger, J., Chen, G. & Pring, A. (2013) Mechanism of mineral transformations in krennerite, Au_3AgTe_8, under hydrothermal conditions.
American Minerologist, v. 98(11-12), pp. 2086-2095

APPENDIX B

Statement of Authorship

Title of Paper	**A novel pre-treatment of calaverite by hydrothermal mineral replacement reactions.**
Publication Status	◉ Published, ○ Accepted for Publication, ○ Submitted for Publication, ○ Publication style
Publication Details	**Zhao, J., Xia, F., Pring, A., Brugger, J., Grundler, P.V., and Chen, G. (2010) A novel pre-treatment of calaverite by hydrothermal mineral replacement reactions. Minerals Engineering, 23(5), 451-453.**

Author Contributions

By signing the Statement of Authorship, each author certifies that their stated contribution to the publication is accurate and that permission is granted for the publication to be included in the candidate's thesis.

Name of Principal Author (Candidate)	**Jing Zhao**		
Contribution to the Paper	**Designed and performed experiments, interpreted and processed data, wrote manuscript.**		
Signature		Date	**6 August 2013**

Name of Co-Author	**Fang Xia**		
Contribution to the Paper	**Helped to evaluate and edit the manuscript.**		
Signature		Date	**6 August 2013**

Name of Co-Author	**Allan Pring**		
Contribution to the Paper	**Supervised development of work, helped in data interpretation and manuscript evaluation.**		
Signature		Date	**8 August 2013**

Name of Co-Author	**Joël Brugger**		
Contribution to the Paper	**Supervised development of work, helped in data interpretation and manuscript evaluation.**		
Signature		Date	**5 July 2013**

Name of Co-Author	**Pascal V. Grundler**		
Contribution to the Paper	**Helped in manuscript evaluation**		
Signature		Date	**13 August2013**

Name of Co-Author	**Guorong Chen**		
Contribution to the Paper	**Supervised development of work, helped in data interpretation and manuscript evaluation, and acted as corresponding author.**		
Signature		Date	**12 August 2013**

Zhao, J., Xia, F., Pring, A., Brugger, J., Grundler, P.V. & Chen, G. (2010) A novel pre-treatment of calaverite by hydrothermal mineral replacement reactions.
Minerals Engineering, v. 23(5), pp. 451-453

APPENDIX C

Statement of Authorship

Title of Paper	**Syntheses and crystallization of mineralogically relevant chalcogenide glasses.**
Publication Status	◉ Published, ○ Accepted for Publication, ○ Submitted for Publication, ○ Publication style
Publication Details	**Tao, H., Pring, A., Xia, F., Brugger, J., Zhao, J., Wang, S., and Chen, G. (2010) Syntheses and crystallization of mineralogically relevant chalcogenide glasses. Journal of the American Ceramic Society, 93(9), 2434-2437.**

Author Contributions

By signing the Statement of Authorship, each author certifies that their stated contribution to the publication is accurate and that permission is granted for the publication to be included in the candidate's thesis.

Name of Principal Author	**Hui Tao**		
Contribution to the Paper	**Designed and performed experiments, interpreted and processed data, wrote manuscript.**		
Signature		Date	**12 August 2013**

Name of Co-Author	**Allan Pring**		
Contribution to the Paper	**Supervised development of work, helped in data interpretation and manuscript evaluation.**		
Signature		Date	**8 August 2013**

Name of Co-Author	**Fang Xia**		
Contribution to the Paper	**Supervised development of work, helped in data interpretation and manuscript evaluation.**		
Signature		Date	**6 August 2013**

Name of Co-Author	**Joël Brugger**		
Contribution to the Paper	**Supervised development of work, helped in data interpretation and manuscript evaluation.**		
Signature		Date	**5 July 2013**

Name of Co-Author (Candidate)	**Jing Zhao**		
Contribution to the Paper	**Helped to evaluate and edit the manuscript.**		
Signature		Date	**6 August 2013**

Name of Co-Author	**Shufen Wang**		
Contribution to the Paper	**Helped in manuscript evaluation**		
Signature		Date	**13 August 2013**

Name of Co-Author	**Guorong Chen**		
Contribution to the Paper	**Supervised development of work, helped in data interpretation and manuscript evaluation, and acted as corresponding author.**		
Signature		Date	**12 August 2013**

Tao, H., pring, A., Xia, F., Brugger, J., Zhao, J., Wang, S. & Chen, G. (2010) Sytheses and crystallization of mineralogically relevant chalcogenide glasses.
Journal of the American Ceramic Society, v. 93(9), pp. 2434-2437

APPENDIX D

Statement of Authorship

Title of Paper	**Single-pass flow-through reaction cell for high-temperature and high-pressure in situ neutron diffraction studies of hydrothermal crystallization processes.**
Publication Status	◉ Published, ○ Accep ted for Publication, ○ Submitted fo r Publication, ○ Publication style
Publication Details	**Xia, F., Brugger, J., Qian, G., Ngothai, Y., O'Neill, B., Zhao, J., Pullen, S., Olsene, S., and Pring, A. (2012) Single-pass flow-through reaction cell for high-temperature and high-pressure in situ neutron diffraction studies of hydrothermal crystallization processes. Journal of Applied Crystallography, 45, 166-173.**

Author Contributions

By signing the Statement of Authorship, each author certifies th at their stated contribution to the publication is accurate and that permission is granted for the publication to be included in the candidate's thesis.

Name of Principal Author	**Fang Xia**		
Contribution to the Paper	**Designed and performed experiments, interpreted and processed data, wrote manuscript.**		
Signature		Date	**6 August 2013**

Name of Co-Author	**Joël Brugger**		
Contribution to the Paper	**Supervised development of work, helped in data interpretation and manuscript evaluation.**		
Signature		Date	**5 July 2013**

Name of Co-Author	**Gujie Qian**		
Contribution to the Paper	**Performed experiments and helped to edit manuscript.**		
Signature		Date	**13 August 2013**

Name of Co-Author	**Yung Ngothai**		
Contribution to the Paper	**Helped in manuscript evaluation.**		
Signature		Date	**6 August 2013**

Name of Co-Author	**Brian O'Neill**		
Contribution to the Paper	**Helped in manuscript evaluation.**		
Signature		Date	**15 August 2013**

Name of Co-Author (Candidate)	**Jing Zhao**		
Contribution to the Paper	**Performed experiments and helped to evaluate manuscript.**		
Signature		Date	**6 August 2013**

Name of Co-Author	**Stewart Pullen**		
Contribution to the Paper	**Designed and evaluated the reaction cell.**		
Signature		Date	**15 August 2013**

Name of Co-Author	**Scott Olsen**		
Contribution to the Paper	**Designed and evaluated the reaction cell.**		
Signature		Date	**15 August 2013**

Name of Co-Author	**Allan Pring**		
Contribution to the Paper	**Supervised development of work, helped in data interpretation and manuscript evaluation, and acted as corresponding author.**		
Signature		Date	**8 August 2013**

research papers

Journal of
Applied Crystallography
ISSN 0021-8898

Received 26 September 2011
Accepted 18 January 2012

Single-pass flow-through reaction cell for high-temperature and high-pressure *in situ* neutron diffraction studies of hydrothermal crystallization processes

Fang Xia,[a,b] Joël Brugger,[a,b] Gujie Qian,[b,c] Yung Ngothai,[d] Brian O'Neill,[d] Jing Zhao,[b,d] Stewart Pullen,[e] Scott Olsen[e] and Allan Pring[a,b]*

[a]School of Earth and Environmental Sciences, University of Adelaide, North Terrace, Adelaide, South Australia, 5005, Australia, [b]Department of Mineralogy, South Australian Museum, North Terrace, Adelaide, South Australia, 5000, Australia, [c]Ian Wark Research Institute, University of South Australia, Mawson Lakes Campus, Mawson Lakes, South Australia, 5095, Australia, [d]School of Chemical Engineering, University of Adelaide, North Terrace, Adelaide, South Australia, 5005, Australia, and [e]The Bragg Institute, Australian Nuclear Science and Technology Organisation, Locked Bag 2001, Kirrawee DC, New South Wales, 2232, Australia. Correspondence e-mail: allan.pring@samuseum.sa.gov.au

A large-volume single-pass flow-through cell for *in situ* neutron diffraction investigation of hydrothermal crystallization processes is reported. The cell is much more versatile than previous designs owing to the ability to control independently and precisely temperature (up to 673 K), pressure (up to 46 MPa), flow rate (0.01–10 ml min^{-1}) and reaction-fluid volume ($\geq$65 ml). Such versatility is realized by an innovative design consisting of a room-temperature and ambient-pressure external fluid supply module, a high-pressure reaction module which includes a high-temperature sample compartment enclosed in a vacuum furnace, and a room-temperature and high-pressure backpressure regulation module for pressure control. The cell provides a new avenue for studying various parameters of hydrothermal crystallizations independently, *in situ* and in real time at extreme hydrothermal conditions (*e.g.* supercritical). The cell was successfully commissioned on the high-intensity powder diffractometer beamline, Wombat, at the Australian Nuclear Science and Technology Organisation by investigating the effect of pressure on the hydrothermal pseudomorphic conversion from $SrSO_4$ (celestine) to $SrCO_3$ (strontianite) at a constant temperature of 473 K and flow rate of 5 ml min^{-1}. The results show that the increase of pressure exerts a nonlinear effect on the conversion rate, which first increases with increasing pressure from 14 to 20 MPa, and then decreases when pressure further increases to 24 MPa.

1. Introduction

The mechanism and kinetics of hydrothermal crystallization processes are of great interest across a range of scientific disciples. For mineralogists and petrologists, a fundamental understanding of reaction mechanism and kinetics will lead to a clearer picture of the formation of minerals in crustal hydrothermal environments (Qian *et al.*, 2010); for hydrometallurgists, it will help optimize the physical and chemical reaction parameters for improved leaching and metal extraction (Ruiz *et al.*, 2011; Zhao *et al.*, 2010); and for materials chemists, it can be applied to guide the product-oriented design of conditions for the hydrothermal syntheses of novel technological materials, hence replacing the traditional time-consuming 'trial and error' practice (Francis & O'Hare, 1998; Davis & Lobo, 1992; Xia, Brugger, Ngothai *et al.*, 2009; Brugger, Mcfadden *et al.*, 2010). Unfortunately, the investigation of the crystallization mechanism and kinetics of hydrothermal processes remains challenging. The reasons for this are that, on one hand, hydrothermal reactions are complex processes involving a dynamic interplay between dissolution, formation of metastable intermediate phases, nucleation, crystal growth and mass transport (Brugger, Pring *et al.*, 2010), and on the other hand, *in situ* studies that are capable of providing valuable direct information about the reaction at elevated pressure and temperature have been rare owing to the limited availability of suitable scientific tools and experimental protocols.

In recent years, the scope for *in situ* direct observation of hydrothermal crystallizations has increased dramatically, thanks to the increasing availability of high-flux synchrotron

X-ray and neutron sources and the development of suitable hydrothermal cells (Evans *et al.*, 1995; Francis *et al.*, 1999; Walton & O'Hare, 2000; Ok *et al.*, 2010). Compared to X-ray diffraction, the neutron diffraction technique has the advantage that relatively large volumes of hydrothermal fluids and samples can be used (cm^3 *versus* mm^3 to μm^3), therefore enabling *in situ* investigations of crystallization under conditions close to those found in natural hydrothermal systems, and metallurgical leaching and materials syntheses on the laboratory and pilot scales. In addition, the weaker interaction of neutrons with the samples compared with X-rays limits the incidence of beam damage, which can strongly affect reaction kinetics and reaction products in synchrotron-based X-ray experiments (Mesu *et al.*, 2005). For these reasons, several hydrothermal cells have been developed for neutron diffraction, covering a wide range of temperature (up to 723 K), pressure (up to 35.5 MPa) and fluid volume (up to 320 ml), and have been applied in studies of mineral and novel materials crystallization (Walton *et al.*, 1999, 2000; Williams *et al.*, 2006; O'Neill *et al.*, 2006; Xia, Qian *et al.*, 2010; Xia, O'Neill *et al.*, 2010; Ok *et al.*, 2010). However, a hydrothermal reaction cell capable of operating over a wider range of hydrothermal conditions, combining features of independent and precise control of temperature, pressure, reaction-fluid volume and flow rate, has not been available. To remove these limitations, we have designed a single-pass flow-through cell, which has been commissioned at the high-intensity powder diffractometer (HIPD) beamline, Wombat, at the Australian Nuclear Science and Technology Organisation (ANSTO). The capability of the cell for *in situ* neutron diffraction of hydrothermal crystallization was demonstrated by a case study of the effect of pressure on the reaction kinetics of hydrothermal pseudomorphic conversion from $SrSO_4$ (celestine) to $SrCO_3$ (strontianite) at constant temperature and fluid flow rate.

2. Cell design

The design of the single-pass flow-through cell is illustrated in Fig. 1. The cell consists of three modules: a low-temperature (close to room temperature) and ambient-pressure external fluid supply module, a high-pressure reaction module which includes a high-temperature sample compartment enclosed in a vacuum furnace provided by ANSTO, and a room-temperature high-pressure backpressure regulation module. The external fluid supply and the high-pressure reaction modules are connected by a high-performance liquid chromatography (HPLC) pump and a backpressure regulator. In the following paragraphs, the principle of the cell operation will be explained, then the ANSTO vacuum furnace and three modules of the cell will be individually described, and finally the cell will be briefly compared with previous designs.

The cell design enables independent and accurate control of temperature, pressure and flow rate of the fluid. The reaction temperature is controlled by a vacuum furnace (item 8 in Fig. 1) provided by ANSTO. Apart from the sample compartment inside the vacuum furnace the rest of the cell is maintained at low temperatures (<323 K), as a result of efficient cooling achieved by the relatively long (3 m) travel path of the connecting tubing (item 4 in Fig. 1 or item 17 in Fig. 2), the relatively low fluid flow rate and the low thermal conductivity of 316-type stainless steel. The control of pressure is achieved by a combination of the HPLC pump (item 11

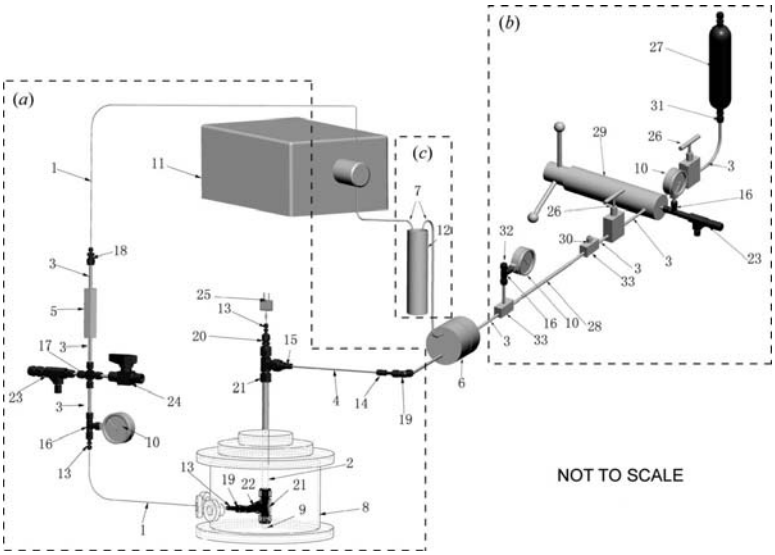

Figure 1
Schematic drawing of the single-pass flow-through cell. Three modules are shown in dashed borders: (*a*) the high-pressure reaction module; (*b*) the room-temperature high-pressure backpressure regulation module; and (*c*) the low-temperature (close to room temperature) and ambient-pressure external fluid supply module. (1) 1/16″ (1″ ≃ 2.54 cm) connecting tube (Swagelok); (2) 1/2″ sample compartment tube (Swagelok); (3) 1/4″ connecting tube (Swagelok); (4) 1/8″ connecting tube (Swagelok); (5) soft seat check valve (30-41HF4-T, HIP); (6) backpressure regulator (BP-100, Temco); (7) 1/4″ flexible silicone tubes; (8) vacuum furnace provided by ANSTO (vacuum pump and heater not shown); (9) custom made plug for centering; (10) pressure gauges (Swagelok, PGI-63B-LG25-LAOX, 0–25 MPa); (11) HPLC pump (Varian ProStar 210/218); (12) reaction solution bottle (500 ml); (13) reducer (Swagelok S-100-R-4); (14) reducer (Swagelok S-200-R-4); (15) reducer (Swagelok S-200-R-8); (16) 1/4″ union tee (Swagelok S-400-3); (17) 1/4″ union cross (Swagelok S-400-4); (18) reducing union (Swagelok S-400-6-1); (19) 1/4″ union elbow (Swagelok S-400-9); (20) reducer (Swagelok S-400-R-8); (21) 1/2″ union tee (Swagelok S-810-3); (22) reducing port connector (Swagelok S-811-PC-4); (23) pressure relief valve (Swagelok S-4R3A); (24) high-pressure ball valve (Swagelok S-83PS4); (25) K-type thermocouple; (26) needle valves (Nova Swiss 30-11H4F); (27) water reservoir (Swagelok 304 L-HDF4-300); (28) 10 m high-pressure flexible hose (Nova Swiss); (29) hand pump (Nova Swiss); (30) sealing plug (Nova Swiss PLG-20-4); (31) male connector (Swagelok S-400-1-4); (32) sealing plug (Swagelok S-400-P); (33) tees (Nova Swiss TEE-20-4M).

research papers

in Fig. 1) and the backpressure regulator (item 6 in Fig. 1). In operation, the reaction module is first filled with reaction fluid by priming the module using the HPLC pump; the HPLC pump delivers a constant flow rate, so the pressure within the reaction module is built up by increasing the pressure in the backpressure regulation module using a hydraulic hand pump (item 29 in Fig. 1); finally the pressure is increased to the target value, and is maintained steadily throughout the reaction both in the reaction and in the backpressure regulation modules. The fluid flow rate is controlled by the HPLC pump and can be precisely set in the range from 0.01 to 10 ml min^{-1}; higher rates are possible using different HPLC head assemblages, albeit at the cost of lowering the maximum working pressures.

The ANSTO vacuum furnace was designed to operate between room temperature and 723 K. The heating is applied *via* the use of three Heraeus shortwave IR lamps that deposit a combined 1.5 kW of IR power towards the sample compartment of the cell. The stray IR radiation is reflected back onto the sample using a parabolic mirror with the sample compartment at its focus. The IR lamps are controlled using a K-type thermocouple which provides feedback to a Eurotherm 3216 temperature controller. This in turn controls a Eurotherm TE10A thyristor which provides the appropriate duty cycling as applied by the controller. The vacuum furnace body is constructed using 6061-T6 aluminium with a thinned down section (2 mm) as a neutron window. The vessel was constructed to AS1210 pressure-vessel requirements and will operate at a vacuum of 1×10^{-5} mbar (1 mPa). The design provides two spare ports for the ability to flow fluid through the system and install additional sensors without affecting the integrity of the furnace. The maximum allowable temperature of the external furnace body is 373 K and this is maintained by heat sinking to the sample stage of Wombat. This customizable furnace had a lid produced especially for the purpose of the experiment and to cater for the various experimental setups that were required.

In the external fluid supply module, the reaction fluid is stored in a reservoir (item 12 in Fig. 1). The fluid is pumped from the reservoir by the HPLC pump through a flexible silicone hose and injected into the high-pressure reaction module *via* two check valves in the HPLC pump head (pressure rated to 60 MPa). After traveling through the reaction module, the fluid passes from the outlet of the backpressure regulator and returns to the same fluid reservoir (closed-loop mode) or to a second fluid reservoir (open mode) *via* another flexible silicone hose.

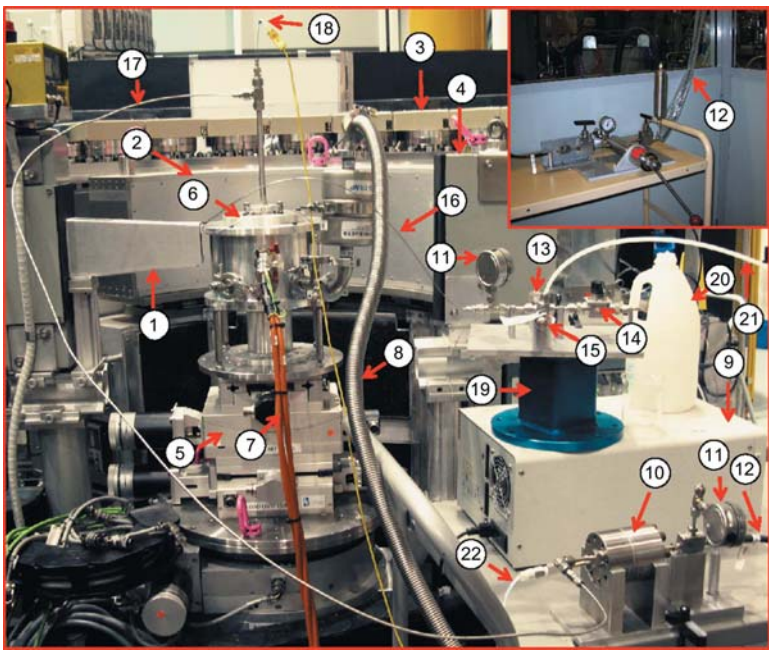

Figure 2
Setup of the hydrothermal cell on Wombat, the high-intensity powder diffractometer at ANSTO. (1) Neutron beam guide; (2) collimator; (3) detector; (4) beam stop; (5) four-dimensional adjustable stage; (6) ANSTO vacuum furnace; (7) power cable for the furnace; (8) vacuum tube; (9) HPLC pump; (10) backpressure regulator; (11) pressure gauges; (12) high-pressure flexible hose; (13) soft seat check valve; (14) ball valve for drainage; (15) pressure relief valve; (16) inlet tube of sample compartment; (17) outlet tube for sample compartment; (18) thermocouple; (19) positioning stage; (20) water reservoir for HPLC pump head cleaning; (21) drainage plastic tube for pressure relief; (22) outlet silicone tube of the backpressure regulator. The inset shows the hand pump for pressure generation and adjustment placed outside the instrument enclosure for remote control.

The reaction module has an internal volume of 65 ml and is composed of a series of Swagelok and HIP tubing and fittings. The reaction fluid is injected from the external fluid supply reservoir into this module by the HPLC pump. The fluid first travels through a soft seat check valve (item 5 in Fig. 1) to ensure the forward direction of the fluid flow, and then through the stainless steel sample compartment (item 2 in Fig. 1) sitting inside the ANSTO vacuum furnace, and finally flows through the backpressure regulator back to the external fluid supply module. Other components in this module include a cylinder-shaped sample tube made of 316-type stainless steel mesh (Locker Group, aperture diameter 47 µm) that is positioned in the center of the sample compartment, a pressure relief valve (item 23 in Fig. 1) to protect the system from pressure overshoot, a ball valve (item 24 in Fig. 1) for fluid drainage after the completion of the reaction, a pressure gauge (item 10 in Fig. 1) for monitoring system pressure, and a K-type thermocouple (item 25 in Fig. 1) with its measuring tip attaching to the mesh container for temperature recording at the sample position and also for sample loading (mesh sample container insertion) and extraction before and after the reaction. These

components are connected by Swagelok fittings (tubing, tee, reducer, elbow and cross) as illustrated in Fig. 1.

The backpressure regulation module consists of a Temco backpressure regulator (BP-100) connected to a hydraulic hand pump (item 29 in Fig. 1) *via* a 10 m high-pressure flexible hose. The temperature and pressure ratings for BP-100 are 394 K and 69 MPa, respectively. The water for the hydraulic pump is stored in a 300 ml reservoir (item 27 in Fig. 1). During pressurization of the backpressure regulation module, the pressure is monitored by two pressure gauges, one near the hand pump and the other near the backpressure regulator. A pressure relief valve (item 23 in Fig. 1) is installed near the hydraulic pump. Two valves are also fitted for initial water filling to the hand pump chamber and the high-pressure flexible hose from the water reservoir. The backpressure regulator operates based on a balanced-pressure principle. Once the process pressure at the outlet of the reaction module exceeds the dome pressure generated by the hydraulic hand pump, the Teflon diaphragm in the regulator flexes to allow the fluid to flow through, thus maintaining the process pressure. Once the process pressure drops below the dome pressure, the diaphragm will seal off the process and maintain the pressure.

In comparison with existing hydrothermal cells for *in situ* neutron diffraction, the current cell has several distinct features and advantages. (i) Unlike the previous cells in which pressures are temperature-dependent vapor-saturated values (Xia, Qian *et al.*, 2010; Xia, O'Neill *et al.*, 2010; O'Neill *et al.*, 2006; Ok *et al.*, 2010; Walton *et al.*, 1999), the temperature and pressure can be controlled independently in the new cell. This feature enables the study of the sole effect of temperature or pressure on the reaction kinetics of hydrothermal reactions *in situ*, which were not possible using previous cells. The independent effects of pressure or temperature are very important because for many hydrothermal reactions, such as those occurring deep in the Earth's crust, the reaction pressures are not vapor-saturated values. (ii) The current cell has higher temperature and pressure ratings. The temperature rating for the system is 673 K (determined by the ANSTO furnace). The pressure rating is determined by the mechanically weakest component in the system, the sample compartment. At room temperature, the wall-thickness-dependent pressure ratings of the sample compartment are 18, 35 and 46 MPa, for wall thicknesses of 0.89, 1.65 and 2.11 mm, respectively. These pressure ratings decrease with increasing temperature owing to the temperature-dependent tensile strength of stainless steel, by a factor of 0.96 at 473 K, 0.85 at 588 K and 0.80 at 673 K. Combined with independent control of pressure and temperature, these ratings enable the study of crystallization in aqueous systems under supercritical conditions *in situ* for a wide range of solvent properties (*e.g.* water density 0.11–0.56 g cm^{-3} at 673 K). (iii) The cell has the ability to rapidly heat the sample compartment to the target temperature. In our experiments, increasing the temperature from 293 to 473 K took only 4 min with a temperature overshoot of less than 3 K. Such rapid temperature increase minimizes the reaction extent below the target temperature, allowing for the collection of isothermal reaction kinetic data from very close to the beginnings of the hydrothermal reactions. The large improvement in heating rates is due to the fact that only a small portion (~10 ml of fluid in the sample compartment) of the total reaction fluid ($\geq$ 65 ml) needs to be heated. Once the fluid travels out of the sample compartment, it cools quickly to close to room temperature. In the previous cells, the entire fluid in the fluid reservoir (~150 ml) needs to be heated up, which takes approximately 20 min before isothermal reaction data can be collected (Xia, Qian *et al.*, 2010; Xia, O'Neill *et al.*, 2010; O'Neill *et al.*, 2006). (iv) Because the external fluid supply module is operated at ambient temperature and pressure, the chemistry of the fluid can be easily controlled (*e.g.* controlled atmosphere) and the fluid volume can be extremely flexible. The fluid volume can be as small as the internal volume of the reaction module (~65 ml) or as large as one wishes, allowing the setting of a wide range of solid to fluid ratios for hydrothermal crystallizations. (v) The separation of the fluid supply module from the reaction module allows the operation of the cell in either closed-loop mode or open mode, while previous cells can only operate in closed-loop mode. Open-loop operation mode enables continuous monitoring of solution parameters (*e.g.* Eh, pH, composition) both prior to and after the reaction, and opens the way for *in situ* study of mineral dissolution and crystallization under steady-state conditions, which is an important approach for getting theoretically meaningful rate constants (Nagy & Lasaga, 1992; Lasaga, 1998). (vi) The flow rate is independently controlled and can be finely tuned within the range 0.01–10 ml min^{-1}, while in previous cells the flow rate either is a fixed nonadjustable value owing to the use of a mechanical pump (O'Neill *et al.*, 2006) or is dependent on reaction temperature owing to the thermosyphon or convection principle of the fluid circulation (Xia, Qian *et al.*, 2010; Xia, O'Neill *et al.*, 2010). The precisely adjustable flow rate enables the investigation of the effects of flow rate on the reaction kinetics, more closely mimicking the conditions of particular hydrothermal crystallizations, such as mineral alterations deep in the Earth's crust.

3. Instrumental setup

The cell was commissioned on Australia's new HIPD beamline, Wombat, at ANSTO. The setup of the cell on Wombat is shown in Fig. 2. A neutron beam with a wavelength of 1.54 Å was selected using a vertically focusing germanium (115) monochromator at a takeoff angle of 90° (Studer *et al.*, 2006). The beam size was shaped by a slit system and in this study the size was 10 mm (width) × 40 mm (height) so as to completely immerse the central part of the sample compartment in the beam. After impinging on the sample, the neutrons first traveled through an oscillating radial collimator. The collimator eliminates unwanted background Bragg scattering, for example from the aluminium body of the vacuum furnace. Then the diffracted neutrons were detected by a 200 mm-high position-sensitive area detector spanning from 15 to 135° in 2θ. The distance from the sample to the front of the radial collimator was 430 mm, providing ample space for the ANSTO vacuum furnace. The 2θ position and the neutron wavelength

were calibrated using an alumina (Al_2O_3) standard. The intensities of the diffraction patterns were calibrated against the diffraction pattern of an empty vanadium can which is assumed to have uniform intensity in the two-dimensional detector.

4. Experimental test

The hydrothermal replacement reaction from $SrSO_4$ (the mineral celestine, orthorhombic, *Pnma*) to $SrCO_3$ (the mineral strontianite, orthorhombic, *Pmcn*) was studied on Wombat using the current cell. The purposes of the experiments were twofold: firstly to demonstrate the capability of the cell and secondly to make a preliminary investigation into the effect of pressure on the rate of a hydrothermal mineral replacement reaction. Celestine ($SrSO_4$), a common mineral mostly found in sedimentary rocks, is the main natural resource of strontium (Hanor, 2004). Celestine is commercially used to produce strontium carbonate ($SrCO_3$), from which other strontium chemicals for various applications are obtained (Castillejos *et al.*, 1996). The conversion from $SrSO_4$ to $SrCO_3$ is currently achieved by either the black ash process or the direct conversion process (Carrillo *et al.*, 1995). The black ash process involves high-temperature (>1223 K) reduction, hot-water leaching and finally precipitation; therefore it is a complex and energy-intensive process. The direct conversion process is simpler and consumes less energy, as the process converts $SrSO_4$ directly to $SrCO_3$ in a carbonate solution under hydrothermal conditions.

The conversion rate is dependent on various parameters, and the optimization of these parameters is vital for efficient processing. While the effects of temperature, particle size and solution chemistry (CO_3^{2-}/SO_4^{2-} ratio) on the conversion kinetics have been reported (Castillejos *et al.*, 1996; Suarez-Orduna *et al.*, 2004), the effect of pressure has yet to be investigated. Since pressure leaching is becoming an efficient and economic process in hydrometallurgy of some metals (Rubisov *et al.*, 2000; Provis *et al.*, 2003), it is interesting to see how an increase in pressure affects the rate of the conversion from $SrSO_4$ to $SrCO_3$. The ability to control temperature and pressure independently using the new cell is ideal for this purpose, because the temperature can be maintained constantly at different pressures, and neutron diffraction makes it practicable to monitor the conversion progress *in situ*. Additionally, the high neutron flux of the OPAL reactor at ANSTO allows the collection of high-quality data with adequate counting statistics in a relatively short time. This study involved fluid phases, which slightly increased the background, and hence we collected diffraction patterns every 15 min to balance the time resolution and adequate signal-to-noise ratio.

In the hydrothermal conversion from $SrSO_4$ to $SrCO_3$, natural millimetre-sized celestine crystals with a pale-blue color from the Sakoang deposit, Mitsijo district, Mahajang province, Madagascar (South Australian Museum Registration Number G21074), were used as starting materials. They were hand selected, ultrasonically cleaned, crushed and sieved. Grain sizes between 150 and 400 μm were used in this study. Analytical grade $NaCO_3$ (≥99.0%, Sigma–Aldrich) was used to prepare the $NaCO_3$ solution. Heavy water (D_2O, provided by ANSTO) instead of ordinary water (H_2O) was used as the solvent for solution preparation aiming to avoid high background from incoherent scattering of hydrogen atoms. In each experimental run, the molar ratio between anions CO_3^{2-} in the freshly prepared solution and SO_4^{2-} in the $SrSO_4$ sample was set to 4, so that the overall reaction can be kept far from equilibrium during the course of the conversion. Specifically, 2 g of $SrSO_4$ grains were reacted with 200 ml of 0.218 *M* Na_2CO_3 solution in all three experiments, which were conducted in closed-loop mode at constant temperature (473 K) and flow rate (5 ml min^{-1}) but with varying pressures, namely 14, 20 and 24 MPa.

The reaction progress was followed by recording *in situ* neutron diffraction patterns. The reaction extent y was calculated by the general formula

$$y = (Y_0 - Y_t)/(Y_0 - Y_e) \times 100\%, \quad (1)$$

where Y_t, Y_0 and Y_e are the mass fractions of the reactant crystals at an arbitrary reaction time t, initially ($t = 0$) and at equilibrium ($t = \infty$, in this case $Y_e = 0$), respectively. The mass fractions of involved phases were obtained from the Rietveld (1969) phase quantification method based on the diffraction data. The Rietveld least-square fittings were performed with the aid of the computer program *GSAS* (Larson & Von Dreele, 2004; Toby, 2001); structure models for least-squares fittings were obtained from the Inorganic Crystal Structure Database (Nos. 92608 for $SrSO_4$, 166088 for $SrCO_3$), and were originally sourced from Jacobsen *et al.* (1998) and Antao & Hassan (2009), respectively.

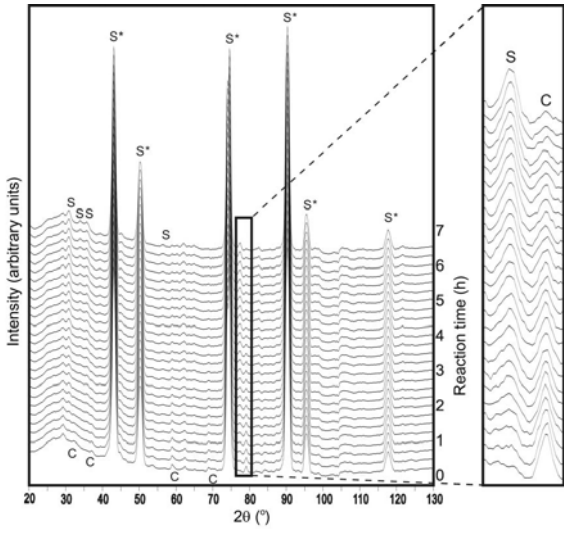

Figure 3
Neutron diffraction (λ = 1.54 Å) patterns of the conversion from $SrSO_4$ to $SrCO_3$ at 473 K and 14 MPa. C = $SrSO_4$, S = $SrCO_3$, S* = stainless steel.

The kinetics were then modeled by the Avrami equation (Xia *et al.*, 2007; Zhao *et al.*, 2009):

$$\ln\ln[1/(1-y)] = n\ln k + n\ln t. \quad (2)$$

From equation (2), the rate constants k and the time exponent n were extracted by plotting $\ln\ln[1/(1-y)]$ *versus* $\ln t$.

The *in situ* diffraction patterns for the conversion at 473 K and different pressures are similar in appearance, consisting of three observable phases (stainless steel, $SrSO_4$ and $SrCO_3$) and one nonlinear background arising from broad D_2O peaks mainly in the range below 50°. As an example, the diffraction patterns for the conversion at 14 MPa are shown in Fig. 3. The stainless steel peaks from the sample compartment tube and mesh basket are intense but remain constant throughout the reaction. In the 2θ range out of the stainless peak positions, *e.g.* the enlarged region in Fig. 3, it is clearly seen that the $SrCO_3$ diffraction peaks increase with time at the expense of those from $SrSO_4$. No other phase was observed as reaction

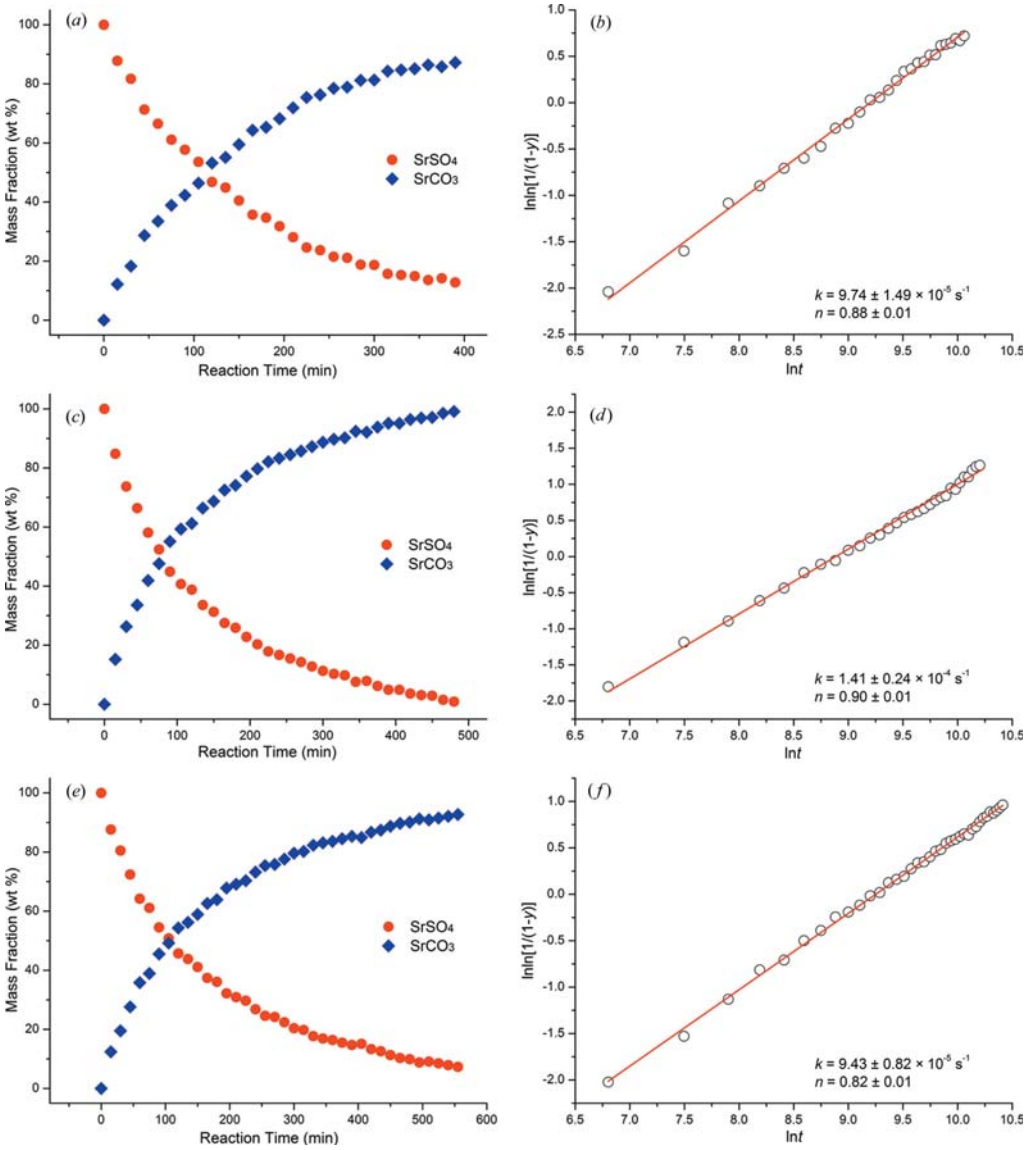

Figure 4
Plots of mass fractions as a function of reaction time and their corresponding Avrami plots for the calculation of rate constants k and time components n (value shown in the plots) during the conversion from $SrSO_4$ to $SrCO_3$ at 473 K and (*a*), (*b*) 14 MPa, (*c*), (*d*) 20 MPa and (*e*), (*f*) 24 MPa.

intermediate or by-product. These patterns undoubtedly indicate the progressive conversion from $SrSO_4$ directly to $SrCO_3$ without a crystalline intermediary phase.

The progress of the conversion is quantitatively seen in the plots of mass fraction evolution with reaction time (Figs. 4*a*, 4*c* and 4*e*), which reveal that, at 14 MPa, 87 wt% $SrSO_4$ was converted to $SrCO_3$ after 6.5 h, and at 20 and 24 MPa, a similar conversion extent required 4.75 and 7 h, respectively. The corresponding Avrami plots (Figs. 4*b*, 4*d* and 4*f*) give rate constants k and time exponents n; they are $k = 9.74\ (149) \times 10^{-5}\ s^{-1}$ and $n = 0.88\ (1)$ for the reaction at 14 MPa, $k = 1.41\ (24) \times 10^{-4}\ s^{-1}$ and $n = 0.90\ (1)$ for the reaction at 20 MPa, and $k = 9.43\ (82) \times 10^{-5}\ s^{-1}$ and $n = 0.82\ (1)$ for the reaction at 24 MPa. The time exponent n is an indication of reaction mechanism (Christian, 1965); hence the similar value of n for the three reactions means that the same reaction mechanism prevails in the conversion under different pressures (Christian, 1965). Previous studies have shown that the conversion is a topotaxially coupled dissolution–reprecipitation reaction mechanism (Suarez-Orduna *et al.*, 2004). Similar to the other mineral replacement reactions (Xia *et al.*, 2008; Janssen *et al.*, 2010; Putnis, 2009, 2002; Tenailleau *et al.*, 2006), the mechanism of the replacement from $SrSO_4$ to $SrCO_3$ is explained as follows. In contact with the carbonate solution, $SrSO_4$ dissolves from the surface, resulting in a local solution supersaturated with respect to $SrCO_3$ and causing the $SrCO_3$ to nucleate and grow on the surface of $SrSO_4$ (at or near $SrSO_4$ dissolution sites); the precipitation of $SrCO_3$ in turn brings the local solution back to the undersaturated state with respect to $SrSO_4$ and drives its further dissolution. In such a manner, the two half reactions finally become coupled such that the rate of $SrSO_4$ dissolution and $SrCO_3$ precipitation equalize, and this coupling is retained until the pseudomorphic conversion is complete; hence the product $SrCO_3$ retains the external dimension of the initial $SrSO_4$ as macroscopically observed. The mechanism can be illustrated by the following reaction equations: the dissolution of $SrSO_4$,

$$SrSO_4 \rightarrow Sr^{2+} + {SO_4}^{2-}, \tag{3}$$

coupled with local precipitation of $SrCO_3$ onto the grain boundary (the interface between $SrSO_4$ and $SrCO_3$),

$$Sr^{2+} + {CO_3}^{2-} \rightarrow SrCO_3. \tag{4}$$

The overall conversion can be written as

$$SrSO_4 + {CO_3}^{2-} \rightarrow SrCO_3 + {SO_4}^{2-}. \tag{5}$$

Because the temperature was kept at 473 K, the flow rate was set at 5 ml min^{-1} and the conversion mechanism is the same for the studied pressure range, it is meaningful to discuss the effect of pressure on the conversion rate, and it is the first time the effect of pressure on a couple dissolution reprecipitation reaction has been investigated. The kinetic data suggest that the reaction rate increases with increasing pressure from 14 to 20 MPa, and then decreases when the pressure further increases from 20 to 24 MPa. Therefore, an optimized pressure must exist in the range from 14 to 24 MPa for the rapid conversion from $SrSO_4$ to $SrCO_3$.

This nonlinear relationship between the conversion rate and the pressure further illustrates the complexity of interface-coupled dissolution–reprecipitation replacement reactions, as has been discussed in a recent work (Qian *et al.*, 2011). These reactions often occur in a non-intuitive manner, *e.g.* nonlinear dependence of reaction rate on temperature (Xia, Brugger, Chen *et al.*, 2009), formation of thermodynamically unexpected mineral phases (Xia, Brugger, Chen *et al.*, 2009; Qian *et al.*, 2011), unpreserved crystallographic orientation in spite of structural similarity between parent and daughter minerals (Qian *et al.*, 2011), the dependence of reaction kinetics on sample texture (Xia *et al.*, 2007), and so on.

Further work is clearly required to investigate the nonlinear effect of pressure on the conversion rate from $SrSO_4$ to $SrCO_3$. In particular, the reproducibility of the experimental results needs be tested, and the pressure dependence measured over a wide range and at higher pressure resolution. However, we note that a significant effect of pressure on interface-coupled dissolution–reprecipitation reactions is not unexpected. On one hand, elevated pressure can usually accelerate the rate of mineral dissolution, which is termed 'pressure solution', a common phenomenon occurring deep in the Earth's crust and one that has been believed to be the main mechanism responsible for rock deformation (Rutter, 1983; Baker *et al.*, 1980; Tada & Siever, 1986). Therefore, it is not surprising that the increase of pressure from 14 to 20 MPa increases the dissolution rate of $SrSO_4$ and hence the overall conversion rate. On the other hand, the conversion process is not a simple dissolution process, as it also involves a coupled precipitation process. The increase of pressure may further exert a kinetic factor on precipitation. The topotaxial conversion from $SrSO_4$ to $SrCO_3$ involves a contraction of 3.258 and 0.838 Å along the a and c axes and an expansion of 3.062 Å along the b axis of the orthorhombic unit cell (Suarez-Orduna *et al.*, 2004). The overall ~15.5% volume contraction is compensated by the formation of elongated pores randomly distributed parallel to the b axis (Suarez-Orduna *et al.*, 2004), which is in agreement with the contraction of the a and c axes. The important feature here is the induced stress along the b axis due to its expansion. Although the stress can be relieved by expanding excessive volume into the surrounding pores, the intentionally increased external pressure exerts further stress by pushing the newly formed $SrCO_3$ onto the $SrSO_4/SrCO_3$ grain boundary along the b axis. This squeezing effect would lead to limited space for $SrCO_3$ precipitation and therefore retard the overall conversion rate. Such twofold effects of pressure on dissolution and precipitation are competitive and may have a transition at around 20 MPa – below 20 MPa the pressure effect on the dissolution is more important, while above 20 MPa the pressure effect on precipitation dominates the overall conversion kinetics.

5. Conclusion

In summary, we have designed and constructed a versatile large-volume flow-through cell for *in situ* neutron diffraction studies of high-temperature and high-pressure hydrothermal

crystallizations, and have commissioned it on the HIPD beamline at ANSTO by investigating the effect of pressure on the hydrothermal pseudomorphic conversion from $SrSO_4$ to $SrCO_3$. The cell introduced several advantages compared with the previous cells in that temperature, pressure and flow rate can be independently controlled, providing a new avenue for studying hydrothermal crystallizations *in situ*, and possibly in real time. This kind of investigation will definitely deepen our understanding of the mechanisms and kinetics of hydrothermal crystallization processes by providing a clearer picture of these complex processes. One limitation of the cell is the intense stainless steel peaks arising from the sample compartment tubing and mesh container, which may be overcome by replacing them with a non-scattering Ti/Zr alloy (Sidhu *et al.*, 1956; Gray & Bailey, 2008); this modification will be tested in future experiments.

This work is financially supported by the Australian Research Council (grant No. DP1095069) and the Australian Institute of Nuclear Science and Engineering (AINSE). We thank Mr Jason Peak (Chemical Engineering Workshop at the University of Adelaide) for the construction of the cell and Dr Andrew Studer (HIPD beamline scientist) for assistance with instrumental setup.

References

Antao, S. M. & Hassan, I. (2009). *Can. Mineral.* **47**, 1245–1255.
Baker, P. A., Kastner, M., Byerlee, J. D. & Lockner, D. A. (1980). *Mar. Geol.* **38**, 185–203.
Brugger, J., Mcfadden, A., Lenehan, C. E., Etschmann, B., Xia, F., Zhao, J. & Pring, A. (2010). *Chimia*, **64**, 693–698.
Brugger, J., Pring, A., Reith, F., Ryan, C., Etschmann, B., Liu, W., O'Neill, B. & Ngothai, Y. (2010). *Radiat. Phys. Chem.* **79**, 151–161.
Carrillo, F. R., Uribe, P. & Castillejos, A. H. (1995). *Miner. Eng.* **8**, 495–509.
Castillejos, A. H., delaCruz, F. P. & Uribe, A. (1996). *Hydrometallurgy*, **40**, 207–222.
Christian, J. W. (1965). *The Theory of Transformations in Metals and Alloys.* Oxford: Pergamon Press.
Davis, M. E. & Lobo, R. F. (1992). *Chem. Mater.* **4**, 756–768.
Evans, J. S. O., Francis, R. J., O'Hare, D., Price, S. J., Clark, S. M., Flaherty, J., Gordon, J., Nield, A. & Tang, C. C. (1995). *Rev. Sci. Instrum.* **66**, 2442–2445.
Francis, R. J., O'Brien, S., Fogg, A. M., Halasyamani, P. S., O'Hare, D., Loiseau, T. & Ferey, G. (1999). *J. Am. Chem. Soc.* **121**, 1002–1015.
Francis, R. J. & O'Hare, D. (1998). *J. Chem. Soc. Dalton Trans.* **19**, 3133–3148.
Gray, E. M. & Bailey, I. F. (2008). *J. Neutron Res.* **16**, 127–132.
Hanor, J. S. (2004). *J. Sediment. Res.* **74**, 168–175.
Jacobsen, S. D., Smyth, J. R., Swope, R. J. & Downs, R. T. (1998). *Can. Mineral.* **36**, 1053–1060.
Janssen, A., Putnis, A., Geisler, T. & Putnis, C. V. (2010). *Mineral. Mag.* **74**, 633–644.
Larson, A. C. & Von Dreele, R. B. (2004). Report LAUR 86-748. Los Alamos National Laboratory, New Mexico, USA.
Lasaga, A. C. (1998). *Kinetic Theory in the Earth Sciences.* Princeton University Press.
Mesu, J. G., van der Eerden, A. M., de Groot, F. M. & Weckhuysen, B. M. (2005). *J. Phys. Chem. B*, **109**, 4042–4047.
Nagy, K. L. & Lasaga, A. C. (1992). *Geochim. Cosmochim. Acta*, **56**, 3093–3111.
Ok, K. M., O'Hare, D., Smith, R. I., Chowdhury, M. & Fikremariam, H. (2010). *Rev. Sci. Instrum.* **81**, 125107.
O'Neill, B., Tenailleau, C., Ngothai, Y., Studer, A., Brugger, J. & Pring, A. (2006). *Physica B*, **385–386**, 942–945.
Provis, J. L., van Deventer, J. S. J., Rademan, J. A. M. & Lorenzen, L. (2003). *Hydrometallurgy*, **70**, 83–99.
Putnis, A. (2002). *Mineral. Mag.* **66**, 689–708.
Putnis, A. (2009). *Rev. Mineral. Geochem.* **70**, 87–124.
Qian, G., Brugger, J., Skinner, W. M., Chen, G. R. & Pring, A. (2010). *Geochim. Cosmochim. Acta*, **74**, 5610–5630.
Qian, G., Xia, F., Brugger, J., Skinner, W. M., Bei, J., Chen, G. & Pring, A. (2011). *Am. Mineral.* **96**, 1878–1893.
Rietveld, H. M. (1969). *J. Appl. Cryst.* **2**, 65–71.
Rubisov, D. H., Krowinkel, J. M. & Papangelakis, V. G. (2000). *Hydrometallurgy*, **58**, 1–11.
Ruiz, M. C., Vera, M. V. & Padilla, R. (2011). *Hydrometallurgy*, **105**, 290–295.
Rutter, E. H. (1983). *J. Geol. Soc.* (*London*), **140**, 725–740.
Sidhu, S. S., Heaton, L. R., Zauberis, D. D. & Campos, F. P. (1956). *J. Appl. Phys.* **27**, 1040–1042.
Studer, A. J., Hagen, M. E. & Noakes, T. J. (2006). *Physica B*, **385–386**, 1013–1015.
Suarez-Orduna, R., Rendon-Angeles, J. C., Lopez-Cuevas, J. & Yanagisawa, K. (2004). *J. Phys. Condens. Matter*, **16**, S1331–S1344.
Tada, R. & Siever, R. (1986). *Geochim. Cosmochim. Acta*, **50**, 29–36.
Tenailleau, C., Pring, A., Etschmann, B., Brugger, J., Grguric, B. A. & Putnis, A. (2006). *Am. Mineral.* **91**, 706–709.
Toby, B. H. (2001). *J. Appl. Cryst.* **34**, 210–213.
Walton, R. I., Francis, R. J., Halasyamani, P. S., O'Hare, D., Smith, R. I., Done, R. & Humphreys, R. J. (1999). *Rev. Sci. Instrum.* **70**, 3391–3396.
Walton, R. I. & O'Hare, D. (2000). *Chem. Commun.* pp. 2283–2291.
Walton, R. I., Smith, R. I., Millange, F., Clark, I. J., Sinclair, D. C. & O'Hare, D. (2000). *Chem. Commun.* pp. 1267–1268.
Williams, G. R., Norquist, A. J. & O'Hare, D. (2006). *Chem. Mater.* **18**, 3801–3807.
Xia, F., Brugger, J., Chen, G. R., Ngothai, Y., O'Neill, B., Putnis, A. & Pring, A. (2009). *Geochim. Cosmochim. Acta*, **73**, 1945–1969.
Xia, F., Brugger, J., Ngothai, Y., O'Neill, B., Chen, G. & Pring, A. (2009). *Cryst. Growth Des.* **9**, 4902–4906.
Xia, F., O'Neill, B., Ngothai, Y., Peak, J., Tenailleau, C., Etschmann, B., Qian, G., Brugger, J., Studer, A., Olsen, S. & Pring, A. (2010). *J. Appl. Cryst.* **43**, 511–519.
Xia, F., Qian, G., Brugger, J., Studer, A., Olsen, S. & Pring, A. (2010). *Rev. Sci. Instrum.* **81**, 105107.
Xia, F., Zhou, J. W., Brugger, J., Ngothai, Y., O'Neill, B., Chen, G. R. & Pring, A. (2008). *Chem. Mater.* **20**, 2809–2817.
Xia, F., Zhou, J., Pring, A., Ngothai, Y., O'Neill, B., Brugger, J., Chen, G. & Colby, C. (2007). *React. Kinet. Catal. Lett.* **92**, 257–266.
Zhao, J., Brugger, J., Grundler, P. V., Xia, F., Chen, G. & Pring, A. (2009). *Am. Mineral.* **94**, 1541–1555.
Zhao, J., Xia, F., Pring, A., Brugger, J., Grundler, P. V. & Chen, G. (2010). *Miner. Eng.* **23**, 451–453.

APPENDIX E

Statement of Authorship

Title of Paper	**A novel route for the synthesis of mesoporous and low-thermal stability materials by coupled dissolution-reprecipitation reactions: mimicking hydrothermal mineral formation.**
Publication Status	◉ Published, ○ Accep ted for Publication, ○ Submitted fo r Publication, ○ Publication style
Publication Details	**Brugger, J., McFadden, A., Lenehan, C.E., Etschmann, B., Xia, F., Zhao, J., and Pring, A. (2010) A novel route for the synthesis of mesoporous and low-thermal stability materials by coupled dissolution-reprecipitation reactions: mimicking hydrothermal mineral formation. CHIMIA International Journal for Chemistry, 64, 693-698.**

Author Contributions

By signing the Statement of Authorship, each author certifies th at their stated contribution to the publication is accurate and that permission is granted for the publication to be included in the candidate's thesis.

Name of Principal Author	**Joël Brugger**		
Contribution to the Paper	**Wrote manuscript and acted as corresponding author.**		
Signature		Date	**5 July 2013**

Name of Co-Author	**Aoife McFadden**		
Contribution to the Paper	**Performed experiments and helped to evaluate the manuscript**		
Signature		Date	**15 August 2013**

Name of Co-Author	**Claire E. Lenehan**		
Contribution to the Paper	**Helped in manuscript evaluation**		
Signature		Date	**27 August 2013**

Name of Co-Author	Barbara Etschmann		
Contribution to the Paper	Helped to evaluate the manuscript.		
Signature		Date	16 August 2013

Name of Co-Author	Fang Xia		
Contribution to the Paper	Helped to evaluate and edit the manuscript.		
Signature		Date	6 August 2013

Name of Co-Author (Candidate)	Jing Zhao		
Contribution to the Paper	Helped to evaluate and edit the manuscript.		
Signature		Date	6 August 2013

Name of Co-Author	Allan Pring		
Contribution to the Paper	Helped to evaluate and edit the manuscript.		
Signature		Date	8 August 2013

doi:10.2533/chimia.2010.1 Chimia 64 (2010) 1–6

A Novel Route for the Synthesis of Mesoporous and Low-Thermal Stability Materials by Coupled Dissolution-Reprecipitation Reactions: Mimicking Hydrothermal Mineral Formation

Joël Brugger*[ab], Aoife McFadden[ac], Claire E. Lenehan[c], Barbara Etschmann[ab], Fang Xia[ab], Jing Zhao[ad], and Allan Pring[abc]

Abstract: Replacement reactions ('pseudomorphism') commonly occur in Nature under a large range of conditions (T 25 to >600 °C; P 1 to >5 kbar). Whilst mineral replacement reactions are often assumed to proceed by solid-state diffusion of the metal ions through the mineral, many actually proceed *via* a coupled dissolution and reprecipitation (CDR) mechanism. In such cases, a starting mineral is dissolved into a fluid and this dissolution is coupled with the precipitation of a replacement phase across the reaction front. In cases where there are close relationships between the crystal structures of the parent and newly formed minerals, the replacement can be topotactic (interface-coupled dissolution and reprecipitation). The kinetics and chemistry of the CDR route are fundamentally different from solid-state diffusion and can be exploited i) for the synthesis of materials that are often difficult to synthesise *via* traditional methods and ii) to obtain materials with unique properties. This review highlights recent research into the use of CDR for such synthetic challenges. Emphasis has been given to i) the use of CDR to synthesise compounds with relatively low thermal stability such as the thiospinel mineral, violarite ($(Ni,Fe)_3S_4$), ii) preliminary work into use of CDR for the production of roquesite ($CuInS_2$), a potentially important photovoltaic component and, iii) examples where the textures resulting from CDR reactions are controlled by the nature and texture of the parent phase and the reaction conditions; these being the formation of micro-porous gold and three-dimensional ordered arrays of nanozeolite of uniform size and crystallographic orientation.

Keywords: Copper-indium sulphide · Coupled dissolution reprecipitation reaction · Materials synthesis · Mineral replacement · Nanozeolites · Porous gold · Thiospinels

Introduction

Aqueous fluids are ubiquitous in the Earth's crust and are the most important medium for mineral formation in surface and near-surface environments. Therefore understanding the dissolution, transport, and deposition of metals in aqueous hydrothermal fluids is central to understanding mineral genesis in geology. Minerals, and in particular, ores, form over a wide range of hydrothermal conditions: pressures from ambient to >5 kbar, temperatures from ambient to >600 °C, and complex solvent compositions (*e.g.* salinity up to >50 wt% salt; varying amounts of volatiles such as CO_2, CH_4 or H_2S) and provide the World's supply of metals such as Au, Ag, U, Pb, Zn, Mo or Fe.[1] In most cases minerals are not deposited into open cavities, but deep underground where reactions proceed *via* replacement of pre-existing rock-forming minerals. In this process the existing set of minerals reacts with the hydrothermal fluid and a different assemblage of minerals forms. In these processes, the external dimension of the primary mineral is preserved by the mineral product in varying degrees of detail, a widespread phenomenon called pseudomorphism. At a fundamental level, understanding processes such as metasomatism, metamorphism, or ore formation requires understanding the interplay between the physical chemistry of mineral dissolution and crystallization, solution chemistry, and fluid transport along grain boundaries and through the porosity within minerals. Much research effort has recently been focused on the formation of minerals by replacement *via* a fluid phase, a mechanism known as coupled dissolution–reprecipitation reaction (CDR).[2,3] The nature of fluid-mediated replacement reactions was explored by Cardew and Davey[4] in polymorphic transformation where there is no change in chemistry. Such topotactic reactions have sometimes been called structure-inheriting solid-state reactions (SISSRs) under hydrothermal conditions,[5,6] but were recently shown to represent a special form of CDR reactions known as interface coupled dissolution–reprecipitation reactions (ICDR reactions).[7] In ICDR reactions, dissolution of the precursor mineral is coupled both in space and time with the precipitation of the product mineral, allowing the external dimension to be preserved.

Our recent research into the nature of CDR reactions has led us to believe that these reactions can be employed in some forms of materials synthesis where more

*Correspondence: Dr. J. Brugger[ab]
E-mail: joel.brugger@samuseum.sa.gov.au
[a]Department of Mineralogy
South Australian Museum
North Terrace, Adelaide
SA 5000, Australia
[b]TRaX, School of Earth and Environmental Sciences
University of Adelaide, Adelaide, SA 5005, Australia
[c]School of Chemical and Physical Sciences
Flinders University
GPO Box 2100 Adelaide, SA 5001, Australia
[d]School of Chemical Engineering
University of Adelaide, Adelaide, SA 5005, Australia

direct methods are difficult. A suitable precursor is prepared, then partially, or completely, replaced from the grain surface into the interior *via* a CDR reaction in a carefully designed hydrothermal fluid to yield the product. In many respects these CDR reactions are similar to a process known to metallurgists as dealloying, which is used to produce nanoporous metals.[8] Indeed, ICDR reactions can also lead to the synthesis of materials with remarkable textural properties. Here we review ICDR as a reaction mechanism, and emphasize how the unique properties of this reaction mechanism can be used in materials synthesis.

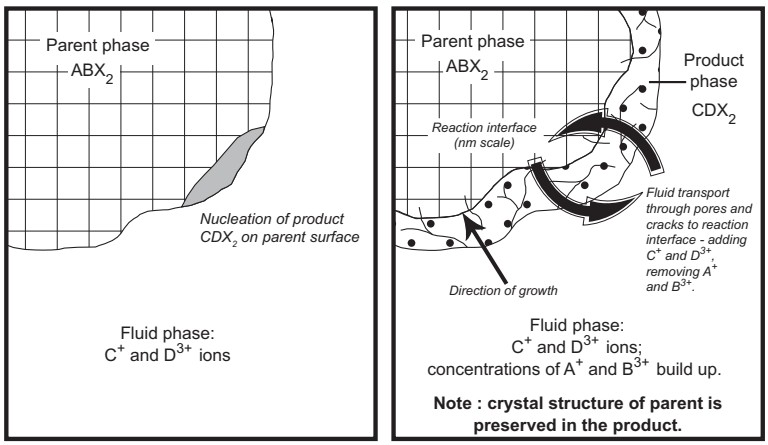

Fig. 1. Schematic diagram of an interface coupled dissolution–reprecipitation reaction.

The Mechanism of Interface Coupled Dissolution–Reprecipitation Reactions

While solid-state reactions are controlled by diffusion (P, T, stress state), CDR reactions proceed *via* the complete dissolution of the parent phase into a fluid, coupled (in space and time) with the precipitation of the product at the reaction front. Specific features of CDR reactions – especially in contrast with solid-state reactions – include i) the variable length scale of coupling, *i.e.* the distance between the dissolution front and the site of precipitation, ii) the controls exerted by solution chemistry and temperature on reaction kinetics and product composition, iii) the sharp phase boundary between the precursor and the product, and iv) the porous texture of the product.

The replacement length scale can vary from ~1 nm to up to 10's of μm or more.[9,10] The length scale of the coupling is controlled by the interplay between the kinetics of dissolution and precipitation, and these are in turn controlled by the relative solubilities of the parent and product phase, which depends on P, T, and solution composition (*e.g.* pH, redox, ligand concentrations[9]); and by the kinetics of nucleation and growth of the product. Local chemical gradients near the reaction front may also play a role in controlling dissolution and precipitation rates; in all cases, however, the product must be porous and remain porous for the duration of the reaction in order to enable fluid transport to and from the reaction front. In natural minerals it appears that over time the porosity heals, or is annealed out. In the case of a tightly coupled reaction (nanometer length scale), the rate of precipitation of the product must be at least as fast as the dissolution of the parent phase. Some CDR reactions proceed topotactically, preserving both the crystallographic orientation and the external morphology of the replaced grain (ICDR), while in others crystallographic relationships are not inherited. For crystallographic orientation to be preserved (Fig. 1), there must be a close structural relationship between the product and the parent phases, enabling the surface of the parent phase to serve as a patterning agent for the nucleation and growth of the product.[9]

Examples of Materials Synthesis *via* ICDR Reactions

Synthesis of Thiospinels

A class of metal sulphides, thiospinels (M_3S_4), analogues of oxide spinels, are attracting growing attention for their magnetic, semiconducting and superconducting properties as well as the metal-insulator transitions exhibited by some compositions.[11–13] Syntheses of thiospinels are thus important to facilitate full characterization of their properties and the development of their industrial applications.[14] Many metal sulphides can be readily synthesized by the traditional method of dry synthesis: heating the metal with elemental sulphur to high temperatures (>500 ºC) in an evacuated sealed glass tube. Others, however, are much more difficult to produce by this route because they have low thermal stabilities (<500 ºC), and thus must be prepared at temperatures below their decomposition points. One such compound is the thiospinel mineral violarite, $(Ni,Fe)_3S_4$, which breaks down at 373 ºC.[15] Slow reaction rates limit the application of the traditional route to the synthesis of $(Ni,Fe)_3S_4$, since several months annealing at or below 300 ºC are required. In addition, the product obtained *via* dry synthesis always contains significant quantities of impurity phases such as nickeliferous pyrite $(Fe,Ni)S_2$.[16,17] Exploring the potential of ICDR reactions to explain the common occurrence of violarite as an alteration product of pentlandite in nature, we were able to prepare pure samples of the thiospinels $(Ni,Fe)_3S_4$ (violarite) and Co_3S_4 (linnaeite) from $(Fe,Ni)_9S_8$ (pentlandite) and Co_9S_8 (cobaltpentlandite) precursors.[17,18] In this case pentlandite and violarite both have structures based on cubic closed packed arrays of S atoms, but differ by the distributions of metals over the available interstitial octahedral and tetrahedral sites (Fig. 2).

Using an ICDR reaction, pure $(Ni,Fe)_3S_4$ can be synthesized in less than three days, compared to the traditional dry synthesis route that requires three months annealing to obtain a product with only 72 ± 5 wt% purity. Xia *et al.*[9,18,19] found that the Fe/Ni ratio of $(Ni,Fe)_3S_4$ could be adjusted by varying the reaction conditions, including temperature (125–145 ºC), pH (1 to 6), and precursor stoichiometry. Between pH 1 and 6 the reaction proceeds *via* an ICDR reaction, with a very sharp reaction front and porous $(Ni,Fe)_3S_4$ product, as the dissolution of the pentlandite precursor is rate-limiting (Fig. 3). However, at low pH (<1) the precipitation of violarite becomes rate-limiting and the reaction is no longer interface coupled. The difference in mechanisms is illustrated in Fig. 4. It is also important to note that violarite is not the thermodynamically stable phase with respect to the bulk solution composition, yet was the only Fe-Ni sulphide forming under most experimental conditions; this reflects the fact that nucleation of violarite is favoured due to the close relationship with pentlandite. The role of the surface of the parent mineral in controlling the nature of the product during nucleation and growth has been recognized for example by Roy and Linnehan[20] (hydrothermal replacement of biogenic carbonates by phosphates), and is discussed in detail by Figlarz *et al.*[21] for both solid-state and hydrothermal situations.

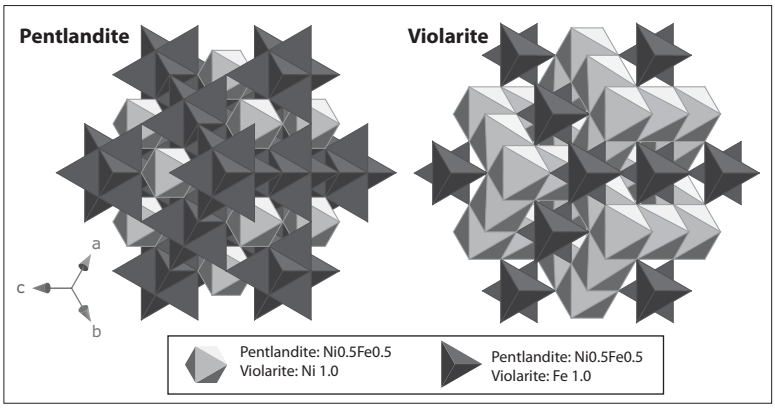

Fig. 2. Structural relationship between pentlandite and violarite, emphasizing the similarity in the close packed cubic arrays of S atoms in both minerals. Projection on the {111} plane. In pentlandite, the metal atoms occupy 1/2 of the tetrahedral sites and 1/8 of the octahedral sites in the ccp S array, while in violarite, they occupy 1/2 of the octahedral sites and 1/8 of tetrahedral sites.

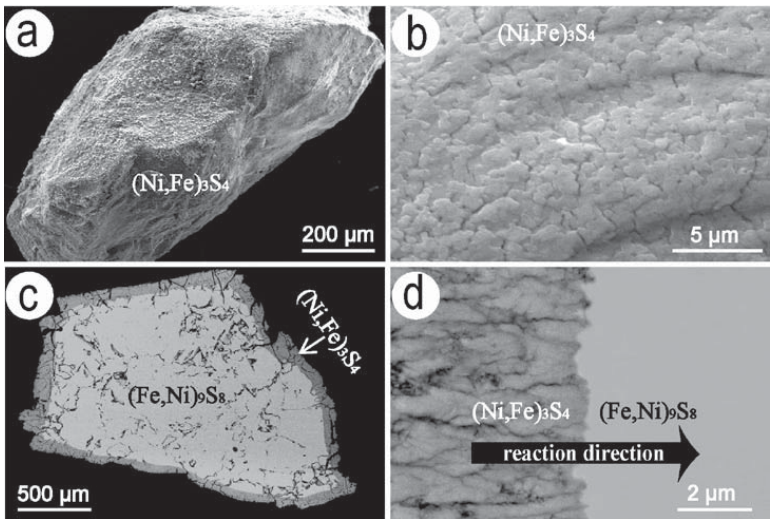

Fig. 3. SEM images of the pentlandite to violarite transformation. (a) SE image of a partially transformed pentlandite grain with a violarite outer layer. (b) SE image of porous violarite surface. (c) BSE image of cross section showing the advance of reaction from the grain surface to the interior and the preservation of external shape. (d) BSE image of the sharp reaction front and the direction of the transformation.

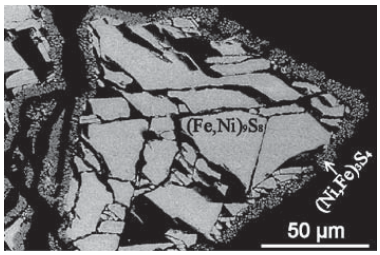

Fig. 4. SEM image of the replacement of pentlandite by violarite at low pH (pH = 1, T = 125 ˚C). Note that here the tight coupling between the dissolution and reprecipitation has broken down and the volarite only precipitates on the outside of the grain and not along the cracks or voids in the parent grain.

Synthesis of $CuInS_2$

$CuInS_2$ is a good semiconductor material with a direct band gap of approximately 1.5 eV within the peak frequencies of the solar spectrum and a high absorption coefficient of approximately 2.65 x 10^5 cm^{-1}.[22–24] Hence $CuInS_2$ is an ideal material for use in photovoltaic devices such as solar panels,[24] with the added advantage of posing only a minimal toxicological threat to the environment.[25] $CuInS_2$ occurs naturally as the rare mineral roquesite in high-temperature hydrothermal veins, usually in the form of inclusions in chalcopyrite ($CuFeS_2$), sphalerite (ZnS) or bornite (Cu_5FeS_4).[26]

Synthesis of $CuInS_2$ has been achieved *via* a number of methods, including solid-state reaction,[27] solvothermal synthesis,[28] static hydrothermal synthesis,[29] chemical vapour deposition[22,30,31] and spray pyrolysis.[32] The application of $CuInS_2$ in photovoltaic devices requires the production of pure, good quality thin films,[24] but the cost of synthesis remains a major drawback for widespread use.[31]

Minerals such as chalcopyrite ($CuFeS_2$), bornite (Cu_5FeS_4) and digenite (Cu_9S_5) are structurally related to $CuInS_2$, exhibit semiconducting properties,[15,33] and could be used as starting materials. Digenite for example has successfully been employed as a component in solar cells in the CdS/Cu_9S_5 and TiO_2/Cu_9S_5 systems.[34,35]

We undertook a preliminary experimental study to see if we could deposit $CuInS_2$ on the surface of either $CuFeS_2$ or Cu_9S_5 *via* ICDR under mild hydrothermal conditions. The synthesis was undertaken using an acetate buffered (pH 3.8), 2M NaCl solution prepared using deoxygenated water. Dissolved in the solution were $In(NO)_3$ (0.02M), $FeSO_4.7H_20$ (0.01 M) and CuCl (0.05 M), with either $CuFeS_2$ or Cu_9S_5 as the parent phase. $CuInS_2$ was successfully synthesised at 125 ˚C, 160 ˚C or 180 ˚C. These results indicate that Cu_9S_5 is a more pertinent starting material for the synthesis. Furthermore, the use of digenite (Cu_9S_5) eliminates the formation of the Fe_2O_3 by-product observed when using $CuFeS_2$ as the starting material. Both products possessed a sharp reaction front and were finely cracked (Fig. 5), features that are typical of a coupled dissolution–reprecipitation reaction. Consequently both the transformation from $CuFeS_2$ to Cu_9S_5 and the further transformation of Cu_9S_5 to $CuInS_2$ proceeded by a CDR mechanism. The production of $CuInS_2$ was highly sensitive to solution chemistry, with the transformation from Cu_9S_5 to $CuInS_2$ proceeding only at low concentrations of In^{3+}. Increasing In^{3+} concentrations above 0.02 M led to $In(OH)_3$ precipitation and inhibited the formation of $CuInS_2$.[36] Further experimental work on the system is required to tune the solution conditions in order to produce homogenous thin films of $CuInS_2$ on a Cu_9S_5 matrix before the suitability of this method can be fully assessed.

Engineering Microtextures by Interface Coupled Dissolution–Reprecipitation Reactions

Porous Gold from $AuTe_2$

Gold tellurides such as calaverite ($AuTe_2$) are important Au carriers in some ore deposits, but are difficult to recover using common leaching methods.[37] Zhao and coworkers.[38,39] found that Te could be effectively 'leached' from calaverite under hydrothermal conditions, leaving sponge-

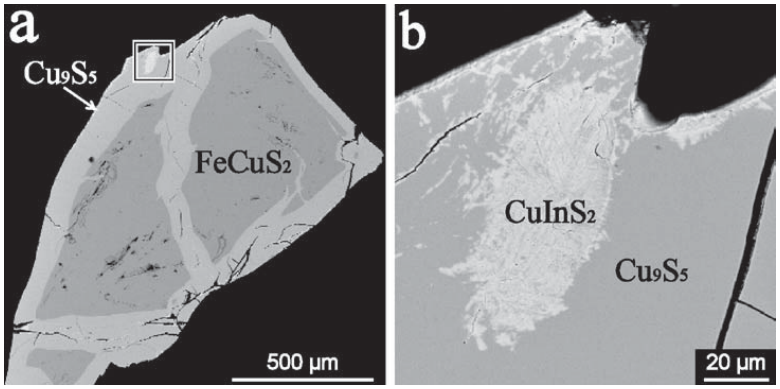

Fig. 5. SEM BSE Image of the $CuFeS_2$ transformation to Cu_9S_5 then further to $CuInS_2$ (T = 150°C, pH 3.8). (a) Grain of CuFeS2 partially transformed into Cu_9S_5, with a minor amount of $CuInS_2$ present at the rim. (b) Detail of the transformation of Cu_5S_9 into $CuInS_2$ at the rim of the grain shown in (a).

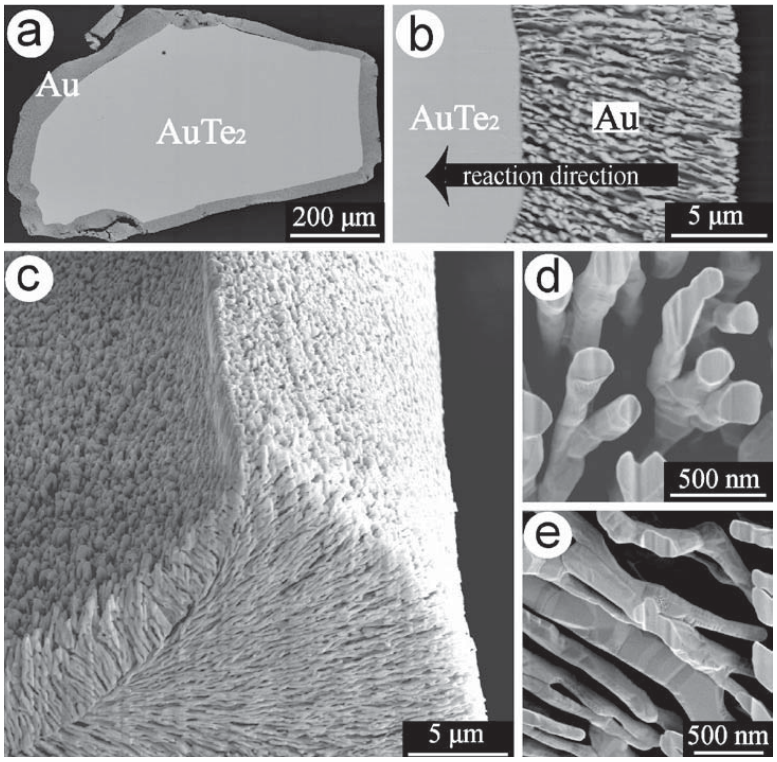

Fig. 6. SEM images of the transformation from calaverite to gold. (a,b) BSE images of partially transformed calaverite, showing the reaction direction, and the porous and filament-shaped gold aggregates growing from the sharp reaction interface. (c) SE images of a corner of a porous gold product. (d,e) Focused Ion Beam milled gold phase clearly show the size and shape of the gold filaments.

like porous gold (Fig. 6). The reaction proceeded over a wide range of solution conditions (pH 2–12), oxidant concentration and temperatures (140 to 220 °C). The replacement was pseudomorphic, with the porous gold preserving the external dimensions of the calaverite grains (Fig. 6a and 6b). The resulting elemental gold is porous, consisting of filament-shaped aggregates with diameters ranging from 200 to 500 nm and lengths up to 25 µm (Fig. 6d and 6e). Gold crystals are randomly oriented with respect to the twinned calaverite grains.

The pseudomorphic transformation proceeds *via* a coupled calaverite dissolution–gold precipitation mechanism, with calaverite dissolution being rate-limiting relative to gold precipitation. Tellurium is lost to the bulk solution as Te(IV) complexes, and may further precipitate away from the dissolution site (*e.g.* autoclave walls) as TeO_2(s). In contrast, gold precipitates locally near the calaverite dissolution site. Such local gold precipitation is facilitated by fast heterogeneous nucleation onto the calaverite surface. The dissolution of calaverite and the overall reaction are oxidation reactions, and oxygen diffusion through the porous metallic gold layer probably plays an important role in sustaining the reaction.

A similar dissolution–reprecipitation process may be responsible for the formation of 'mustard gold' during the weathering of gold-telluride ores. At 220 °C, solid-state replacement of calaverite by gold is slow (months), but calaverite grains ~100 µm in size are fully replaced in less than 24 hours under hydrothermal conditions, providing a possible alternative to roasting as a pre-treatment of telluride-rich gold ores.

Transformation of Leucite ($KAlSiO_4$) to Analcite ($NaAlSiO_4{\cdot}H_2O$)

Zeolites and zeolite-like materials display unique molecular sieve structures and are often considered 'green' materials.[40] Consequently, considerable research efforts are dedicated to the design of novel routes for the preparation of zeolites with hierarchical pore structures, adjustable size and morphology, uniform crystallographic orientation, and ordered arrangement,[41–43] as these features are essential for emerging applications as advanced catalysts, chemical sensors, highly selective membranes, optical materials, and low dielectric materials for microelectronics.[44,45]

Great success has been achieved on the control of hierarchical pore structure, size, and morphology of zeolite products[43,46,47] yet relatively less progress has been made on the alignment of the nano- or micro-zeolites into uniformly oriented and/or highly ordered arrays.[48] Xia *et al.*[49] reported the first synthesis of 3D ordered arrays of nanozeolites with uniform size and crystallographic orientation, and adjustable overall shape by a simple hydrothermal coupled dissolution–reprecipitation pseudomorphic replacement route (Fig. 7). The key to synthesize 3D ordered arrays of nanocrystals with uniform size and crystallographic orientation is to find a suitable precursor. Putnis *et al*.[50] showed using ^{18}O tracer that the leucite to analcime reaction proceeds *via* the ICDR mechanism. Leucite crystals contain inherent 3D ordered networks of nanometer-sized lamellar twins (Fig. 7c and 7e), and Xia *et al*.[49,51] demonstrat-

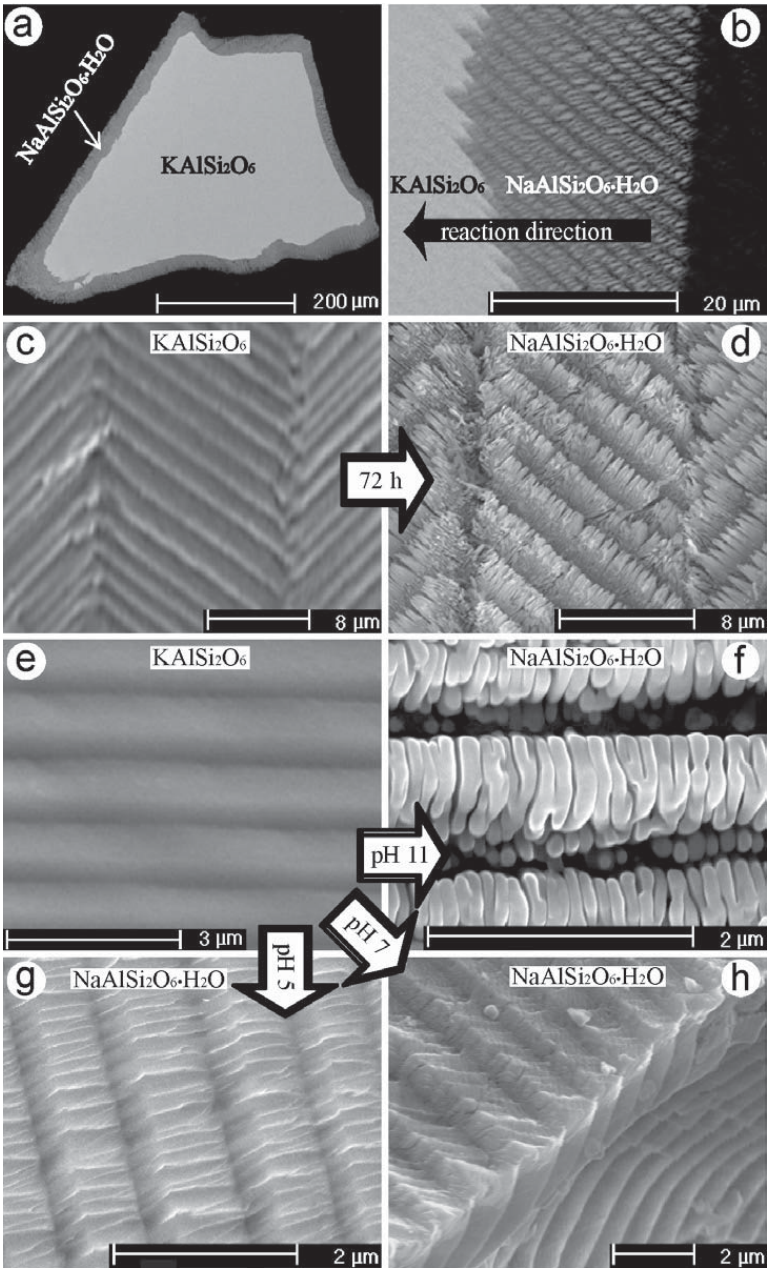

Fig. 7. SEM images of the transformation from $KAlSi_2O_6$ to $NaAlSi_2O_6{\cdot}H_2O$. (a,b) BSE images of partially transformed $KAlSi_2O_6$ showing the reaction direction, the preservation of the overall shape, the zigzag sharp reaction front, and the hierarchical porosity in the product phase. (c,d) SE images showing the 3D ordered arrays of $KAlSi_2O_6$ lamellae are preserved in the product, forming 3D ordered arrays of nano $NaAlSi_2O_6{\cdot}H_2O$ with uniform size and crystallographic orientation. (e,f) SE images of $NaAlSi_2O_6{\cdot}H_2O$ texture as a function of pH.

ed that such highly ordered 3D patterns could be precisely preserved during hydrothermal pseudomorphic replacement reactions in pH-buffered NaCl solutions, resulting in 3D ordered arrays of analcime nanocrystals (Fig. 7d and 7f). Moreover, these analcime nanocrystals have uniform size and crystallographic orientation due to epitaxial nucleation and growth facilitated by the similarity of crystal lattice between leucite and analcime. The morphology of the nanocrystals is tuneable by simply changing solution pH. Mild acidic to mild alkaline conditions tend to produce cuboid-shaped nanocrystals; while strong alkaline conditions favour the formation of cylindrical-shaped nanocrystals (Fig. 7f–h). The replacement follows the ICDR mechanism, with the dissolution of leucite being rate-limiting.

This pseudomorphic replacement route could be used to synthesize other ordered arrays of functional nanocrystals with controlled shape, size, and crystallographic orientation. Nature provides many possible precursors, but it is also possible to design and synthesize a suitable parent phase. Many minerals, such as microcline, cristobalite, nepheline, sodalite, leucite and other feldspathoid minerals, exhibit a microstructure consisting of 3D ordered network of twin planes, after a displacive or reconstructive phase transition upon cooling.[52,53] Many such precursors are also readily synthesized mimicking the natural formation environments.[54] Leucite ($KAlSi_2O_6$) was used as the precursor to synthesize analcime $NaAlSi_2O_6{\cdot}H_2O$ as an illustration of this new synthesis route,[49,51] because leucite crystals are abundant in Nature, and their 3D ordered lamellar twinning has been studied in detail.[55]

Conclusions

CDR reactions are often extremely complex, since they result from a complex dynamic interplay between dissolution and precipitation, controlled critically by phenomena such as surface nucleation, porosity creation/destruction, and transport of aqueous species to and from the reaction front. Understanding the molecular level mechanisms at work in these reactions is key in the textures and compositions of the products, and requires the concerted efforts of physical chemists and mineralogists, but may have many benefits in terms of synthesis of materials with unique chemical and textural properties. Acknowledgements

This work is funded by the Australian Research Council Project (DP0878903; DP0772299; DP1095069) and the South Australian Museum. Special thanks are due to the staff at Adelaide Microscopy for their help with scanning electron imaging. We are grateful to T. Armbruster for organising this special volume, and two anonymous reviewers for their helpful comments. This is TRaX publication #89.

Received: June 8, 2010

[1] J. Brugger, A. Pring, F. Reith, C. Ryan, B. Etschmann, W.H. Liu, B. O'Neill, Y. Ngothai, *Radiation Phys. Chem.* **2010**, *79*, 151.
[2] A. Putnis, *Miner. Mag.* **2002**, *66*, 689.
[3] A. Putnis, 'Mineral Replacement Reactions', in 'Thermodynamics and Kinetics of Water-

Rock Interaction', Reviews in Mineralogy & Geochemistry, **2009**, p. 87.
[4] P. T. Cardew, R. J. Davey, *Proc. Royal Soc.* **1985**, *A398*, 415.
[5] K. Eda, K. Chin, N. Sotani, M. S. Whittingham, *J. Solid State Chem.* **2005**, *178*, 158.
[6] K. Eda, Y. Uno, N. Nagai, N. Sotani, C. Chen, M. S. Whittingham, *J. Solid State Chem*. **2006**, *179*, 1453.
[7] A. Putnis, C. V. Putnis, *J. Solid State Chem*. **2007**, *180*, 1783.
[8] J. Erlebacher, M. J. Azia, A. Karma, N. Dimitrov, K. Sieradzki, *Nature* **2001**, *410*, 450.
[9] F. Xia, J. Brugger, G.R. Chen, Y. Ngothai, B. O'Neill, A. Putnis, A. Pring, *Geochim. Cosmochim. Acta* **2009**, *73*, 1945.
[10] B. Pewkliang, A. Pring, J. Brugger, *Can. Miner*. **2008**, *46*, 139.
[11] T. Hagino, Y. Seki, N. Wada, S. Tsuji, T. Shirane, K. Kumagai, S. Nagata, *Phys. Rev.* **1995**, *B51*, 12673.
[12] S. Nagata, N. Matsumoto, Y. Kato, T. Furubayashi, T. Matsumoto, J. P. Sanchez, P. Vulliet, *Phys. Rev.* **1998**, *B58*, 6844.
[13] M. S. Park, S. K. Kwon, B. I. Min, *Phys. Rev.* **2001**, *B64*, 100403.
[14] C. I. Pearce, R. A. D. Patrick, D. J. Vaughan, *Rev. Miner. Geochem.* **2006**, *61*, 127.
[15] D. J. Vaughan, J. R. Craig, 'Mineral chemistry of metal sulfides', Cambridge Univ. Press. UK, **1978**.
[16] C. Tenailleau, B. Etschmann, R. M. Ibberson, A. Pring, *Amer. Miner.* **2006**, *91*, 1442.
[17] C. Tenailleau, A. Pring, B. Etschmann, J. Brugger, B. Grguric, A. Putnis, *Amer. Miner*. **2006**, *91*, 706.
[18] F. Xia, J. Zhou, J. Brugger, Y. Ngthai, B. O'Neill, G. Chen, A. Pring, *Chem. Mater.* **2008**, *20*, 2809.
[19] F. Xia, A. Pring, Y. Ngothai, B. O'Neill, J. Brugger, G. Chen, C. Colby, *React. Kin. Catal. Lett.* **2007**, *92*, 257.
[20] D. M. Roy, S. K. Linnehan, *Nature* **1974**, *247*, 220.
[21] M. Figlarz, B. Gerand, A. Delahayevidal, B. Dumont, F. Harb, A. Coucou, F. Fievet, *Solid State Ionics* **1990**, *43*, 143.
[22] D. O. Henderson, R. Mu, A. Ueda, M. H. Wu, E. M. Gordon, Y. S. Tung, M. Huang, J. Keay, L. C. Feldman, J. A. Hollingsworth, W. E. Buhro, J. D. Harris, A. F. Hepp, R. P. Raffaelle, *Mater. Design* **2001**, *22*, 585.
[23] J. Guha, H.-Z. Lu, B. Dubé, F. Robert, M. Gagnon, *Econ. Geol.* **1991**, *86*, 667.
[24] Y. X. Chen, X. He, X. J. Zhao, M. X. Song, X. Y. Gu, *Mater. Sci. Eng. B Solid State Mater. Adv. Technol.* **2007**, *139*, 88.
[25] P. Guha, D. Das, A. B. Maity, D. Ganguli, S. Chaudhuri, *Solar Ener. Mater. Solar Cells* **2003**, *80*, 115.
[26] U. Schwarz-Schampera, P. M. Herzig, 'Indium: Geology, Mineralogy, and Economics', Heidelberg, Springer, **2002**.
[27] T. Miyauchi, N. Yamamoto, H. Higuchi, *Jap. J. Appl. Phys. 2 Lett.* **1988**, *27*, L1178.
[28] S. Gorai, S. Bhattacharya, E. Liarokapis, D. Lampakis, S. Chaudhuri, *Mater. Lett.* **2005**, *59*, 3535.
[29] T. Nyari, P. Barvinschi, R. Baies, P. Vlazan, F. Barvinschi, I. Dekany, *J. Crys. Growth* **2005**, *275*, e2383.
[30] X. H. Hou, K. L. Choy, *Thin Solid Films* **2005**, *480*, 13.
[31] H. M. Pathan, C. D. Lokhande, *Appl. Surf. Sci.* **2004**, *239*, 11.
[32] I. Oja, M. Nanu, A. Katerski, M. Krunks, A. Mere, J. Raudoja, A. Goossens, *Thin Solid Films* **2005**, *480*, 82.
[33] B. A. Grguric, 'Polymorphism and exsolution in the bornite-digenite solid solution series', Churchill College, University of Cambridge, Cambridge, **1998**.
[34] L. Reijnen, B. Meester, A. Goossens, J. Schoonman, *Chem. Vapor Deposition* **2003**, *9*, 15.
[35] Y. B. Lou, A. C. S. Samia, J. Cowen, K. Banger, X. B. Chen, H. Lee, C. Burda, *Phys. Chem. Chem. Phys.* **2003**, *5*, 1091.
[36] M. Fadden.??? **2008**.
[37] J. P. Vaughan, A. Kyin, *Miner. Mag.* **2004**, *68*, 255.
[38] J. Zhao, J. Brugger, P. V. Grundler, F. Xia, G. R. Chen, A. Pring, *Amer. Miner.* **2009**, *94*, 1541.
[39] J. Zhao, F. Xia, A. Pring, J. Brugger, P. Grundler, G. Chen, *Miner. Eng*. **2010**, online 23 December 2009.
[40] J. M. Thomas, W. J. Thomas, 'Principles and practice of heterogeneous catalysis', 1997, New York, Wiley-VCH, **1997**.
[41] C. S. Cundy, P. A. Cox, *Chem. Rev*. **2003**, *103*, 663.
[42] L. Tosheva, V. P. Valtchev, *Chem. Mater*. **2005**, *17*, 2494.
[43] M. A. Snyder, M. Tsapatsis, *Angew. Chem. Int. Ed.* **2007**, *46*, 7560.
[44] M. E. Davis, *Nature* **2002**, *417*, 813.
[45] R. Srivastava, M. Choi, R. Ryoo, *Chem. Commun.* **2006**, *43*, 4489.
[46] K. H. Rhodes, S. A. Davis, F. Caruso, B. J. Zhang, S. Mann, *Chem. Mater.* **2000**, *12*, 2832.
[47] M. W. Anderson, S. M. Holmes, N. Hanif, C. S. Cundy, *Angew. Chem. Int. Ed.* **2000**, *39*, 2707.
[48] G. Calzaferri, K. Lutkouskaya, *Photochem. Photobiol. Sci*. **2008**, *7*, 879.
[49] F. Xia, J. Brugger, Y. Ngothai, B. O'Neill, G. R. Chen, A. Pring, *Crys. Growth Design* **2009**, *9*, 4902.
[50] C. V. Putnis, T. Geisler, P. Schmid-Beurmann, T. Stephan, C. Giampaolo, *Amer. Miner.* **2007**, *92*, 19.
[51] F. Xia, B. O'Neill, Y. Ngothai, J. Peak, C. Tenailleau, B. Etschmann, G. Qian, J. Brugger, A. Studer, S. Olsen, A. Pring, *J. Appl. Crys*. **2010**, 43.
[52] A. Putnis, 'Introduction to mineral sciences', Cambridge University Press, **1992**.
[53] W. A. Deer, R. A. Howie, J. Zussman, 'An introduction to the rock-forming minerals', 2nd ed. Essex, Longman, **1996**.
[54] Y. Zhang, J. Wu, P. Rao, M. Lv, *Mater. Lett.* **2006**, *60*, 2819.
[55] D. C. Palmer, A. Putnis, E. K. H. Salje, *Phys. Chem. Miner.* **1988**, *16*, 298.

APPENDIX F

Statement of Authorship

Title of Paper	**Hydrothermal mineral replacement reactions and their applications in mining and processing.**
Publication Status	◉ Published, ○ Accepted for Publication, ○ Submitted for Publication, ○ Publication style
Publication Details	**Zhao, J., Pring, A., Brugger, J., Xia, F., Li, K., and Ngothai, Y. Hydrothermal mineral replacement reactions and their applications in mining and processing. 5th International Seminar on Process Hydrometallurgy, Santiago, 10-12 July, 2013.**

Author Contributions

By signing the Statement of Authorship, each author certifies that their stated contribution to the publication is accurate and that permission is granted for the publication to be included in the candidate's thesis.

Name of Principal Author (Candidate)	**Jing Zhao**		
Contribution to the Paper	**Designed and performed experiments, interpreted and processed data, wrote manuscript.**		
Signature		Date	**6 August 2013**

Name of Co-Author	**Allan Pring**		
Contribution to the Paper	**Supervised development of work and helped in manuscript evaluation.**		
Signature		Date	**8 August 2013**

Name of Co-Author	**Joël Brugger**		
Contribution to the Paper	**Supervised development of work, helped in data interpretation and manuscript evaluation.**		
Signature		Date	**5 July 2013**

Name of Co-Author	**Fang Xia**		
Contribution to the Paper	**Helped to evaluate and edit the manuscript.**		
Signature		Date	**6 August 2013**

Name of Co-Author	**Kan Li**		
Contribution to the Paper	**Helped to evaluate and edit the manuscript.**		
Signature		Date	**15 August 2013**

Name of Co-Author	**Yung Ngothai**		
Contribution to the Paper	**Supervised development of work and helped in manuscript evaluation.**		
Signature		Date	**6 August 2013**

Zhao, J., Pring, A., Brugger, J., Xia, F., Li, K. & Ngothai, Y. (2013) Hydrothermal mineral replacement reactions and their applications in mining and processing.
5th International Seminar on Process Hydrometallurgy, Santiago, Chile, 10-12 July